HIGHLIGHTS

Small et al*., *Antarctic ice sheet palaeo-thinning rates from vertical transects of cosmogenic exposure ages.

- Exposure ages that constrain ice sheet thickness collated from an online database.
- Thinning rates are reconstructed from 23 sites across Antarctica.
- Palaeo-thinning rates are comparable to modern observations.
- Wide-spread thinning during the Holocene, but after Meltwater Pulse 1A.

Antarctic ice sheet palaeo-thinning rates from vertical transects of cosmogenic exposure ages.

David Small[1*], Michael J. Bentley[1], R. Selwyn Jones[1], Mark L. Pittard[1], Pippa L. Whitehouse[1]

[1] Department of Geography, Durham University, Durham, UK, DH1 3LE

* Corresponding author: david.p.small@durham.ac.uk

Abstract

Constraining Antarctic ice sheet evolution provides a way to validate numerical ice sheet models that aid predictions of sea-level rise. In this paper we collate cosmogenic exposure ages from exposed nunataks in Antarctica that have been used, or have the potential to be used, to constrain rates of thinning of the Antarctic Ice Sheets since the Last Glacial Maximum. We undertake quality control of the data and adopt a Bayesian approach to outlier detection. Past thinning rates are modelled by Monte Carlo linear regression analysis. We present thinning rates from 23 sites across Antarctica. The resulting data set is the first Antarctic-wide collation of past ice sheet thinning rates and provides an empirical starting point for future model-data comparisons. Palaeo-thinning rates are spatially variable with high rates appearing to correlate to areas of contemporary rapid changes. On centennial timescales past thinning rates are comparable to modern day observations implying that modern day thinning has the potential to persist for centuries in numerous parts of Antarctica. The onset of abrupt thinning from all sites post-dates Meltwater Pulse 1A suggesting that its source region(s) are distal to areas where exposure age constraints on ice surface geometry exist.

Keywords: Holocene; Glaciology; Antarctica; Cosmogenic isotopes; Ice sheet thinning; Model-data comparison.

1. Introduction

Anthropogenic climate change is driving changes in the Antarctic Ice Sheets (AISs) which will be the largest contributors to future sea-level rise (IPCC, 2013). Present day measurements indicate that Antarctica is losing mass (Shepherd et al., 2012) and the rate of mass loss is increasing (Rignot et al., 2011; Velicogna et al., 2014; Harig and Simons, 2015; Shepherd et al., 2018). Most observed mass loss occurs as rapid changes to the major ice streams that drain the AISs (Shepherd et al., 2001; Pritchard et al., 2009; Flament et al., 2012; Joughin et al., 2014; Rignot et al., 2014; Scheuchl et al., 2016; Konrad et al., 2018). Modern observations can directly constrain the timing and rates of ice mass changes in Antarctica (Miles et al., 2013; Rignot et al., 2014; Konrad et al., 2018) and help identify the mechanisms that drive mass loss (De Angelis and Skvarca, 2003; Pritchard et al., 2012). However, they are limited to the last ~60 years for which satellite and direct observations exist, preventing modern rates being placed in a longer-term context. Palaeo-data can contextualise modern-day observations and provide a longer temporal record of the behaviour of the AISs (e.g. Bentley, 2010; Balco, 2011; Stokes et al., 2015).

In recent years surface exposure dating (SED) using *in situ* terrestrial cosmogenic nuclides has contributed greatly to an improved understanding of the evolution of the AISs since the Last Glacial Maximum (LGM) (e.g. Ackert et al., 1999; Stone et al., 2003; Bentley et al., 2006; Mackintosh et al., 2007; Johnson et al., 2014; Balco et al., 2016). Given the general scarcity of ice-free areas and the fact that much of the ice sheet margin is marine based, studies that use SED to constrain the former lateral extent of ice are rare (cf. Joy et al., 2017). A more common approach involves dating erratic cobbles – glacially-transported rocks that have been deposited on nunataks as the ice sheet thinned – to constrain vertical changes in the AISs from the LGM to the present day: the so-called 'dipstick approach' (e.g. Ackert et al., 1999; Stone et al., 2003).

As an ice sheet thins, and assuming no prior exposure, cosmogenic exposure ages of erratic cobbles deposited on nunataks will get progressively younger as elevation decreases. This principle allows the past surface geometry of the ice sheet to be constrained by: 1) providing minimum constraints on the extent and timing of the maximum ice sheet surface elevation where a sample is from below said maximum, and 2) directly constraining past ice surface elevation (and timing) where the sample is from a setting that delimits the former ice sheet surface. Similarly, where samples are from progressively lower altitudes they provide an opportunity to constrain surface elevation change through time (Figure 1). Over relatively short time-scales (e.g. ~10^2 – 10^5 years) this ice surface elevation broadly defines ice thickness, given knowledge of bed elevation. An increasing number of studies have presented SED ages from vertical transects and some have used these data to reconstruct past rates of thinning. Thinning histories have been linearly extrapolated from cosmogenic exposure ages (e.g. Johnson et al., 2008; Bentley et al., 2010) and modelled using Monte Carlo (MC) linear regression analysis (e.g. Johnson et al., 2014; Jones et al., 2015; Hein et al., 2016).

Reconstructed thinning rates are important because they: 1) offer a dataset that can be used to assess the output of numerical ice sheet models, and 2) inform on processes that influence deglacial behaviour but are not currently operating or operate on timescales beyond the observational record. In this paper we present a dataset of reconstructed thinning rates, calculated from a collation of cosmogenic exposure ages from Antarctica that will be used in a future model-data comparison exercise. We use a consistent approach to quality control and calculation of thinning rates to allow direct comparison between the reconstructed rates. Our compilation of palaeo-thinning rates is compared to contemporary changes in the ice sheet to inform on potential drivers of past thinning. Finally, our approach allows us to place temporal constraints on thinning and we compare these to global sea-level change since the LGM.

2. The utility of thinning rates for model-data comparison

Geological observations can be used to test the hindcasting abilities of numerical ice sheet models and improve future estimates of sea-level rise (Tarasov et al., 2012; Whitehouse et al., 2012; Briggs and Tarasov, 2013; Lecavalier et al., 2014; Stokes et al., 2015). Traditionally, workers have compared ice sheet model outputs to point measurements that constrain ice sheet configuration at some time in the past (e.g. Briggs et al. 2014; Ely et al., *in review*). Undertaking such model-data comparisons requires a quantification of uncertainties associated with both ice sheet models and geological data (cf. Briggs and Tarasov, 2013). Models use simplifications of real-world physical processes to reconstruct ice sheet configuration and evolution in time. A modelled deglaciation chronology is the product of boundary conditions (e.g. basal sliding, bed topography, climate-ocean forcing, grid-resolution) imposed on that particular experiment; by adjusting parameters, model ensembles can explore the parameter space and quantify (to some degree) uncertainties on modelled deglaciation chronologies (Tarasov and Peltier, 2004; Briggs et al., 2014). Similarly geological data have uncertainties in both measurement and interpretation. These can be quantified through appropriate data reduction and laboratory procedures (e.g. Rood et al., 2013; Corbett et al., 2016) or through expert judgement (e.g. Hughes et al., 2016). However, geological processes introduce an implicit and often unquantifiable level of uncertainty. This can stem from i) factors that could affect the measured property prior to sampling, which workers have little control over, and ii) the strength of the geological association between the material that is being dated and the event of interest. This 'geological uncertainty' (cf. Small et al., 2017) requires that geochronological data undergo some form of quality control before further use (Blockley et al., 2008; Graf, 2009; Small et al., 2017).

In continental-scale model-data comparisons the spatial distribution and contiguity of geological data is fundamentally different to ice sheet model output (Ely et al., *in review*). Ice sheet models produce spatially and temporally continuous outputs for the model domain, albeit at a defined spatial (grid cell) and temporal (time-step) resolution. Conversely geological data usually represent point measurements in space and time that, providing the data point is accurate, constrain ice sheet configuration (e.g. ice free vs. ice covered). The disparity in scale requires point data constraints be assumed to represent the configuration of the ice sheet for the entirety of the grid cell to which the data have been assigned. This may be unrealistic when many 'dipstick' measurements occur in regions of complex topography, rather than a smooth ice sheet surface. One approach to bridge this gap is to spatio-temporally interpolate geological data. For lateral ice sheet margins this can be done by creating isochrones of ice margin positions (Clark et al., 2012; Bentley et al., 2014; Hughes et al., 2016) or through a Bayesian approach to modelling geochronological data that produces deglacial ages and age uncertainties along a reconstructed flowline (Chiverrell et al., 2013; Small et al., 2018). For changes in ice sheet surface elevation, vertical transects of geochronological data provide constraints on timing and rates of ice sheet thinning.

The potential to compare ice sheet model output to *rates* of change, specifically thinning rates in this case, has advantages over individual measurements. Firstly, where a rate is reconstructed using single nuclide SED, the derived rate will be broadly insensitive to systematic uncertainties which should affect all samples within a transect proportionally. Additionally, in Antarctica scaling uncertainties relating to solar modulation are minimal, however, care should be taken when comparing rates that are integrated over different timescales (e.g. mid-Holocene vs. post-LGM period) as these may be biased by temporal averaging of the datasets that underlie the scaling model. That said, (dis)agreement between a reconstructed rate and modelled rates (n.b. *not* the precise *timing* of thinning) remains a robust comparison even in the event of future refinements in the dating technique. This is important where models simulate retreat at different times to geological data, sometimes due to uncertainties in forcing data such as climate input. In the case of point measurements, if the age changes by a given amount the data-model agreement/misfit will also change by a correlated amount. Specifically, this may change the absolute agreement such that model output(s) that were previously conformable with observations are now incompatible. Another advantage is that a thinning rate can be reasoned on glaciological grounds to be representative of ice sheet change on scales similar to, and greater than, the grid resolution commonly used in modelling experiments of ice sheet evolution since the LGM (Mackintosh et al., 2011; Golledge et al., 2012; DeConto and Pollard, 2016).For example, longitudinal stress-coupling allows perturbations that increase mass flux through the grounding line, such as thinning and/or disintegration of buttressing ice shelves, to result in rapid propagation of dynamic thinning inland at distances of >100 km (Pritchard et al., 2009; Wingham et al., 2009; Reese et al., 2018). Despite these advantages the use of thinning rates for model-data comparison requires that the derived rate be a robust approximation of the past rate of change. This requires 1) Identification and removal of data points whose apparent exposure age does not accurately reflect the true age of deglaciation at a given altitude, and 2) A means of calculating a thinning rate that accounts for reported uncertainties in the remaining data set.

3. Methods

We surveyed the online ICE-D Antarctica database (http://antarctica.ice-d.org/: census date: November 2017) and extracted previously published data (^{10}Be and ^{26}Al) from sites where exposure ages are < 25 ka and span a suitable altitudinal extent (>50 m) or were inferred by the original authors to constrain thinning (Figure 2; supplemental Table S1). We consider this appropriate as the AISs are likely to have been at, or very near to, their maximum extent at 25 ka (Clark et al., 2009; Bentley et al., 2014). The input file(s) for all sites are included in the Supplemental Data Table S2. We re-calculated the ages using the input data contained within ICE-D using v3 of the CRONUS-Earth online calculators (https://hess.ess.washington.edu/). All ages were calculated assuming zero erosion. Densities (2.20 - 2.94 g cm^{-3}) are taken from the original publications as per the ICE-D database. We present ages calculated using the Lal-Sato-Dunai nuclide-specific (LSD_n) scaling scheme (Lifton et al., 2014). Given that subsequent analyses utilise the external uncertainties and 2σ internal uncertainties our results are insensitive to choice of scaling scheme or density value.

As a first-order quality control criterion we excluded ages with discordant (i.e. the apparent exposure ages do not overlap within their respective uncertainties) $^{26}Al/^{10}Be$ ages as this suggests a complex exposure history. Ages from samples currently emerging from ice or located on present day blue ice moraines were not used to reconstruct thinning rates as the relationship between these exposure ages and the thinning represented by ages from clasts deposited on the flanks of nunataks is not clear (cf. Hein et al., 2016). These ages were however used to constrain the minimum age of cessation of thinning where possible (i.e. Marble Hills and Patriot Hills). We acknowledge that this approach may lead to exclusion of a small amount of potentially useful data but consider it appropriate given the broad scale of our study and the future implementation of the derived dataset.

We did not attempt to reconstruct thinning rates from sites with fewer than four exposure ages as a low number of samples reduces confidence in the subsequent identification of outliers. To maximise the data available we combined data-sets where exposure ages were inferred to constrain thinning but quantified rates had not previously been reported. One issue that arises from combining sites that extend for several km in an along-flow direction is that distal samples that were exposed simultaneously can occur at different altitudes (Spector et al., 2017). Three of our combined sites (Figure 2, Table 1; Sites 11 - 13) had elevations normalised with respect to the modern ice surface, and an elevation projection (cf. Spector et al., 2017) was not required. The other combined site (Figure 2, Table 1; Site 22) has no current glacier from which to extract a gradient, hence we assumed a low gradient of 0.01 for the elevation projection. Projection introduces a degree of altitudinal uncertainty, however, given the limited amount of data to which this approach was applied, and the fact that the results are to be used as a first order comparison to model output, we consider this acceptable. In one case (Mackintosh et al., 2007) the relatively large distances between individual sites (>10 km) meant we could not confidently project altitudes and thus did not include these data in further analyses. To calculate thinning rates for all other sites we used normalised elevations where these were reported and raw elevations above sea level where they were unreported. In total we present 25 thinning rates from 23 sites (Figure 2, Tables 1 and 3). The regressed exposure ages and elevations are included in supplemental Table S3.

3.1 Bayesian Outlier detection

Older and higher samples should be exposed by ice surface lowering before the lower samples. This age-elevation relationship can be used to reduce the uncertainties of exposure ages (Jones et al., 2015) but such an approach also allows outliers to be identified using *OxCal* v4.3 (Bronk Ramsey, 2017; https://c14.arch.ox.ac.uk/oxcal/OxCal.html). The independent age measurements were arranged into a relative order of exposure; the *prior model* (Buck et al., 1996; Bronk Ramsey, 2008, 2009a), and assigned an initial probability (*prior probability*) of being an outlier in time (*t-type* outlier cf. Bronk Ramsey, 2009b). The outlier model calculates a subsequent probability (*posterior probability*) for a given measurement being an outlier. In practice the *prior model* contains a series of independent age probability distributions (SED ages) that are often overlapping. Bayesian age modelling in *OxCal* v4.3 uses Markov Chain Monte Carlo sampling to assess the conformability of the age measurements and produce a model output of refined age distributions. Where the refined age distribution of a given sample does not overlap with its un-modelled initial age distribution the *posterior probability* of the sample being an outlier will increase (Figure 3). We assigned each age measurement a low *prior probability* of being an outlier of 0.05 (i.e. 1 in 20). *OxCal* produces a model agreement index (A) with 60 being the commonly-adopted threshold value (Bronk Ramsey, 2008). If $A > 60$ then samples with an outlier *posterior probability* >0.5 (i.e. more likely to be an outlier than not (Bronk Ramsey, 2009b)) were excluded from further analysis. If $A < 60$ then the model was re-run iteratively, increasing the *prior probabilities* (i.e. down-weighting) of samples whose *posterior* > *prior*, until an acceptable A index value was obtained (Figure 4).

We used the "general" outlier definition within the *Sequence* model of *OxCal* (Bronk Ramsey, 2009a), which uses a student's t-distribution to define how outliers are distributed, and a timescale of 10^0-10^4 years (i.e. a sample may be an outlier by a few years or by many thousands of years). The *Sequence* model only requires samples to be in a stratigraphic order and it uses a uniform prior (Bronk Ramsey, 2009a). This essentially assumes a linear interpolation between dates akin to a linear sedimentation rate within a sedimentary sequence. The relatively large uncertainties associated with exposure ages preclude identification of variable thinning rates between individual samples. Where there is some constraint on the timing of maximum ice surface elevation, such as samples from a high lateral moraine or above a weathering limit, we imposed a *Boundary* between those samples and the samples that are inferred to constrain thinning to account for any potential abrupt shift in the rate of change. In some cases, where there was a significant temporal gap between vertically adjacent samples, a *Boundary* was required to obtain a conformable model. Bayesian outlier detection was undertaken on ^{10}Be ages only. Given that the 26Al/10Be nuclide pair cannot discriminate short (i.e. 10^3 – 10^4 years) periods of complex exposure on the timescales we are interested in we do not think it is appropriate to weight our Bayesian outlier detection to the limited number of samples where paired $^{26}Al/^{10}Be$ analyses are available. In total only 43 ^{26}Al analyses pass our age screening criteria thus we do not consider that our results would be sensitive to their inclusion. All model outputs are included in supplemental data.

3.2 Monte Carlo Linear Regression

MC linear regression analysis was undertaken using a MATLAB® model (Jones et al., 2015; Jones et al., *in review*) that is based on the general approach of Johnson et al. (2014). Thinning rates are generated from 5000 iterations through randomly sampled points using 2σ internal uncertainties. Regressions that produce a reverse slope are excluded as implausible. The model outputs the 68% and 95% ranges of thinning rates, the 'best-fit' thinning rate, the median thinning rate, and a histogram of modelled rates. Thinning rates were calculated using ^{10}Be exposure ages that produced a conformable Bayesian sequence and were not flagged as outliers (see Section 3.1). Where vertical transects were punctuated by *boundaries* we estimated thinning rates based on the longest continuous sequence of exposure ages between individual boundaries. For consistency we calculated thinning rates from ^{10}Be exposure ages only. Examples of the model output are shown in Figure 5 and all model outputs are included in supplemental data.

4. <u>Results</u>

All transects yielded Bayesian sequences with acceptable A indices after exclusion (or suitable down-weighting) of samples flagged as being potential outliers (Table 2). In general the number of samples excluded represents a small proportion of the total compilation and in all but one case (Thomas Hills) the number of excluded samples is <50%. Bayesian outlier analysis identifies outliers on the basis that their *posterior* age probabilities are not conformable within a continuous sequence representing progressive thinning. It does not differentiate between samples that are "too old" and samples that are "too young"., Assessing the relative likelihood of processes that act to make an age "too young" or "too old" is best carried out by the field workers. As we compiled previously published datasets we cannot make that appraisal. Considering this fact, and to retain objectiveness and reproducibility, we did not manually re-introduce 'young' erratics flagged as outliers into the MC analysis that produced the thinning rates presented in Table 3. In total 6 samples from 5 transects were excluded as being 'too young' (Table 6).

The modelled thinning rates obtained by the MC approach outlined here are summarised in Figure 6 and Table 3. Thinning rates range from 0.01 – 6.41 m yr^{-1} (1σ; 68%) and 0.02 – 37.72 m yr^{-1} (2σ; 95%) with best fit thinning rates ranging from 0.02 – 1.67 m yr^{-1} and median rates ranging from 0.02 – 1.57 m yr^{-1}. For ease of discussion we quote the 'best-fit' rate when outlining rates from individual sites as this metric best illustrates contrasts in rate. At two sites, Pourquoi-Pas Island and Thomas Hills, the 'best-fit' regression produced a negative slope and is not reported. For these sites we instead use the median rate while acknowledging that the exposure age data implies a potentially much higher rate of thinning.

The results from transects that have previously been used by other authors to calculate thinning rates are somewhat comparable to these previously published rates (Table 4) with notable exceptions of Mount Moses (Figure 2, Site 10; Johnson et al., 2014), Low Ridge (Site 5; Jones et al., 2015), and the Marble Hills (Site 14; Hein et al., 2016). For Mount Moses and Low Ridge this is because the samples are in age stratigraphic order and, as per our protocol, thinning rates were calculated from all samples. The original studies identified a change in thinning rate, and calculated their rate from the uppermost samples that defined the period of more rapid thinning. For comparison we also calculated thinning based on these upper samples and obtained a similar rate (Table 4). These values are included in Table 3 as alternative thinning rates from Mount Moses and Low Ridge. Given the close agreement between the higher rates and those from neighbouring sites - Maish Nunatak (Figure 2, Site 9), and Mount Suess/Gondola Ridge (Site 3) - we use the rapid thinning rates in further discussions. For the Marble Hills (Site 14) our best-fit rate is somewhat lower (0.08 m yr^{-1}) than the rate quoted by Hein et al. (2016) (0.21 m yr^{-1}). This is because we combined all samples from the Marble Hills (Bentley et al., 2010; Hein et al., 2016) and, on the basis of our approach to outlier detection and removal, our rate is calculated from a different sub-set of these samples compared with the rate of Hein et al. (2016). When we used only the same samples we obtained a similar rate of 0.28 m yr^{-1}.

Both Bayesian and MC analyses provide estimates of the timing of thinning onset and cessation (Table 5). As the thinning rates discussed in this paper are derived from the MC analysis the discussion regarding timings of thinning focuses on the MC derived estimates. It is important to note that the estimates of thinning onset/cessation are maximum and minimum constraints respectively. As identified by previous studies (e.g. Bentley et al., 2017; Johnson et al., 2014; Jones et al., 2015; Hein et al., 2016) widespread thinning occurs during the Holocene at numerous locations throughout East and West Antarctica. The earliest onset of thinning at c. 12 ka occurs in the Ross Sea region of the Transantarctic Mountains (Mount Hope (Figure 2, Site 1) and Mount Rigby/Karo (Site 2); Spector et al., 2017). At the other sites thinning onset is focussed in the early to mid-Holocene. The latest inferred onset of thinning occurs at c. 3 ka at Mount Rea (Figure 2, Site 16); Stone et al., 2003), although early Holocene thinning onset is also recorded at nearby sites; Mount Darling (Site 17) and Mount Valkenburg (Site 18; Stone et al., 2003). The transect locations, reconstructed rates and modelled onset/cessations are combined and included as supplementary Table S4.

5. <u>Discussion</u>

5.1 Considerations when using MC analysis to model thinning rates

Bayesian outlier analysis identifies outliers on the basis that their *posterior* age probabilities are not conformable within a continuous sequence representing progressive thinning. It does not differentiate between samples that are "too old" and samples that are "too young". In total 6 samples from 5 transects were excluded as being 'too young'. (Table 6). The specific effect of manually inserting these 'outliers' depends on their location within the vertical transect and the number of other samples considered in the regression analysis. A linear regression line intersects with the mean of the predictor and response variables. Consequently, if a predictor value (i.e. elevation) is far from the mean then an extreme response value (i.e. young age due to transient shielding) will lead to a larger change in the regression slope (Figure 7; cf. Altman and Kryzywinski, 2016). The best fit thinning rate, defined by the regression slope, is thus most sensitive to extreme ages at the top and bottom of the vertical transect. In contrast, samples with extreme ages located near the mean of the elevation distribution have lower influence on the regression slope.

This sensitivity to a sample's elevation has some important implications. If a sample is conformable but is not an accurate exposure age due to undetected geological uncertainty it will influence the estimated thinning rates. For example, a small amount of inheritance within samples at the upper and lower limits of an elevation transect can act to reduce and increase the best-fit thinning rates respectively. In general transects with smaller numbers of samples, particularly where these are unevenly distributed in space and/or define monotonic thinning, are likely to be most sensitive to the effects of undetected geological uncertainty. This is well illustrated at Thomas Hills (Figure 2, Site 12) where the samples are clustered towards the upper and lower ends of the transect and the modelled thinning rates – 1.57 m yr^{-1} (median); 0.36–37.72 m yr^{-1} (95% range) – are the highest and most widely distributed in our compilation. It is notable that these rates are significantly higher than those from nearby sites (Williams Hills (Figure2, Site 11), Mount Harper/Bragg (Site 13)). This may reflect site specific conditions, such as a particularly extreme windscoop or local flow re-organisation, or alternatively the Thomas Hills data set may be influenced by geological uncertainty. Specifically, if inheritance was prevalent in the lower-most samples, but to an extent that did not make samples unconformable, then this geological uncertainty would be undetected by our analysis. Ideally, multiple samples from similar elevations would allow outliers to be identified using statistical approaches (e.g. Balco, 2011; Jones et al., *in review*; Rinterknecht et al., 2006). However, there are numerous reasons why this may not be possible including adequate resources, lithology, sample availability, and restricted time on the ground.

Linear regression implicitly averages the rate of change over the period of observation and as such precludes identification of variations in the rate of thinning. For many sequences the scatter of exposure ages and their inherent uncertainties (even after identification and removal of outliers) may make identification of such variations in thinning rate exceedingly difficult. However for more coherent sequences of exposure ages, particularly those that span longer timeframes (e.g. Spector et al., 2017), there may be useful information regarding the timing of changes in thinning rate if they can be identified. Johnson et al. (2014) used a two-segment, piecewise regression for the Mount Moses data-set to define a change in the thinning rate implied by a distinct break in slope in a simple linear interpolation between the exposure ages. This approach relies on such a break of slope being identifiable, which may not always be the case. A potential alternative approach to account for temporal changes in thinning rate is to use a time-dependent statistical model in a similar way to approaches employed in reconstructing rates of sea-level change (e.g. Cahill et al., 2015; Kemp et al., 2017; Khan et al., 2015). Examining residual plots from a simple linear regression is one potential means to identify transects where time variable rates may be appropriate. Subsequently, a spline-based model could allow continuous and dynamic evolution of thinning rate changes to be estimated (Jones et al., *in review*).

5.2 Discussion of reconstructed palaeo-thinning rates

5.2.1 Comparison to modern thinning rates

Modern rates of ice surface changes in Antarctica are primarily quantified through satellite observations, specifically satellite altimetry (c.f. Shepherd et al., 2018) and whilst some areas are thinning, the rates are highly variable, with some parts of Antarctica showing little change or even thickening (Pritchard et al., 2009; McMillan et al., 2014). Additionally, the spatial scale over which rates are quantified is also variable with some rates being presented as basin averages while others are more limited in space (e.g. thinning rates close to a grounding line). We compiled a number of published thinning rates for comparison to the reconstructed palaeo-rates. This is not an exhaustive compilation of modern rates but is intended to show the range of reported rates from satellite observations.

Overall, the modelled palaeo-thinning rates are generally lower than modern thinning rates measured by satellite altimetry although notably there is some overlap in the ranges (Figure 8 and Table S1). Specifically, the overlap occurs in those palaeo-observations that correspond to centennial observation intervals which have a similar range to modern (annual to decadal) rates.

Palaeo-rates that are derived from exposure ages that span longer (>10^3 years) observation intervals are lower. There are a couple of potential explanations for this pattern. Modern observations demonstrate that thinning is focused in the central portions of ice streams (e.g. Shepherd et al., 2001; Wingham et al., 2009). In the case of Pine Island Glacier, the rates of thinning within the main trunk of the ice stream and the average for the entire drainage basin differ by an order of magnitude (>2m yr^{-1} *vs* 0.11 m yr^{-1}; Wingham et al., 2009). This difference is driven by lower rates of thinning in areas of slow flow (Wingham et al., 2009). These areas correspond to areas of ice overlying topographic/bedrock highs between faster flowing ice corridors. The fast flowing areas generally correspond to deeper subglacial troughs where ice flow is accelerated by basal sliding and lateral drag is minimal (Stenoien and Bentley, 2000; Shepherd et al., 2001). The SED data used to reconstruct palaeo-thinning rates are, by necessity, collected from topographic bedrock highs as these form the exposed rock areas required for applying the technique, potentially explaining the general lower thinning rates reconstructed in the past.

Another potential explanation relates to the disparity in temporal sampling resolution between modern observations and palaeo-data. Modern observations span the last couple of decades with thinning rates often calculated from a few years of data so, on geological timescales, these represent point measurements. Conversely, palaeo-rates are reconstructed from data that span 100’s to 1000’s of years and these rates represent a time-averaging of thinning rates that likely varied to be both faster and slower than the long-term average. It is implicit that high rates of dynamic thinning cannot be maintained at any location over long (10^3) timescales and are relatively short-lived events, an inference reflected by the fact that the highest paleo-rates correspond to sites where the data span a relatively shorter period of time (Figure 8). As dynamic thinning progresses the spatial pattern changes (cf. Shepherd et al., 2001; Wingham et al., 2009). A given location will experience different flow regimes as the drainage basin evolves through time due to retreat/stabilisation of the grounding line, ice divide migration etc. This may be a potential explanation for any sites where variable rates of thinning can potentially be identified and quantified. A thinning rate reconstructed from a given location not only represents an average through time but also a quasi-spatial average. That is, over long timescales a thinning rate will be more reflective of the basin average than of the higher measurements of thinning within the main glacier trunk. The lower rates reconstructed in the past may therefore, at least partially, reflect an averaging effect.

The overlap of modern and palaeo-rates suggests that modern rates of thinning may be consistent with those that occurred during the Holocene in various parts of Antarctica. Importantly, the overlap at centennial timescales implies that dynamic thinning, once initiated, can be sustained for hundreds of years. This implication was previously highlighted by Johnson *et al.*, (2014) for the Pine Island Glacier catchment (Figure 2, Sites 9 and 10) but it may be speculated that the potential for centennial scale thinning and associated grounding line retreat may be pervasive across Antarctica.

5.2.2 Spatial and temporal patterns of thinning rates and potential implications

Sites with the highest inferred palaeo-thinning rates are located in the Amundsen Sea sector of West Antarctica (Maish Nunatak and Mount Moses) and the Antarctic Peninsula (Pourquoi-Pas Island; Figure 9). These are both locations where modern observations record rapid changes in ice surface geometries. In the Amundsen Sea sector satellite observations record contemporary thinning rates of 1 - >4 m yr^{-1} within the trunk of Pine Island Glacier (e.g. Wingham et al., 2009; Park et al., 2013) with comparable rates from nearby Thwaites Glacier (Shepherd et al., 2002; Pritchard et al., 2009). In the Antarctic Peninsula thinning of outlet glaciers has been observed in connection with the thinning and breakup of buttressing ice shelves with rates ranging from c.1.5 - 3 m yr^{-1} (Wouters et al., 2015; Friedl et al., 2018) to >10 m yr^{-1} (Rignot et al., 2004; Scambos et al., 2004).

In the Amundsen Sea the primary driver of ice shelf thinning is inferred to be oceanic with increased influx of warm Circumpolar Deep Water (CDW) at depths exceeding 300 m driving increased melting in the sub-ice shelf cavity (Rignot and Jacobs, 2002; Jenkins et al., 2010; Jacobs et al., 2011). This process has been cited as the driver of contemporary thinning across a wide swathe of the West Antarctic margin (Pritchard et al., 2012). In the Antarctic Peninsula rising air temperatures have been correlated with the breakup of fringing ice shelves (Vaughan and Doake, 1996) but other studies have invoked oceanic forcing as the primary driver of melting (e.g. Wouters et al., 2015). Although a contribution from atmospheric forcing is likely, the widespread extent of contemporary thinning, even in areas where atmospheric forcing is insignificant, points to the ocean as a primary driver of the observed changes. Under this assumption the correlation in the locations of the high modelled palaeo-thinning rates and the highest observed modern rates is notable and suggests that a common oceanic forcing could have been prevalent during deglaciation (cf. Smith et al., 2007; Hillenbrand et al., 2017) although the influence of trough geometry is also likely to play a key role in determining the absolute magnitude of thinning (Jamieson et al., 2014; Jones et al., 2015). That said, for rapid thinning to occur requires an initial driver before the positive feedback influences of reverse bed slopes and/or deep troughs are fully engaged. Notably, Pourquoi-Pas Island (Figure 2, Site 11), where thinning may have been rapid – as implied by the negative slope of the best-fit regression – is located on the western margin of the Antarctic Peninsula which is thought to be particularly sensitive to changes in the Antarctic Circumpolar Current and associated influxes of CDW (Bentley et al., 2009). Additionally, there is evidence of southward penetration of warm CDW waters during the early-mid Holocene from sediment cores in Palmer Deep (Leventer et al., 2002) and Pine Island Bay (Hillenbrand et al., 2017). This presence of warm water coincides broadly with the modelled timing of thinning around Pine Island Glacier at 8.5–7.5 ka (cf. Johnson et al., 2014). Given the indications that CDW was present in the Amundsen and Bellingshausen Seas during the earliest Holocene (Hillenbrand et al., 2017; Peck et al., 2015) it can be speculated that the rapid thinning at Pourquoi-Pas Island was potentially related to grounding line retreat and/or a decrease in buttressing from fringing ice shelves at c.11.6 ka. This timing is broadly co-incident with marine foraminiferal records and radiocarbon ages that constrain initial outer shelf deglaciation of the Marguerite Bay Ice Stream at c.13 ka, with retreat of grounded ice from the inner portion of Marguerite Bay more proximal to Pourquoi-Pas Island by c.9.5 ka (Heroy and Anderson, 2007; Kilfeather et al., 2011).

The two sites on the eastern Antarctic Peninsula have lower modelled thinning rates than PQP on the western Antarctic Peninsula. While we cannot completely exclude the possibility that these differences reflect effects of sampling resolution the sites span a comparable altitudinal range and do not exhibit any evidence for a significant step change in thinning rate. Consequently, while acknowledging that the data points are limited, we suggest that the difference in modelled thinning rates represents a real difference between the eastern and western Antarctic Peninsula. This may reflect a reduced influence of CDW on the eastern side of the Antarctic Peninsula (cf. Hodgson et al., 2006; Bentley et al., 2009) leading the ice shelves in this area to be more resilient and preserving their buttressing effect. Additionally, there is a difference in the timing of thinning onset between the western and eastern Antarctic Peninsula sites. This is consistent with previous suggestions of earlier deglaciation on the west side compared with the east (Evans et al., 2005; Ó Cofaigh et al., 2005; Hodgson et al., 2006; Bentley et al., 2009). However, given the limited amount of data, these observations remain speculative and further studies on early Holocene glacier evolution in the Antarctic Peninsula are required to further elucidate the controls on deglaciation.

Broadly, palaeo-thinning rates in the interior parts of the Weddell and Ross Sea sectors are lower than the rates observed at sites more proximal to the ocean (with the notable exception of the Thomas Hills – discussed in section 5.1). This is evident in the Ross Sea sector where rates decrease as latitude increases. Modern observations demonstrate that dynamic thinning occurs at higher rates closer to the grounding line. For example on Pine Island Glacier thinning rates, as measured by in situ GPS, decrease from 3.65 m yr^{-1} at a distance of 55 km from the grounding line to 1.05 m yr^{-1} at 171 km from the grounding line (Scott et al., 2009). The interior Weddell/Ross Sea sites where palaeo-thinning is recorded would have been located further from the grounding line as it retreated following the LGM (cf. Bentley et al., 2014) and were likely less susceptible to rapid thinning. Additionally, these inner sites have likely retained the buttressing of the Ronne-Filchner and Ross Ice Shelves throughout much, if not all, of the Holocene.

At all sites thinning is focused in the Holocene (cf. Hein et al., 2016; Spector et al., 2017). In the Ross Sea sector there is a complex temporal and spatial pattern of thinning onset. The earliest modelled onset occurs at sites 1 and 2, (Beardmore and Shackleton Glaciers; cf. Spector et al., 2017) where thinning begins at c. 12 ka. Further to the south, sites 6-8 evidence thinning onset after 10 ka. Earlier thinning onset at more northerly sites could be inferred to reflect a general North–South migration of the grounding line (cf. Conway et al., 1999; Ackert, 2008) with concomitant reduction in buttressing stresses first affecting more northerly sites. However, this simple scenario does not account for the later onset of thinning at c. 7 ka at Mackay Glacier (cf. Jones et al., 2015). Recent studies have proposed a more complex model of Ross Sea Basin deglaciation that accounts for bathymetry and incorporates early deglaciation of the central Ross Sea Basin and an early Holocene readvance of East Antarctic outlet glaciers (Halberstadt et al., 2016; Lee et al., 2017). It may be that the later thinning of Mackay Glacier relates to retreat from this readvance rather than early Holocene deglaciation of the central Ross Sea. The complexity in the temporal pattern of thinning is also observed at sites 16-19 (Figure 10; Stone et al., 2003), where thinning begins at different times between 9 ka and 3 ka within a relatively restricted geographical area. Within the Weddell Sea sector the onset of thinning ranges from 9.4 – 7.4 ka in the Ellsworth Mountains (Figure 10, sites 14 and 15; Bentley et al., 2010; Hein et al., 2016) and 8.7 – 5.8 ka in the Pensacola Mountains (Figure 10, sites 11-13; Balco et al., 2016; Bentley et al., 2017). Importantly, the geological data do not directly evidence a single common forcing for thinning as they record thinning occurring in different places at different times. Instead the data highlight a complex response of the AISs to external forcing factors. This response was likely influenced by internal feedbacks, such as trough geometry, resulting in temporal variability in thinning onset during deglaciation.

Despite this complexity the overall timing of thinning does allow some inferences to be drawn regarding Antarctica's contribution to sea-level rise during the last deglaciation. Firstly, as noted above, all sites evidence thinning commencing from the early Holocene onwards (Figure 11). Antarctica has been proposed as a major contributor to Meltwater Pulse 1A (MWP-1A) (Clark et al., 2002; Weber et al., 2014), a eustatic sea-level rise of >10 m dated to 14.7-14.3 ka (Deshcamps et al., 2012). No thinning rate sites have MC estimates of thinning onset that overlap with the timing of MWP-1A (Figure 11), with thinning focused in the Holocene at all sites (cf. Hein et al., 2016; Spector et al., 2017). While acknowledging that the MC estimates of thinning onset are minimum ages it may be expected that, if thinning was ongoing at these sites during MWP-1A, then at least some of the thinning onset ages would overlap or pre-date this time. Notably, at sites with constraints on maximum ice elevation (e.g. weathering limit or moraine) such as those in the Ellsworth Mountains (Bentley et al., 2010; Hein at al., 2016), Prince Charles Mountains (White et al., 2011), and the Transantarctic Mountains (Todd et al., 2010; Jones et al., 2015), thinning onsets, as constrained by the Bayesian boundary ages, also significantly post-date MWP-1A. It is important to emphasise that the current absence of evidence is not evidence of absence and an Antarctic contribution to MWP-1A could be sourced from areas of Antarctica without suitable SED data (e.g. most of East Antarctica, or the central Ross Sea/Weddell Sea embayments). However the evidence presented here accords with recent studies that have not identified the potential Antarctic sources of MWP-1A from terrestrial studies using SED (Bentley et al., 2014; Spector et al., 2017).

Finally, some data-constrained models have Antarctica's contribution to deglacial sea-level rise continuing into the Holocene (Mackintosh et al., 2011; Argus et al., 2014; Briggs et al., 2014). Our compilation, while including some of the said data constraints, also includes newly available data not used in those models. All available SED sites with constraints on Antarctic thinning since the LGM currently suggest that the majority of mass loss from these sectors occurred during the Holocene, with widespread thinning occurring in the mid-Holocene (Figure 11). This timing of mass loss is also consistent with estimates of the timing of Antarctic deglaciation derived from far-field eustatic sea-level records (Mauz et al., 2015).

6. <u>Conclusions</u>

We have compiled exposure ages from a total of 23 sites around Antarctica that constrain, or have the potential to constrain, past ice sheet thinning. By taking a consistent approach to quality control and modelling of past thinning rates we present an internally consistent data set for use in a forthcoming model-data comparison exercise. This is the first compilation of palaeo-thinning rates in Antarctica and provides an opportunity to compare the modelled rates to contemporary patterns and magnitudes of thinning.

Thinning rates, as determined by MC linear regression analysis, are sensitive to the distribution of exposure ages, both in time and space. Consequently, sampling strategies can be designed to account for this with accurate constraints from the top and bottom of a transect being the most important for use in linear regression analysis. MC analysis can produce both ranges and single values (best fit, median) for past thinning rates. These values can be sensitive to, and are influenced by, the distribution of exposure ages within transects. Consequently, there remains a need to use some degree of subjective judgement, both in deciding which metric to use in model-data comparisons, and in interrogating the data in the cases of disagreement.

When constrained over centennial timescales past rates of thinning are comparable to modern rates. This implies that modern thinning has the potential to be sustained for some time into the future. Palaeo-thinning rates are lower than modern observations when constrained on millennial timescales. This difference is potentially due to the locations of sampling sites within ice drainage basins and/or averaging effects when the periods of time over which past thinning rates are reconstructed are orders of magnitude greater than the length of modern observations. Notably the highest palaeo-rates of thinning occur in regions that are characterised by high rates of contemporary thinning, namely the Amundsen Sea and Antarctic Peninsula regions, suggesting that similar mechanisms to those that drive modern thinning may have operated in the past. Both the MC analysis and Bayesian outlier detection produce age estimates for the onset of past thinning. Although these constraints are usually minimum ages for thinning onset they all post-date MWP-1A, and no transect has thinning occurring during MWP-1A (as constrained by the exposure ages). This suggests that any Antarctic contribution to this event may have been sourced from regions of the continent away from SED sites constraining thinning.

Acknowledgements

We would like to gratefully acknowledge the ICE-D Antarctica Database and specifically acknowledge Greg Balco for creating an invaluable resource to facilitate comparison of data from across the continent. We would also like to acknowledge all workers, scientific and logistic, whose considerable efforts have provided the cosmogenic exposure age data used in this contribution. MJB acknowledges support from NERC grants NE/J008176/1, NE/F014260/1 NE/K003674/1. PLW and MLP were supported by NERC grant NE/K003674/1. RSJ is supported by a Junior Research Fellowship COFUNDed between Durham University and the European Union under grant agreement number 609412. All data and code used in this submission is available from the authors on reasonable request.

References

Ackert, R.P, 2008. Swinging gate or Saloon doors: Do we need a new model of Ross Sea deglaciation. In *Fifteenth West Antarctic Ice Sheet Meeting, Sterling, Virginia* (Vol. 811).

Ackert, R.P., Barclay, D.J., Borns, H.W., Calkin, P.E., Kurz, M.D., Fastook, J.L. and Steig, E.J., 1999. Measurements of past ice sheet elevations in interior West Antarctica. *Science*, *286*, pp.276-280.

Altman, N. and Krzywinski, M., 2016. Points of Significance: Analyzing outliers: influential or nuisance? *Nature Methods, 13,* pp.281-282.

Argus, D.F., Peltier, W.R., Drummond, R. and Moore, A.W., 2014. The Antarctica component of postglacial rebound model ICE-6G_C (VM5a) based on GPS positioning, exposure age dating of ice thicknesses, and relative sea level histories. *Geophysical Journal International*, *198*, pp.537-563.

Balco, G., 2011. Contributions and unrealized potential contributions of cosmogenic-nuclide exposure dating to glacier chronology, 1990–2010. *Quaternary Science Reviews*, *30*, pp.3-27

Balco, G. and Schaefer, J.M., 2013. Exposure-age record of Holocene ice sheet and ice shelf change in the northeast Antarctic Peninsula. *Quaternary Science Reviews*, *59*, pp.101-111.

Balco, G., Todd, C., Huybers, K., Campbell, S., Vermeulen, M., Hegland, M., Goehring, B.M. and Hillebrand, T.R., 2016. Cosmogenic-nuclide exposure ages from the Pensacola Mountains adjacent to the Foundation Ice Stream, Antarctica. *American Journal of Science*, *316*, pp.542-577.

Bentley, M.J., 2010. The Antarctic palaeo record and its role in improving predictions of future Antarctic Ice Sheet change. *Journal of Quaternary Science*, *25*, pp.5-18.

Bentley, M.J., Fogwill, C.J., Kubik, P.W. and Sugden, D.E., 2006. Geomorphological evidence and cosmogenic $^{10}Be/^{26}Al$ exposure ages for the Last Glacial Maximum and deglaciation of the Antarctic Peninsula Ice Sheet. *Geological Society of America Bulletin*, *118*, pp.1149-1159.

Bentley, M.J., Hodgson, D.A., Smith, J.A., Ó Cofaigh, C., Domack, E.W., Larter, R.D., Roberts, S.J., Brachfeld, S., Leventer, A., Hjort, C. and Hillenbrand, C.D., 2009. Mechanisms of Holocene palaeoenvironmental change in the Antarctic Peninsula region. *The Holocene*, *19*, pp.51-69.

Bentley, M.J., Fogwill, C.J., Le Brocq, A.M., Hubbard, A.L., Sugden, D.E., Dunai, T.J. and Freeman, S.P., 2010. Deglacial history of the West Antarctic Ice Sheet in the Weddell Sea embayment: Constraints on past ice volume change. *Geology*, *38*, pp.411-414.

Bentley, M.J., Johnson, J.S., Hodgson, D.A., Dunai, T., Freeman, S.P.H.T. and Cofaigh, C.Ó., 2011. Rapid deglaciation of Marguerite Bay, western Antarctic Peninsula in the early Holocene. *Quaternary Science Reviews*, *30*, pp.3338-3349.

Bentley, M.J., Ó Cofaigh, C., Anderson, J.B., Conway, H., Davies, B., et al., 2014. A community-based geological reconstruction of Antarctic Ice Sheet deglaciation since the Last Glacial Maximum. *Quaternary Science Reviews*, *100*, pp.1-9.

Bentley, M.J., Hein, A.S., Sugden, D.E., Whitehouse, P.L., Shanks, R., Xu, S. and Freeman, S.P.H.T., 2017. Deglacial history of the Pensacola Mountains, Antarctica from glacial geomorphology and cosmogenic nuclide surface exposure dating. *Quaternary Science Reviews*, *158*, pp.58-76.

Blockley, S.P.E., Ramsey, C.B. and Higham, T.F.G., 2008. The Middle to Upper Paleolithic transition: dating, stratigraphy, and isochronous markers. *Journal of Human Evolution*, *55*(5), pp.764-771.

Briggs, R.D. and Tarasov, L., 2013. How to evaluate model-derived deglaciation chronologies: a case study using Antarctica. *Quaternary Science Reviews*, *63*, pp.109-127.

Briggs, R.D., Pollard, D. and Tarasov, L., 2014. A data-constrained large ensemble analysis of Antarctic evolution since the Eemian. *Quaternary Science Reviews*, *103*, pp.91-115.

Bronk Ramsey, C., 2008. Deposition models for chronological records. *Quaternary Science Reviews*, *27*, pp.42-60.

Bronk Ramsey, C., 2009a. Bayesian analysis of radiocarbon dates. *Radiocarbon*, *51*, pp.337-360.

Bronk Ramsey, C., 2009b. Dealing with outliers and offsets in radiocarbon dating. *Radiocarbon*, *51*, pp.1023-1045.

Bronk Ramsey, C., 2017. OxCal 4.3. https://c14.arch.ox.ac.uk/oxcal/OxCal.html.

Buck, C.E., Cavanagh, W.G. and Litton, C.D., 1996. *Bayesian approach to interpreting archaeological data*. Wiley.

Cahill, N., Kemp, A.C., Horton, B.P. and Parnell, A.C., 2015. Modeling sea-level change using errors-in-variables integrated Gaussian processes. *The Annals of Applied Statistics*, *9*, pp.547-571.

Chiverrell, R.C., Thrasher, I.M., Thomas, G.S., Lang, A., Scourse, J.D., van Landeghem, K.J., McCarroll, D., Clark, C.D., Cofaigh, C.Ó., Evans, D.J. and Ballantyne, C.K., 2013. Bayesian modelling the retreat of the Irish Sea Ice Stream. *Journal of Quaternary Science*, *28*, pp.200-209.

Clark, C.D., Hughes, A.L., Greenwood, S.L., Jordan, C. and Sejrup, H.P., 2012. Pattern and timing of retreat of the last British-Irish Ice Sheet. *Quaternary Science Reviews*, *44*, pp.112-146.

Clark, P.U., Mitrovica, J.X., Milne, G.A. and Tamisiea, M.E., 2002. Sea-level fingerprinting as a direct test for the source of global meltwater pulse 1A. *Science*, *295*, pp.2438-2441.

Clark, P.U., Dyke, A.S., Shakun, J.D., Carlson, A.E., Clark, J., Wohlfarth, B., Mitrovica, J.X., Hostetler, S.W. and McCabe, A.M., 2009. The last glacial maximum. *Science*, *325*, pp.710-714.

Conway, H., Hall, B.L., Denton, G.H., Gades, A.M. and Waddington, E.D., 1999. Past and future grounding-line retreat of the West Antarctic Ice Sheet. *Science*, *286*, pp.280-283.

Corbett, L.B., Bierman, P.R. and Rood, D.H., 2016. An approach for optimizing in situ cosmogenic ^{10}Be sample preparation. *Quaternary Geochronology*, *33*, pp.24-34.

De Angelis, H. and Skvarca, P., 2003. Glacier surge after ice shelf collapse. *Science*, *299*, pp.1560-1562.

DeConto, R.M. and Pollard, D., 2016. Contribution of Antarctica to past and future sea-level rise. *Nature*, *531*, pp.591-597.

Deschamps, P., Durand, N., Bard, E., Hamelin, B., Camoin, G., Thomas, A.L., Henderson, G.M., Okuno, J.I. and Yokoyama, Y., 2012. Ice-sheet collapse and sea-level rise at the Bølling warming 14,600 years ago. *Nature*, *483*, pp. 559-564.

Ely, J. C., Clark, C. D., Small, D., and Hindmarsh, R. C. A. 2018. ATAT 1.0, an Automated Timing Accordance Tool for comparing ice-sheet model output with geochronological data, *Geoscientific Model Development Discussions*, https://doi.org/10.5194/gmd-2018-12, in review.

Evans, J., Pudsey, C.J., Ó Cofaigh, C., Morris, P. and Domack, E., 2005. Late Quaternary glacial history, flow dynamics and sedimentation along the eastern margin of the Antarctic Peninsula Ice Sheet. *Quaternary Science Reviews*, *24*, pp.741-774.

Flament, T. and Rémy, F., 2012. Dynamic thinning of Antarctic glaciers from along-track repeat radar altimetry. *Journal of Glaciology*, *58*, pp.830-840.

Friedl, P., Seehaus, T.C., Wendt, A., Braun, M.H. and Höppner, K., 2018. Recent dynamic changes on Fleming Glacier after the disintegration of Wordie Ice Shelf, Antarctic Peninsula. *The Cryosphere*, *12*, pp.1347-1365.

Glasser, N.F., Davies, B.J., Carrivick, J.L., Rodés, A., Hambrey, M.J., Smellie, J.L. and Domack, E., 2014. Ice-stream initiation, duration and thinning on James Ross Island, northern Antarctic Peninsula. *Quaternary Science Reviews*, *86*, pp.78-88.

Graf, K.E., 2009. "The Good, the Bad, and the Ugly": Evaluating the radiocarbon chronology of the middle and late Upper Paleolithic in the Enisei River valley, south-central Siberia. *Journal of Archaeological Science*, *36*, pp.694-707.

Golledge, N.R., Fogwill, C.J., Mackintosh, A.N. and Buckley, K.M., 2012. Dynamics of the last glacial maximum Antarctic ice-sheet and its response to ocean forcing. *Proceedings of the National Academy of Sciences*, *109*, pp.16052-16056.

Halberstadt, A.R.W., Simkins, L.M., Greenwood, S.L. and Anderson, J.B., 2016. Past ice-sheet behaviour: Retreat scenarios and changing controls in the Ross Sea, Antarctica. *The Cryosphere*, *10*, pp.1003-1020.

Hall, B.L. and Denton, G.H., 1999. New relative sea-level curves for the southern Scott Coast, Antarctica: evidence for Holocene deglaciation of the western Ross Sea. *Journal of Quaternary Science*, *14*, pp.641-650.

Hall, B.L. and Denton, G.H., 2000. Radiocarbon chronology of Ross Sea drift, eastern Taylor Valley, Antarctica: Evidence for a grounded ice sheet in the Ross Sea at the last glacial maximum. *Geografiska Annaler: Series A, Physical Geography*, *82*, pp.305-336.

Harig, C. and Simons, F.J., 2015. Accelerated West Antarctic ice mass loss continues to outpace East Antarctic gains. *Earth and Planetary Science Letters*, *415*, pp.134-141.

Hein, A.S., Marrero, S.M., Woodward, J., Dunning, S.A., Winter, K., Westoby, M.J., Freeman, S.P., Shanks, R.P. and Sugden, D.E., 2016. Mid-Holocene pulse of thinning in the Weddell Sea sector of the West Antarctic ice sheet. *Nature communications*, *7*, 12511.

Heroy, D.C. and Anderson, J.B., 2007. Radiocarbon constraints on Antarctic Peninsula ice sheet retreat following the Last Glacial Maximum (LGM). *Quaternary Science Reviews*, *26*, pp.3286-3297.

Hillenbrand, C.D., Smith, J.A., Hodell, D.A., Greaves, M., Poole, C.R., Kender, S., Williams, M., Andersen, T.J., Jernas, P.E., Elderfield, H. and Klages, J.P., 2017. West Antarctic Ice Sheet retreat driven by Holocene warm water incursions. *Nature*, *547*, pp.43-48.

Hodgson, D.A., Bentley, M.J., Roberts, S.J., Smith, J.A., Sugden, D.E. and Domack, E.W., 2006. Examining Holocene stability of Antarctic Peninsula ice shelves. *Eos, Transactions American Geophysical Union*, *87*, pp.305-308.

Hughes, A.L., Gyllencreutz, R., Lohne, Ø.S., Mangerud, J. and Svendsen, J.I., 2016. The last Eurasian ice sheets–a chronological database and time-slice reconstruction, DATED-1. *Boreas*, *45*, pp.1-45.

Jacobs, S.S., Jenkins, A., Giulivi, C.F. and Dutrieux, P., 2011. Stronger ocean circulation and increased melting under Pine Island Glacier ice shelf. *Nature Geoscience*, *4*, pp.519-523.

Jamieson, S.S., Vieli, A., Cofaigh, C.Ó., Stokes, C.R., Livingstone, S.J. and Hillenbrand, C.D., 2014. Understanding controls on rapid ice-stream retreat during the last deglaciation of Marguerite Bay, Antarctica, using a numerical model. *Journal of Geophysical Research: Earth Surface*, *119*, pp.247-263.

Jenkins, A., Dutrieux, P., Jacobs, S.S., McPhail, S.D., Perrett, J.R., Webb, A.T. and White, D., 2010. Observations beneath Pine Island Glacier in West Antarctica and implications for its retreat. *Nature Geoscience*, *3*, pp.468-472.

Johnson, J.S., Bentley, M.J. and Gohl, K., 2008. First exposure ages from the Amundsen Sea embayment, West Antarctica: The late Quaternary context for recent thinning of Pine Island, Smith, and Pope Glaciers. *Geology*, *36*, pp.223-226.

Johnson, J.S., Smellie, J.L., Nelson, A.E. and Stuart, F.M., 2009. History of the Antarctic Peninsula Ice Sheet since the early Pliocene—evidence from cosmogenic dating of Pliocene lavas on James Ross Island, Antarctica. *Global and Planetary Change*, *69*, pp.205-213.

Johnson, J.S., Bentley, M.J., Smith, J.A., Finkel, R.C., Rood, D.H., Gohl, K., Balco, G., Larter, R.D. and Schaefer, J.M., 2014. Rapid thinning of Pine Island Glacier in the early Holocene. *Science*, pp.999-1001.

Jones, R.S., Mackintosh, A.N., Norton, K.P., Golledge, N.R., Fogwill, C.J., Kubík, P.W., Christl, M. and Greenwood, S.L., 2015. Rapid Holocene thinning of an East Antarctic outlet glacier driven by marine ice sheet instability. *Nature communications*, *6*, 8910.

Jones, R.S., Small D., Cahill N., Bentley, M.J. and Whitehouse, P.L, 2018. iceTEA: Tools for plotting and analysing cosmogenic-nuclide surface-exposure data from former ice margins. In review at *Quaternary Geochronology.*

Joughin, I., Smith, B.E. and Medley, B., 2014. Marine ice sheet collapse potentially under way for the Thwaites Glacier Basin, West Antarctica. *Science*, *344*, pp.735-738.

Joy, K., Fink, D., Storey, B., De Pascale, G.P., Quigley, M. and Fujioka, T., 2017. Cosmogenic evidence for limited local LGM glacial expansion, Denton Hills, Antarctica. *Quaternary Science Reviews*, *178*, pp.89-101.

Kemp, A.C., Hill, T.D., Vane, C.H., Cahill, N., Orton, P.M., Talke, S.A., Parnell, A.C., Sanborn, K. and Hartig, E.K., 2017. Relative sea-level trends in New York City during the past 1500 years. *The Holocene*, *27*, pp.1169-1186.

Khan, N.S., Ashe, E., Shaw, T.A., Vacchi, M., Walker, J., Peltier, W.R., Kopp, R.E. and Horton, B.P., 2015. Holocene relative sea-level changes from near-, intermediate-, and far-field locations. *Current Climate Change Reports*, *1*, pp.247-262.

Kilfeather, A.A., Cofaigh, C.Ó., Lloyd, J.M., Dowdeswell, J.A., Xu, S. and Moreton, S.G., 2011. Ice-stream retreat and ice-shelf history in Marguerite Trough, Antarctic Peninsula: Sedimentological and foraminiferal signatures. *Geological Society of America Bulletin*, *123*, pp.997-1015.

King, M.A., Bingham, R.J., Moore, P., Whitehouse, P.L., Bentley, M.J. and Milne, G.A., 2012. Lower satellite-gravimetry estimates of Antarctic sea-level contribution. *Nature*, *491*, pp.586.

Konrad, H., Shepherd, A., Gilbert, L., Hogg, A.E., McMillan, M., Muir, A. and Slater, T., 2018. Net retreat of Antarctic glacier grounding lines. *Nature Geoscience*, *11*, pp.258.

Lambeck, K., Rouby, H., Purcell, A., Sun, Y. and Sambridge, M., 2014. Sea level and global ice volumes from the Last Glacial Maximum to the Holocene. *Proceedings of the National Academy of Sciences*, *111*, pp.15296-15303.

Lecavalier, B.S., Milne, G.A., Simpson, M.J., Wake, L., Huybrechts, P., Tarasov, L., Kjeldsen, K.K., Funder, S., Long, A.J., Woodroffe, S. and Dyke, A.S., 2014. A model of Greenland ice sheet deglaciation constrained by observations of relative sea level and ice extent. *Quaternary Science Reviews*, *102*, pp.54-84.

Lee, J.I., McKay, R.M., Golledge, N.R., Yoon, H.I., Yoo, K.C., Kim, H.J. and Hong, J.K., 2017. Widespread persistence of expanded East Antarctic glaciers in the southwest Ross Sea during the last deglaciation. *Geology*, *45*, pp.403-406.

Leventer, A., Domack, E., Barkoukis, A., McAndrews, B. and Murray, J., 2002. Laminations from the Palmer Deep: A diatom-based interpretation. *Paleoceanography*, *17*, PA000624.

Li, X., Rignot, E., Morlighem, M., Mouginot, J. and Scheuchl, B., 2015. Grounding line retreat of Totten Glacier, East Antarctica, 1996 to 2013. *Geophysical Research Letters*, *42*, pp.8049-8056.

Lifton, N., Sato, T. and Dunai, T.J., 2014. Scaling in situ cosmogenic nuclide production rates using analytical approximations to atmospheric cosmic-ray fluxes. *Earth and Planetary Science Letters*, *386*, pp.149-160.

Locarnini, R.A., Mishonov, A.V., Antonov, J.I., Boyer, T.P., Garcia, H.E., Baranova, O.K., Zweng, M.M., Paver, C.R., Reagan, J.R., Johnson, D.R., Hamilton, M., and Seidov, D., 2013*. World Ocean Atlas 2013, Volume 1: Temperature.* Levitus, S. Ed., Mishonov, A. Technical Ed.; NOAA Atlas NESDIS 73, 40 pp.

Mackintosh, A., White, D., Fink, D., Gore, D.B., Pickard, J. and Fanning, P.C., 2007. Exposure ages from mountain dipsticks in Mac. Robertson Land, East Antarctica, indicate little change in ice-sheet thickness since the Last Glacial Maximum. *Geology*, *35*, pp.551-554.

Mackintosh, A., Golledge, N., Domack, E., Dunbar, R., Leventer, A., White, D., Pollard, D., DeConto, R., Fink, D., Zwartz, D. and Gore, D., 2011. Retreat of the East Antarctic ice sheet during the last glacial termination. *Nature Geoscience*, *4*, 195.

Mauz, B., Ruggieri, G. and Spada, G., 2015. Terminal Antarctic melting inferred from a far-field coastal site. *Quaternary Science Reviews*, *116*, pp.122-132.

McMillan, M., Shepherd, A., Sundal, A., Briggs, K., Muir, A., Ridout, A., Hogg, A. and Wingham, D., 2014. Increased ice losses from Antarctica detected by CryoSat-2. *Geophysical Research Letters*, *41*, pp.3899-3905.

Miles, B.W.J., Stokes, C.R., Vieli, A. and Cox, N.J., 2013. Rapid, climate-driven changes in outlet glaciers on the Pacific coast of East Antarctica. *Nature*, *500*, pp.563.

Ó Cofaigh, C, Dowdeswell, J.A., Allen, C.S., Hiemstra, J.F., Pudsey, C.J., Evans, J. and Evans, D.J., 2005. Flow dynamics and till genesis associated with a marine-based Antarctic palaeo-ice stream. *Quaternary Science Reviews*, *24*, pp.709-740.

Park, J.W., Gourmelen, N., Shepherd, A., Kim, S.W., Vaughan, D.G. and Wingham, D.J., 2013. Sustained retreat of the Pine Island Glacier. *Geophysical Research Letters*, *40*, pp.2137-2142.

Peck, V.L., Allen, C.S., Kender, S., McClymont, E.L. and Hodgson, D.A., 2015. Oceanographic variability on the West Antarctic Peninsula during the Holocene and the influence of upper circumpolar deep water. *Quaternary Science Reviews*, *119*, pp.54-65.

Pritchard, H.D., Arthern, R.J., Vaughan, D.G. and Edwards, L.A., 2009. Extensive dynamic thinning on the margins of the Greenland and Antarctic ice sheets. *Nature*, *461*, pp.971.

Pritchard, H.D., Ligtenberg, S.R.M., Fricker, H.A., Vaughan, D.G., Van den Broeke, M.R. and Padman, L., 2012. Antarctic ice-sheet loss driven by basal melting of ice shelves. *Nature*, *484*, pp.502-505.

Reese, R., Gudmundsson, G.H., Levermann, A. and Winkelmann, R., 2018. The far reach of ice-shelf thinning in Antarctica. *Nature Climate Change*, *8*, p.53-57.

Rignot, E. and Jacobs, S.S., 2002. Rapid bottom melting widespread near Antarctic ice sheet grounding lines. *Science*, *296*, pp.2020-2023.

Rignot, E., Casassa, G., Gogineni, P., Krabill, W., Rivera, A.U. and Thomas, R., 2004. Accelerated ice discharge from the Antarctic Peninsula following the collapse of Larsen B ice shelf. *Geophysical Research Letters*, *31*.

Rignot, E., Velicogna, I., van den Broeke, M.R., Monaghan, A. and Lenaerts, J.T., 2011. Acceleration of the contribution of the Greenland and Antarctic ice sheets to sea level rise. *Geophysical Research Letters*, *38*, L05503.

Rignot, E., Mouginot, J., Morlighem, M., Seroussi, H. and Scheuchl, B., 2014. Widespread, rapid grounding line retreat of Pine Island, Thwaites, Smith, and Kohler glaciers, West Antarctica, from 1992 to 2011. *Geophysical Research Letters*, *41*, pp.3502-3509.

Rinterknecht, V.R., Clark, P.U., Raisbeck, G.M., Yiou, F., Bitinas, A., Brook, E.J., Marks, L., Zelčs, V., Lunkka, J.P., Pavlovskaya, I.E. and Piotrowski, J.A., 2006. The last deglaciation of the southeastern sector of the Scandinavian Ice Sheet. *Science*, *311*, pp.1449-1452.

Rood, D.H., Brown, T.A., Finkel, R.C. and Guilderson, T.P., 2013. Poisson and non-Poisson uncertainty estimations of ^{10}Be/^{9}Be measurements at LLNL–CAMS. *Nuclear Instruments and Methods in Physics Research Section B: Beam Interactions with Materials and Atoms*, *294*, pp.426-429.

Scambos, T.A., Bohlander, J.A., Shuman, C.U. and Skvarca, P., 2004. Glacier acceleration and thinning after ice shelf collapse in the Larsen B embayment, Antarctica. *Geophysical Research Letters*, *31*.

Scheuchl, B., Mouginot, J., Rignot, E., Morlighem, M. and Khazendar, A., 2016. Grounding line retreat of Pope, Smith, and Kohler Glaciers, West Antarctica, measured with Sentinel-1a radar interferometry data. *Geophysical Research Letters*, *43*, pp.8572-8579.

Schröder, L., Horwath, M., Dietrich, R. and Helm, V., 2018. Four decades of surface elevation change of the Antarctic Ice Sheet from multi-mission satellite altimetry. The Cryosphere Discussions, 1-25, 2018.

Scott, J.B., Gudmundsson, G.H., Smith, A.M., Bingham, R.G., Pritchard, H.D. and Vaughan, D.G., 2009. Increased rate of acceleration on Pine Island Glacier strongly coupled to changes in gravitational driving stress. *The Cryosphere, 3,* pp.125-131.

Shepherd, A., Wingham, D.J., Mansley, J.A. and Corr, H.F., 2001. Inland thinning of pine island Glacier, West Antarctica. *Science*, *291*, pp.862-864.

Shepherd, A., Wingham, D.J. and Mansley, J.A., 2002. Inland thinning of the Amundsen Sea sector, West Antarctica. *Geophysical Research Letters*, *29*(10).

Shepherd, A., Ivins, E.R., Geruo, A., Barletta, V.R., Bentley, M.J., Bettadpur, S., Briggs, K.H., Bromwich, D.H., Forsberg, R., Galin, N. and Horwath, M., 2012. A reconciled estimate of ice-sheet mass balance. *Science*, *338*, pp.1183-1189.

Shepherd, A., Ivins, E., Rignot, E., Smith, B., van den Broeke, M., Velicogna, I., Whitehouse, P., Briggs, K., Joughin, I., Krinner, G. and Nowicki, S., 2018. Mass balance of the Antarctic Ice Sheet from 1992 to 2017. *Nature*, *556*, pp.219-222

Small, D., Clark, C.D., Chiverrell, R.C., Smedley, R.K., Bateman, M.D., Duller, G.A., Ely, J.C., Fabel, D., Medialdea, A. and Moreton, S.G., 2017. Devising quality assurance procedures for assessment of legacy geochronological data relating to deglaciation of the last British-Irish Ice Sheet. *Earth-science reviews*, *164*, pp.232-250.

Small, D., Smedley, R.K., Chiverrell, R.C., Scourse, J.D., Ó Cofaigh, C., Duller, G.A., McCarron, S., Burke, M.J., Evans, D.J., Fabel, D. and Gheorghiu, D.M., Thomas, G.S.P., and Xu, S., 2018. Trough geometry was a greater influence than climate-ocean forcing in regulating retreat of the marine-based Irish-Sea Ice Stream. *Geological Society of America Bulletin*. https://doi.org/10.1130/B31852.1.

Smith, J.A., Bentley, M.J., Hodgson, D.A., Roberts, S.J., Leng, M.J., Lloyd, J.M., Barrett, M.S., Bryant, C. and Sugden, D.E., 2007. Oceanic and atmospheric forcing of early Holocene ice shelf retreat, George VI Ice Shelf, Antarctica Peninsula. *Quaternary Science Reviews*, *26*, pp.500-516.

Spector, P., Stone, J., Cowdery, S.G., Hall, B., Conway, H. and Bromley, G., 2017. Rapid early-Holocene deglaciation in the Ross Sea, Antarctica. *Geophysical Research Letters*, *44*, pp.7817-7825.

Stenoien, M.D. and Bentley, C.R., 2000. Pine Island Glacier, Antarctica: A study of the catchment using interferometric synthetic aperture radar measurements and radar altimetry. *Journal of Geophysical Research: Solid Earth*, *105*, pp.21761-21779.

Stocker, T.F., Qin, D., Plattner, G.K., Tignor, M., Allen, S.K., Boschung, J., Nauels, A., Xia, Y., Bex, V. and Midgley, P.M., 2013. IPCC, 2013: Climate Change 2013: The Physical Science Basis. Contribution of Working Group I to the Fifth Assessment Report of the Intergovernmental Panel on Climate Change, 1535 pp.

Stokes, C.R., Tarasov, L., Blomdin, R., Cronin, T.M., Fisher, T.G., Gyllencreutz, R., Hättestrand, C., Heyman, J., Hindmarsh, R.C., Hughes, A.L. and Jakobsson, M., 2015. On the reconstruction of palaeo-ice sheets: recent advances and future challenges. *Quaternary Science Reviews*, *125*, pp.15-49.

Stone, J.O., Balco, G.A., Sugden, D.E., Caffee, M.W., Sass, L.C., Cowdery, S.G. and Siddoway, C., 2003. Holocene deglaciation of Marie Byrd land, west Antarctica. *Science*, *299*, pp.99-102.

Tarasov, L. and Peltier, W.R., 2004. A geophysically constrained large ensemble analysis of the deglacial history of the North American ice-sheet complex. *Quaternary Science Reviews*, *23*, pp.359-388.

Tarasov, L., Dyke, A.S., Neal, R.M. and Peltier, W.R., 2012. A data-calibrated distribution of deglacial chronologies for the North American ice complex from glaciological modeling. *Earth and Planetary Science Letters*, *315*, pp.30-40.

Todd, C., Stone, J., Conway, H., Hall, B. and Bromley, G., 2010. Late Quaternary evolution of Reedy Glacier, Antarctica. *Quaternary Science Reviews*, *29*, pp.1328-1341

Velicogna, I., Sutterley, T.C. and Van Den Broeke, M.R., 2014. Regional acceleration in ice mass loss from Greenland and Antarctica using GRACE time-variable gravity data. *Geophysical Research Letters*, *41*, pp.8130-8137.

Weber, M.E., Clark, P.U., Kuhn, G., Timmermann, A., Sprenk, D., Gladstone, R., Zhang, X., Lohmann, G., Menviel, L., Chikamoto, M.O. and Friedrich, T., 2014. Millennial-scale variability in Antarctic ice-sheet discharge during the last deglaciation. *Nature*, *510*(7503), p.134.

White, D.A., Fink, D. and Gore, D.B., 2011. Cosmogenic nuclide evidence for enhanced sensitivity of an East Antarctic ice stream to change during the last deglaciation. *Geology*, *39*, pp.23-26.

Whitehouse, P.L., Bentley, M.J. and Le Brocq, A.M., 2012. A deglacial model for Antarctica: geological constraints and glaciological modelling as a basis for a new model of Antarctic glacial isostatic adjustment. *Quaternary Science Reviews*, *32*, pp.1-24.

Wingham, D.J., Wallis, D.W. and Shepherd, A., 2009. Spatial and temporal evolution of Pine Island Glacier thinning, 1995–2006. *Geophysical Research Letters*, *36*, L17501.

Wouters, B., Martin-Español, A., Helm, V., Flament, T., van Wessem, J.M., Ligtenberg, S.R., Van den Broeke, M.R. and Bamber, J.L., 2015. Dynamic thinning of glaciers on the Southern Antarctic Peninsula. *Science*, *348*, pp.899-903.

Figure Captions

Figure 1. Schematic diagram illustrating how samples from vertical transects can constrain past ice sheet surface elevation and thinning. The left hand panels illustrate exposure ages from a vertical transect and the evolution of the ice sheet surface from the LGM (t_0) to present. The right hand panels illustrate the concomitant evolution of a sample's ^{10}Be inventory under the scenarios. (A) The LGM ice sheet surface overtopped the uppermost sample which provides only a minimum constrain on ice sheet surface elevation. (B) The LGM ice sheet surface is below the uppermost surface and a sample (Sample B) from a lateral moraine constrains the timing and surface elevation of the LGM. In both scenarios thinning is constrained by samples with progressively lower concentrations of ^{10}Be, which would yield progressively younger exposure ages. In scenario B the uppermost sample becomes saturated with ^{10}Be.

Figure 2. Location map of Antarctica showing place names mentioned in the text and locations of transects where exposure ages are used to constrain past thinning rates. These are numbered as per Table 1. PIG = Pine Island Glacier, ThG = Thwaites Glacier, LG = Lambert Glacier, AmIS = Amery Ice Shelf, FIS = Filchner Ice Shelf, PIB = Pine Island bay, MB = Marguerite Bay. Base map is from Quantarctica GIS package compiled by the Norwegian Polar Institute (http://www.quantarctica.org/).

Figure 3. Bayesian age model output from OxCal 4.3 (Bronk Ramsey, 2017) for a simple sequence of exposure ages from a vertical transect (Sample 1 being the uppermost sample). The measured age distributions are shown in light grey with refined age distributions in darker grey. In this example Sample 4 was flagged as an outlier. The Bayesian model produces a refined age estimate for all samples, however for our purposes these were not considered in the Monte Carlo analysis. The black bars represent 68% and 95% confidence intervals. The modelled age distributions for the *boundaries* (“top” and “bottom”) provide minimum and maximum constraints on thinning onset and cessation respectively.

Figure 4. Flow chart of the approach taken to detect outliers using OxCal 4.3. See text for further description.

Figure 5. Example output from the Monte Carlo linear regression analysis. Transects from; A) Mount Hope (Spector et al., 2017), and B) Maish Nunatak (Johnson et al., 2014) with resulting distribution of modelled thinning rates (C: Mount Hope, D: Maish Nunatak) at 68% (dashed vertical lines) and 95% (dotted vertical lines). Note the x-axis is logarithmic. Note that the Maish

transect has a skewed distribution with a wider range of modelled thinning rates and a distinctly different median rate (red vertical line) vs*.* the 'best-fit' rate (blue vertical line).

Figure 6. Box and whisker plot summarising the modelled palaeo-thinning rates presented here. The box represents the 68% range, the whiskers represent the 95% range. The median thinning rate from the Monte Carlo analysis is shown with the target symbol, the 'best fit' thinning rate based on a linear regression through the mean values of the exposure ages is shown with the red diamond. Transect ID numbers are as per Table 3. Note that the y-axis is logarithmic.

Figure 7. The effect of extreme values on the gradient of a linear regression. (A) A hypothetical data-set of exposure ages showing a clear age-elevation trend. (B) The same data-set but with a younger exposure age from the middle elevation of the transect. (C) The same data-set as A but with a younger age from the bottom elevation of the transect. Note that the difference in 'best fit' thinning rates is greater for the second scenario.

Figure 8. Scatter plot of modern thinning rates (blue triangles) and palaeo thinning rates (red triangles) against the length of observations in years. For the palaeo-rates the duration of thinning is taken from the midpoints of the 95% modelled age distributions from the Monte Carlo linear regression analysis. Note that the axes are logarithmic. Triangles labelled *a* and *b* are the thinning rates from Mount Moses and Low Ridge respectively as calculated using all exposure ages from each site (cf. Johnson et al., 2014; Jones et al., 2015).

Figure 9. Palaeo-rates of thinning (circles) are shown against modern thinning rates (Pritchard et al., 2009) and present day ocean temperatures at 500 m depth (Locarnini et al., 2013; data from Quantarctica GIS package). Base map is from Quantarctica GIS package compiled by the Norwegian Polar Institute (http://www.quantarctica.org/).

Figure 10. Spatial distribution of the onset of thinning as inferred from the midpoint of the 95% modelled onset from the Monte Carlo linear regression analysis. Base map is from Quantarctica GIS package.

Figure 11. Monte Carlo modelled age ranges (95%) for onset of thinning plotted alongside ice volume equivalent global sea-level changes (dark blue line: Lambeck et al., 2014) and a modelled Antarctic contribution to sea-level change (dark red line: Briggs et al., 2014). The timing

of meltwater pulse 1A (MWP-1A) is shown with the blue shading (Deschamps et al., 2012). Transects are numbered as per Table 1.

Table 1. Location information of sites from which thinning rates are presented. ID numbers are used in subsequent figures. Elevation range is difference in altitude of uppermost and lowermost samples.

Site	Reference(s)	ID No.	Latitude (DD)	Longitude (DD)	Elevation range (m)
Mount Hope	Spector et al., 2017	1	-83.51	171.40	719
Mount Rigby/Karo	Spector et al., 2017	2	-85.52	-154.52	727
Mount Suess/Gondola	Jones et al., 2015	3	-77.04	161.64	208
Gondola (mid-lower)	Jones et al., 2015	4	-77.00	161.76	61
Low Ridge	Jones et al., 2015	5	-76.99	162.28	202
Reedy Glacier (Quartz Hills)	Todd et al., 2010	6	-85.90	-132.57	160
Reedy Glacier (Pip's Peak)	Todd et al., 2010	7	-85.43	-135.90	151
Reedy Glacier (Cohen's Nunatak)	Todd et al., 2010	8	-85.40	-136.20	104
Maish Nunatak	Johnson et al., 2014	9	-74.59	-99.45	99
Mount Moses	Johnson et al., 2014	10	-74.55	-99.20	141
Williams Hills	Balco et al., 2016; Bentley et al., 2017	11	-83.68	-58.81	413
Thomas Hills	Balco et al., 2016; Bentley et al., 2017	12	-84.38	-65.52	291
Mount Harper/Bragg	Bentley et al., 2017	13	-84.07	-57.06	236
Marble Hills	Bentley et al., 2010; Hein et al., 2016	14	-80.26	-82.13	485
Patriot Hills	Bentley et al., 2010; Hein et al., 2016	15	-80.33	-81.49	247
Mount Rea	Stone et al., 2003	16	-77.07	-145.57	572
Mount Darling	Stone et al., 2003	17	-77.27	-143.33	227
Mount Valkenburg	Stone et al., 2003	18	-77.31	-142.11	75
Fosdick Mountains	Stone et al., 2003	19	-76.54	-144.50	225
Mount Stinear	White et al., 2011	20	-73.04	66.42	323
Porquoi-Pas Island	Bentley et al., 2011	21	-67.59	-67.26	266
James Ross Island	Johnson et al., 2011; Glasser et al., 2014	22	-63.80	-57.83	198
Sjorden-Boydell	Balco et al., 2013	23	-64.23	-59.02	319

Table 2. Summary of total number of samples, final *OxCal* Bayesian agreement index (A) and total number of outliers excluded from each site.

Site	No. of samples	Final Bayesian $A_{overall}$	Outliers excluded
Mount Hope	28	62.5	4
Mount Rigby/Karo	21	124.1	0
Mount Suess/Gondola Upper	16	103.9	0
Gondola (mid-lower)	12	78	0
Low Ridge	10	123	1
Reedy Glacier (Quartz Hills)	25	64.6	10
Reedy Glacier (Pip's Peak)	7	108.7	0
Reedy Glacier (Cohen's Nunatak)	5	104.8	0
Maish Nunatak	6	158.4	1
Mount Moses	6	62.9	0
Williams Hills	17	70.3	5
Thomas Hills	15	79.9	9
Mount Harper/Bragg	12	81	5
Marble Hills	28	81.1	12
Patriot Hills	11	119.5	3
Mount Rea	15	93.2	2
Mount Darling	5	103.3	0
Mount Valkenburg	4	103.8	0
Fosdick Mountains	5	107.7	0
Mount Stinear	12	90.3	2
Porquoi-Pas Island	6	132.8	1
James Ross Island	7	74.2	2
Sjorden-Boydell	9	121	0

Table 3. Summary of thinning rates presented from each site derived from Monte Carlo linear regression analysis. 'Best-fit' rates are not presented for two sites (Thomas Hills and Pourquoi-Pas Island) as at these sites the best fit linear regression gave a negative slope and is thus rejected as physically implausible.

Site	ID No.	Min thinning rate (68%) m yr^{-1}	Max thinning rate (68%) m yr^{-1}	Min Thinning rate (95%) m yr^{-1}	Max Thinning rate (95%) m yr^{-1}	Best fit thinning rate m yr^{-1}	Median rate
Mount Hope	1	0.14	0.20	0.13	0.24	0.17	0.17
Mount Rigby/Karo	2	0.06	0.07	0.06	0.08	0.06	0.06
Mount Suess/Gondola Upper	3	0.12	0.32	0.09	1.20	0.17	0.17
Gondola Mid-lower	4	0.07	0.49	0.04	3.16	0.57	0.15
Low Ridge (all)	5	0.03	0.03	0.02	0.04	0.03	0.03
Low Ridge (subset n=5)	5a	0.12	0.65	0.08	3.62	0.39	0.23
Reedy Glacier (Quartz Hills)	6	0.01	0.03	0.01	0.06	0.02	0.02
Reedy Glacier (Pip's Peak)	7	0.23	0.99	0.17	5.39	0.43	0.38
Reedy Glacier (Cohen's Nunatak)	8	0.01	0.02	0.01	0.03	0.02	0.02
Maish Nunatak	9	0.19	1.24	0.12	7.09	1.16	0.38
Mount Moses (all)	10	0.06	0.12	0.05	0.21	0.08	0.08
Mount Moses (subset n= 3)	10a	0.24	1.52	0.15	10.19	1.67	0.49
Williams Hills	11	0.09	0.12	0.08	0.14	0.10	0.10
Thomas Hills	12	0.62	6.41	0.36	37.72	*N/A*	1.57
Mount Harper/Bragg	13	0.06	0.12	0.04	0.25	0.08	0.08
Marble Hills	14	0.06	0.09	0.06	0.12	0.08	0.08
Patriot Hills	15	0.05	0.08	0.04	0.11	0.06	0.06
Mount Rea	16	0.27	0.50	0.22	0.84	0.35	0.35
Mount Darling	17	0.04	0.05	0.04	0.05	0.04	0.04
Mount Valkenburg	18	0.02	0.03	0.02	0.03	0.02	0.02
Fosdick Mountains	19	0.08	0.09	0.08	0.09	0.09	0.09
Mount Stinear	20	0.20	1.19	0.13	6.86	0.76	0.38
Porquoi-Pas Island	21	0.25	1.81	0.16	12.35	*N/A*	0.53
James Ross Island	22	0.05	0.16	0.04	0.73	0.08	0.09
Sjorden-Boydell	23	0.08	0.09	0.07	0.10	0.08	0.08

Table 4. Comparison of thinning rates presented here and rates presented in original studies.

Reference	**Site**	**Metric**	**Published rates (m yr-1)**	**This study (m yr-1)**	**Notes**
Hein et al., 2016	Marble Hills	mean ± 1 s.d	0.21 ± 0.03	0.08 (median)	0.28 m yr-1 with samples used by Hein
Hein et al., 2016	Patriot Hills	mean ± 1 s.d	0.07 ± 0.01	0.06 (median)	-
Johnson et al., 2014	Mount Moses	95% range	0.08 - 5.90	0.05 - 0.21	0.15 - 10.45 m yr-1 (95%) when using three upper samples (cf. Johnson et al., 2014)
Johnson et al., 2014	Mount Moses	*best fit*	*1.67*	*0.08*	1.67 m yr-1 (best fit) when using three upper samples
Johnson et al., 2014	Maish Nunatak	95% range	0.13 - 5.50	0.12 - 7.09	-
Johnson et al., 2014	Maish Nunatak	*best fit*	*1.12*	*1.16*	-
Jones et al., 2015	Mount Suess/Gondola upper	95% range	0.33 - 0.80	0.09 - 1.07	-
Jones et al., 2015	Low Ridge	95% range	0.08 - 3.59	0.02 - 0.04	0.08 - 3.62 (95%) when using upper 5 samples (cf. Jones et al., 2015)

Table 5. Modelled timings for the onset and end of thinning as derived from Monte Carlo (MC) linear regression analysis and *OxCal* ‘Boundary’ command within Sequence model.

		MC 95% Onset		***MC 95% End***		***Bayesian Onset 95%***		***Bayesian End 95%***	
Site	**ID No.**	**Mid-range**	**+/-**	**Mid-range**	**+/-**	**Mid-range**	**+/-**	**Mid-range**	**+/-**
Mount Hope	1	12200	900	7600	700	12400	1200	7200	800
Mount Rigby/Karo	2	12200	1200	-100	1000	11500	1700	100	100
Mount Suess/Gondola Upper	3	6800	700	5400	800	7100	1000	4900	1300
Gondola Mid-lower	4	7000	600	6300	600	6900	600	6100	800
Low Ridge (all)	5	7600	1100	-200	1100	6900	1100	200	200
Low Ridge (subset n=5)	5a	6600	500	6000	500	6900	1100	5200	1500
Reedy Glacier (Quartz Hills)	6	10000	1200	6800	1400	10300	1400	6600	100
Reedy Glacier (Pip's Peak)	7	7400	300	7000	300	10300	3200	300	300
Reedy Glacier (Cohen’s Nunatak)	8	8600	2000	1400	1700	10300	3800	900	900
Maish Nunatak	9	7200	300	6800	400	7400	700	6700	700
Mount Moses (all)	10	7400	700	5400	700	8600	1000	5300	1300
Mount Moses (subset n= 3)	10a	7100	200	6900	200	8600	1000	7200	800
Williams Hills	11	8800	600	4300	5100	7900	900	4700	600
Thomas Hills	12	6800	500	6500	500	6900	500	6600	500
Mount Harper/Bragg	13	5800	1300	2400	1700	7200	1600	1800	1100
Marble Hills	14	9400	1000	5300	800	10200	1600	4200	1400
Patriot Hills	15	7400	1100	3100	1000	7400	2500	3800	500
Mount Rea	16	3300	400	2200	400	4100	1000	1700	700
Mount Darling	17	9200	200	3400	300	12100	3900	2100	2100
Mount Valkenburg	18	6600	500	3100	500	10600	4800	1900	1900
Fosdick Mountains	19	5100	100	2200	100	6200	2000	1300	1300
Mount Stinear	20	11400	1200	10300	800	11300	1100	9900	1200
Porquoi-Pas Island	21	11100	800	10300	800	11300	1100	10200	1200
James Ross Island	22	9700	1900	6600	1800	9100	1400	7100	1900
Sjorden-Boydell	23	7600	400	3400	400	8100	1400	2500	1300

Table 6. Alternate thinning rates from Monte Carlo analysis for sites where Bayesian outlier detection resulted in exclusion of ‘young’ erratics.

Site	Total samples in profile	Young sample(s) excluded	Alternate 68% range (m yr^{-1})	Alternate 95% range (m yr^{-1})	Alt. best fit (m yr^{-1})	Alt. median (m yr^{-1})
Low Ridge	10	CC93	0.03-0.19	0.02-0.90	0.19	0.16
Williams Hills	17	WIL-4	0.09-0.15	0.08-0.21	0.12	0.12
Mount Harper/Bragg	12	HAR-3	0.05-0.11	0.04-0.25	0.07	0.07
Marble Hills	28	MH12-16	0.08-0.15	0.06-0.25	0.10	0.10
Patriot Hills	11	PH12-28	0.06-0.14	0.05-0.34	0.09	0.09
James Ross Island	7	JOH-04	0.06-0.26	0.04-1.36	0.12	0.10

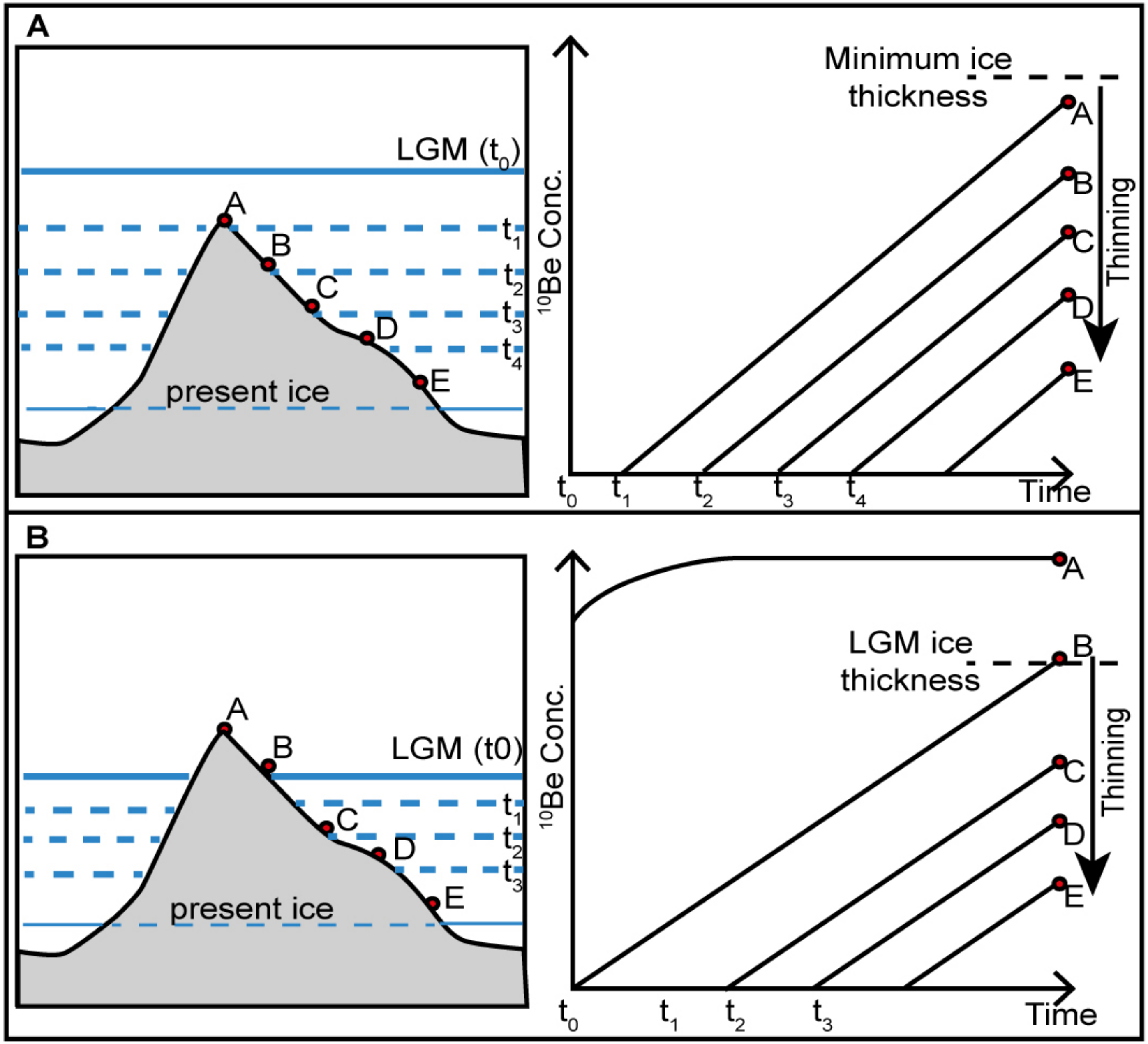

A
LGM (t_0)
A
B
C
D
E
t_1
t_2
t_3
t_4
present ice
Minimum ice thickness
^{10}Be Conc.
Thinning
t_0 t_1 t_2 t_3 t_4 Time
B
LGM (t0)
A
B
C
D
E
t_1
t_2
t_3
present ice
LGM ice thickness
^{10}Be Conc.
Thinning
t_0 t_1 t_2 t_3 Time

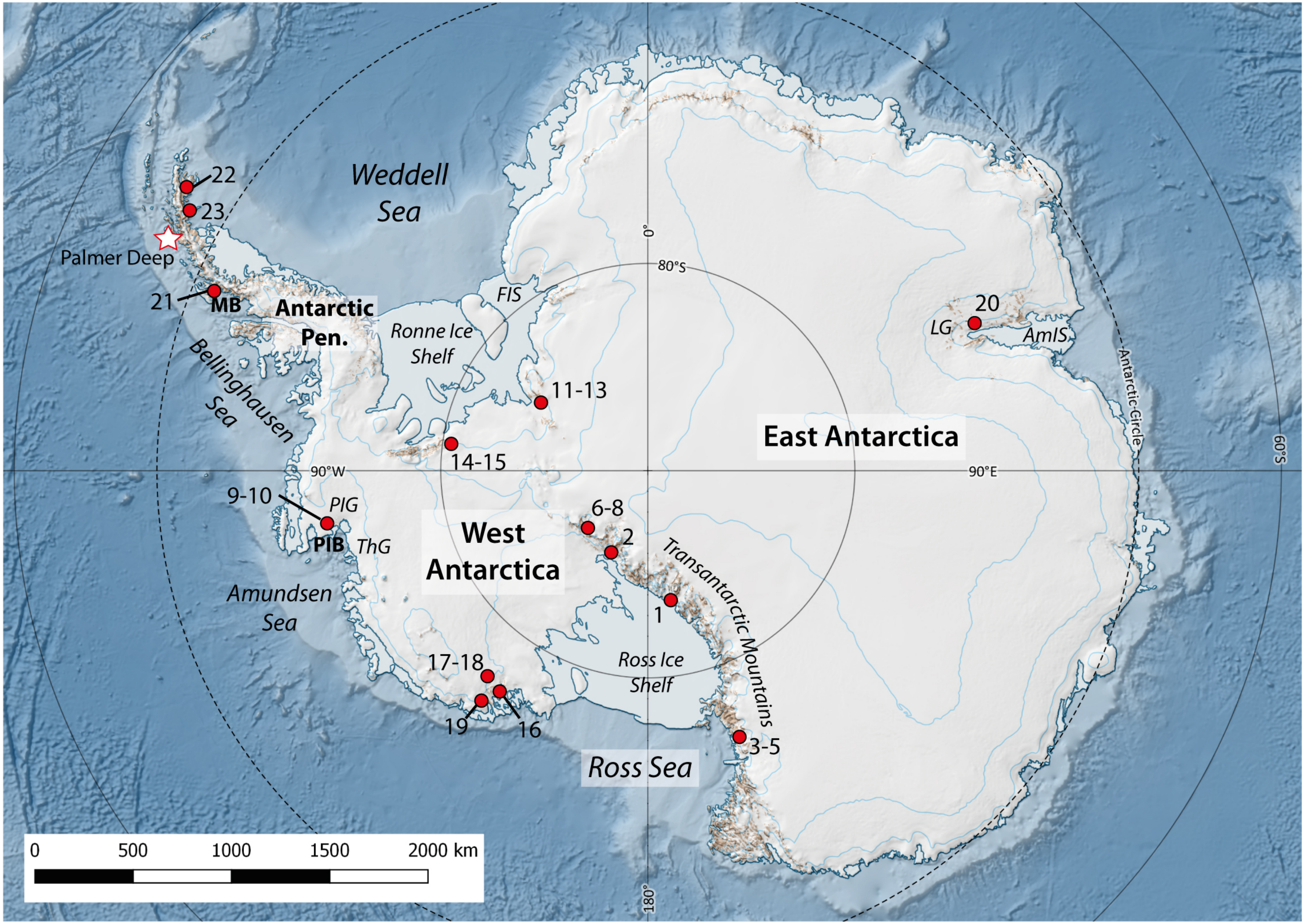

Weddell Sea
22
23
Palmer Deep
21
MB
Antarctic Pen.
Bellinghausen Sea
FIS
Ronne Ice Shelf
0°
80°S
20
LG
AmIS
Antarctic Circle
11-13
14-15
East Antarctica
90°W
90°E
60°S
9-10
PIG
PIB
ThG
West Antarctica
6-8
2
Transantarctic Mountains
1
Amundsen Sea
Ross Ice Shelf
17-18
19
16
3-5
Ross Sea
0
500
1000
1500
2000 km
180°

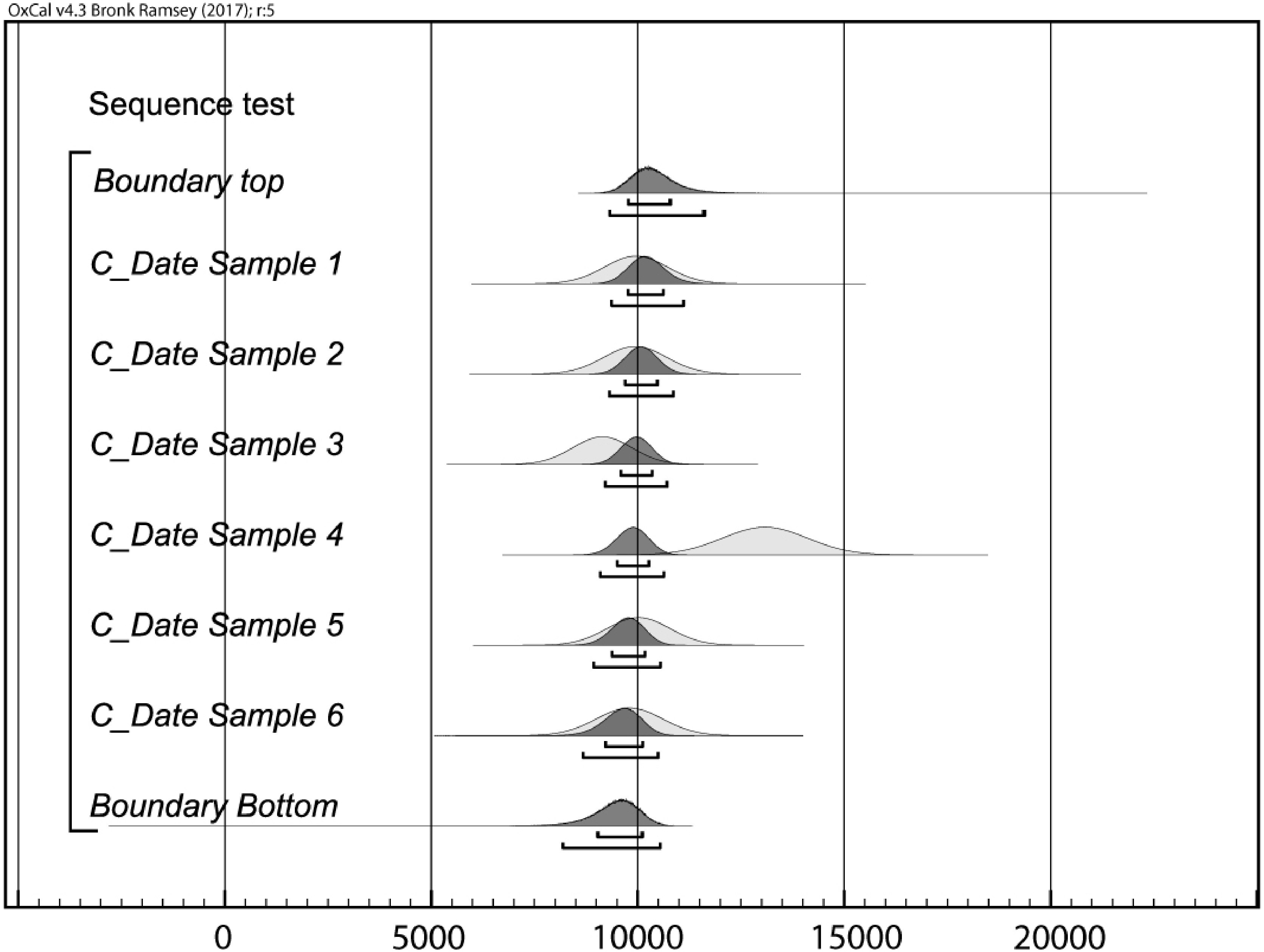

OxCal v4.3 Bronk Ramsey (2017); r:5
Sequence test
Boundary top
C_Date Sample 1
C_Date Sample 2
C_Date Sample 3
C_Date Sample 4
C_Date Sample 5
C_Date Sample 6
Boundary Bottom
0
5000
10000
15000
20000

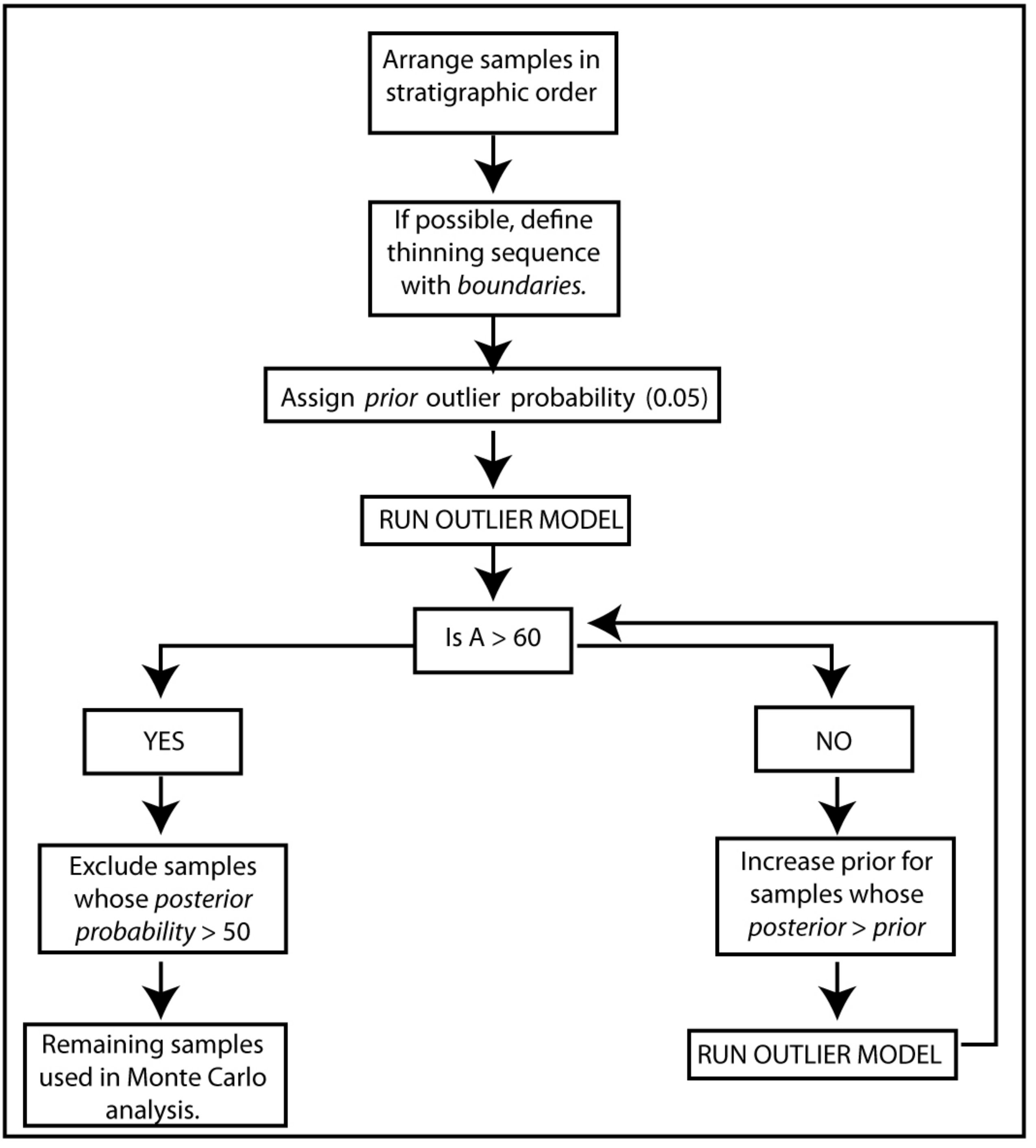
Arrange samples in stratigraphic order
If possible, define thinning sequence with *boundaries.*
Assign *prior* outlier probability (0.05)
RUN OUTLIER MODEL
Is A > 60
YES
NO
Exclude samples whose *posterior probability* > 50
Remaining samples used in Monte Carlo analysis.
Increase prior for samples whose *posterior* > *prior*
RUN OUTLIER MODEL

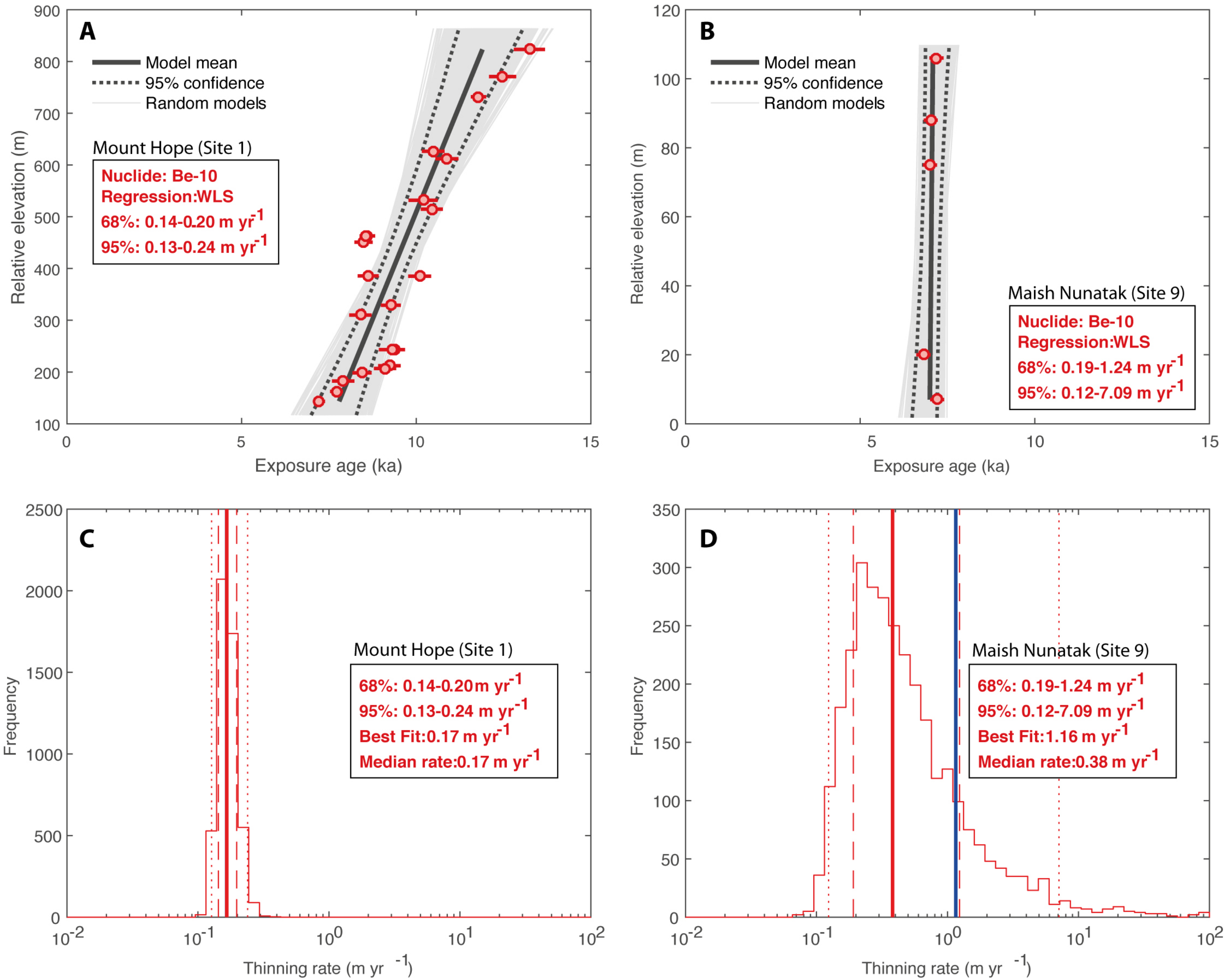
A
Model mean
95% confidence
Random models
Mount Hope (Site 1)
Nuclide: Be-10
Regression:WLS
68%: 0.14-0.20 m yr^{-1}
95%: 0.13-0.24 m yr^{-1}
Relative elevation (m)
Exposure age (ka)
B
Model mean
95% confidence
Random models
Maish Nunatak (Site 9)
Nuclide: Be-10
Regression:WLS
68%: 0.19-1.24 m yr^{-1}
95%: 0.12-7.09 m yr^{-1}
Relative elevation (m)
Exposure age (ka)
C
Mount Hope (Site 1)
68%: 0.14-0.20m yr^{-1}
95%: 0.13-0.24 m yr^{-1}
Best Fit:0.17 m yr^{-1}
Median rate:0.17 m yr^{-1}
Frequency
Thinning rate (m yr^{-1})
D
Maish Nunatak (Site 9)
68%: 0.19-1.24 m yr^{-1}
95%: 0.12-7.09 m yr^{-1}
Best Fit:1.16 m yr^{-1}
Median rate:0.38 m yr^{-1}
Frequency
Thinning rate (m yr^{-1})

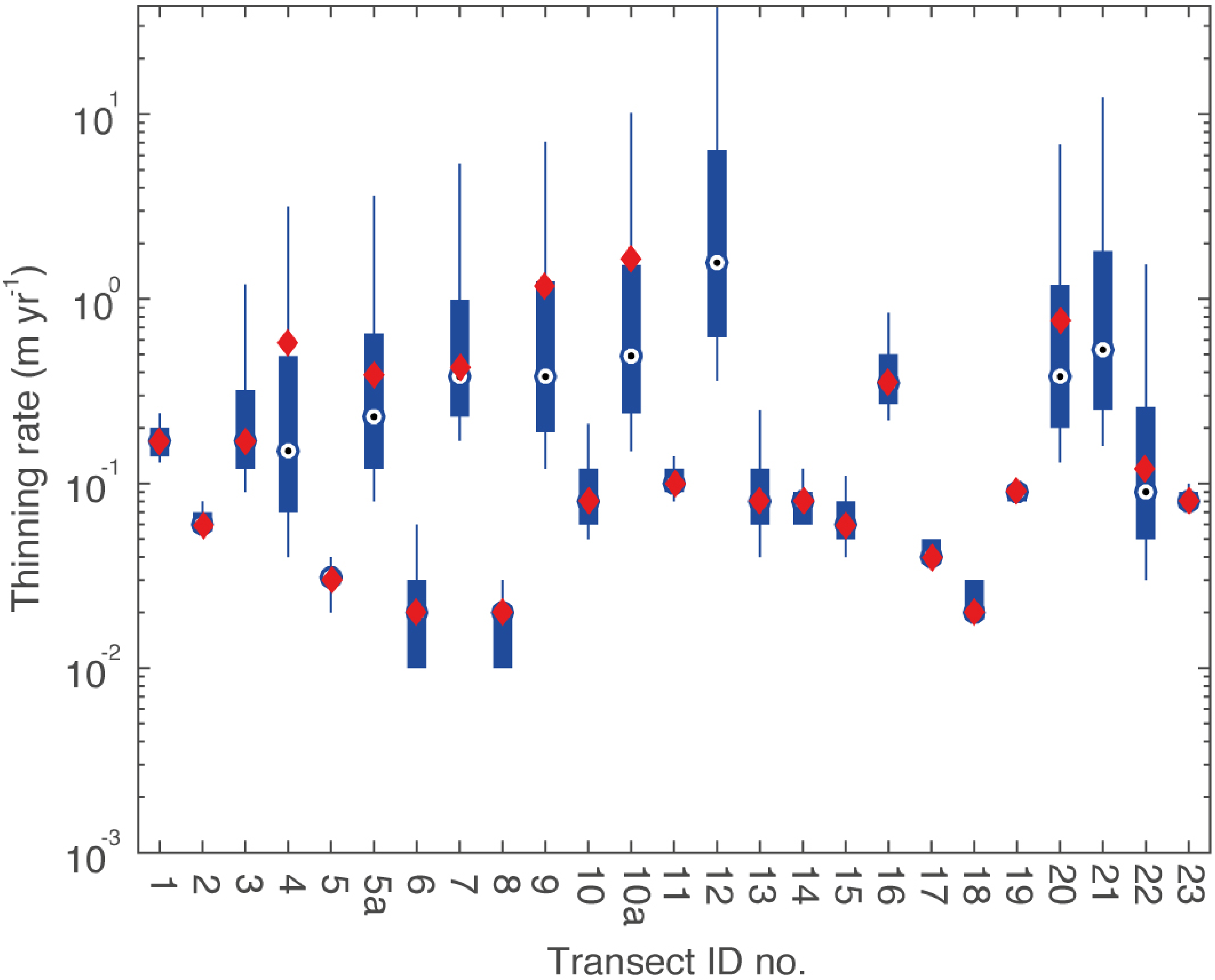

Thinning rate (m yr^{-1})
10^{1}
10^{0}
10^{-1}
10^{-2}
10^{-3}
1 2 3 4 5 5a 6 7 8 9 10 10a 11 12 13 14 15 16 17 18 19 20 21 22 23
Transect ID no.

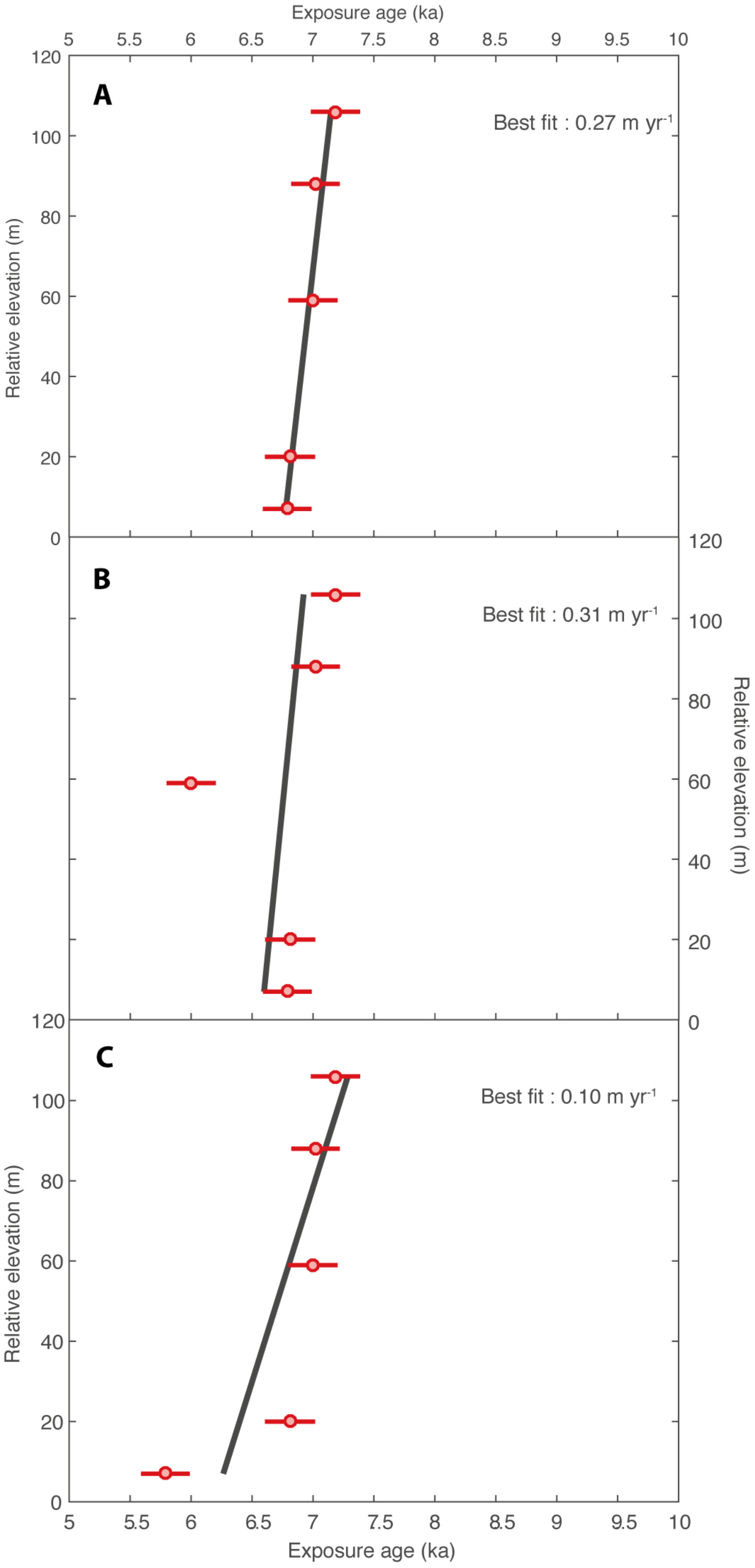
Exposure age (ka)
5
5.5
6
6.5
7
7.5
8
8.5
9
9.5
10
120
100
80
60
40
20
0
Relative elevation (m)
A
Best fit : 0.27 m yr-1
B
Best fit : 0.31 m yr-1
C
Best fit : 0.10 m yr-1

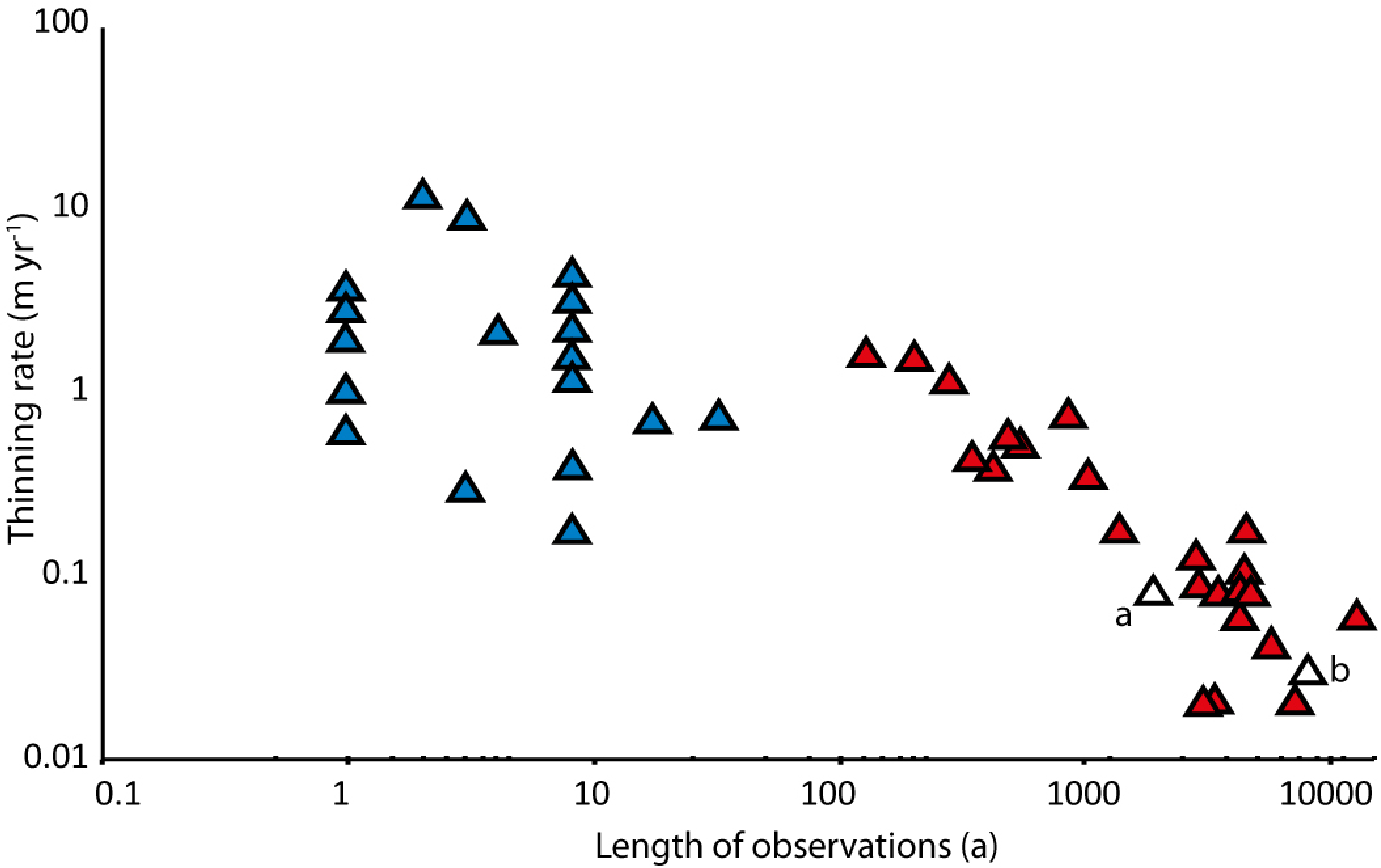

100
10
1
0.1
0.01
Thinning rate (m yr^{-1})
0.1
1
10
100
1000
10000
Length of observations (a)
a
b

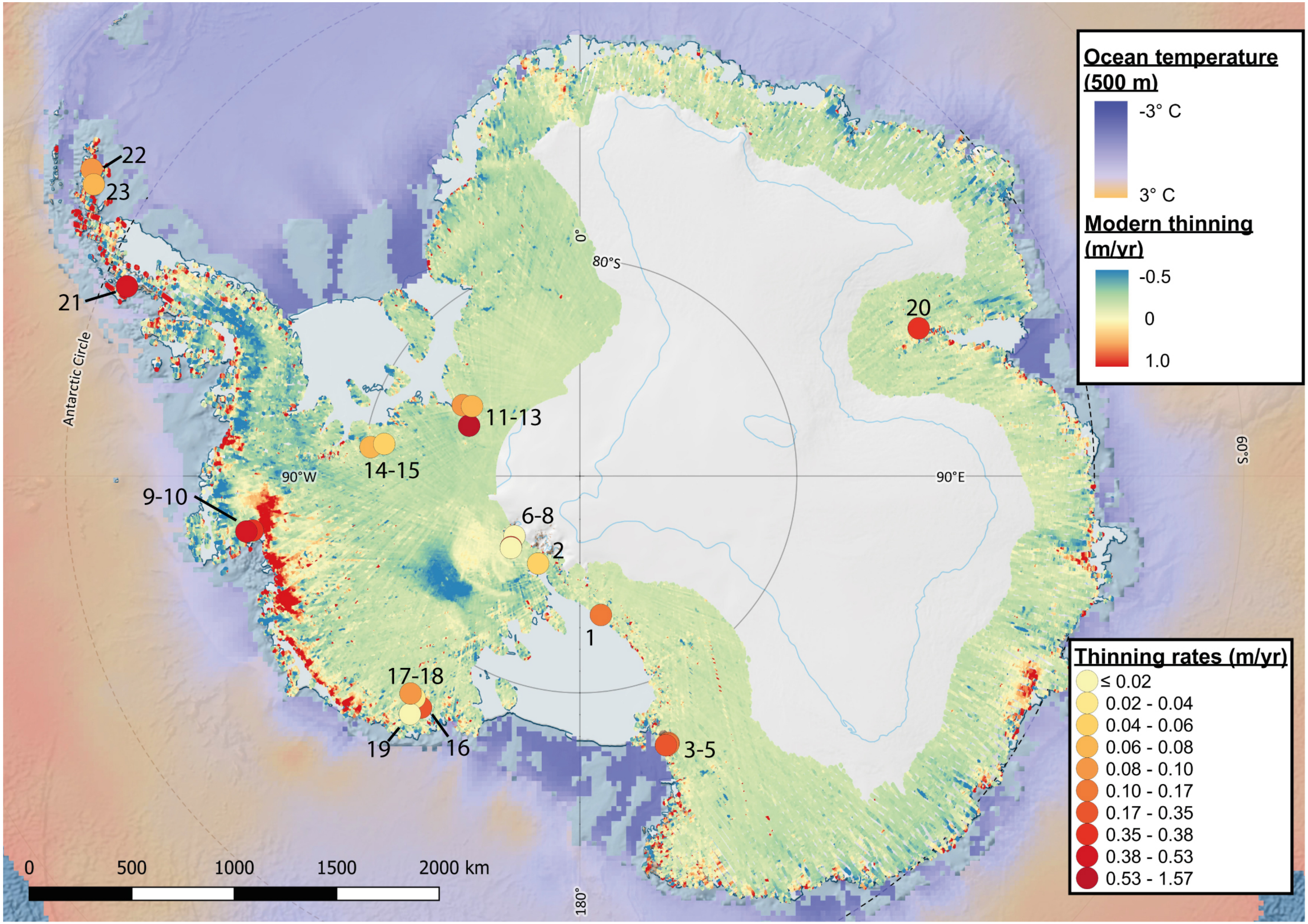

Ocean temperature (500 m)
-3° C
3° C
Modern thinning (m/yr)
-0.5
0
1.0
Thinning rates (m/yr)
≤ 0.02
0.02 - 0.04
0.04 - 0.06
0.06 - 0.08
0.08 - 0.10
0.10 - 0.17
0.17 - 0.35
0.35 - 0.38
0.38 - 0.53
0.53 - 1.57
0°
80°S
90°W
90°E
180°
60°S
Antarctic Circle
1
2
3-5
6-8
9-10
11-13
14-15
16
17-18
19
20
21
22
23
0
500
1000
1500
2000 km

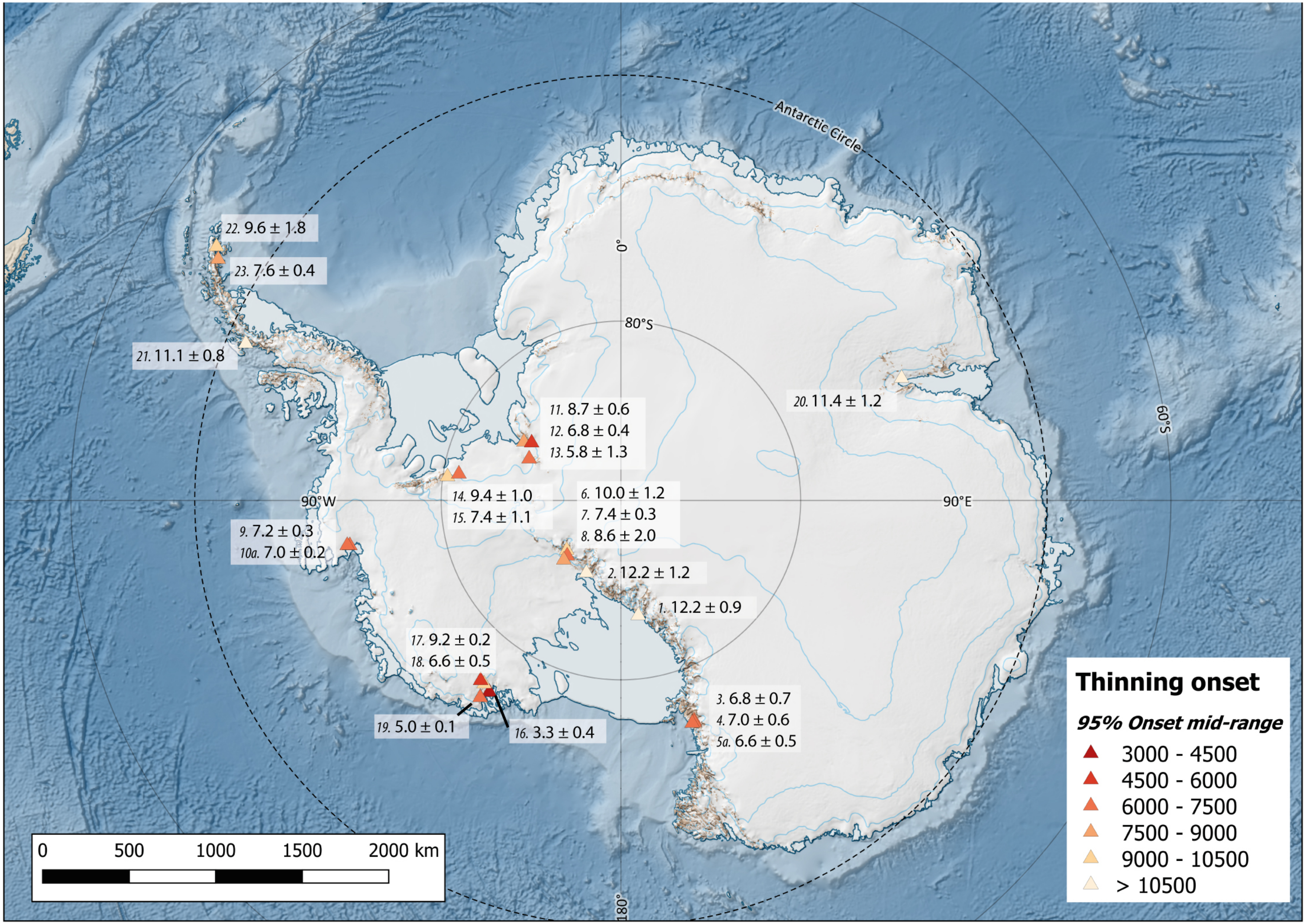

Antarctic Circle
0°
80°S
60°S
90°W
90°E
180°
22. 9.6 ± 1.8
23. 7.6 ± 0.4
21. 11.1 ± 0.8
20. 11.4 ± 1.2
11. 8.7 ± 0.6
12. 6.8 ± 0.4
13. 5.8 ± 1.3
14. 9.4 ± 1.0
15. 7.4 ± 1.1
6. 10.0 ± 1.2
7. 7.4 ± 0.3
8. 8.6 ± 2.0
9. 7.2 ± 0.3
10a. 7.0 ± 0.2
2. 12.2 ± 1.2
1. 12.2 ± 0.9
17. 9.2 ± 0.2
18. 6.6 ± 0.5
19. 5.0 ± 0.1
16. 3.3 ± 0.4
3. 6.8 ± 0.7
4. 7.0 ± 0.6
5a. 6.6 ± 0.5
0 500 1000 1500 2000 km
Thinning onset
95% Onset mid-range
3000 - 4500
4500 - 6000
6000 - 7500
7500 - 9000
9000 - 10500
> 10500

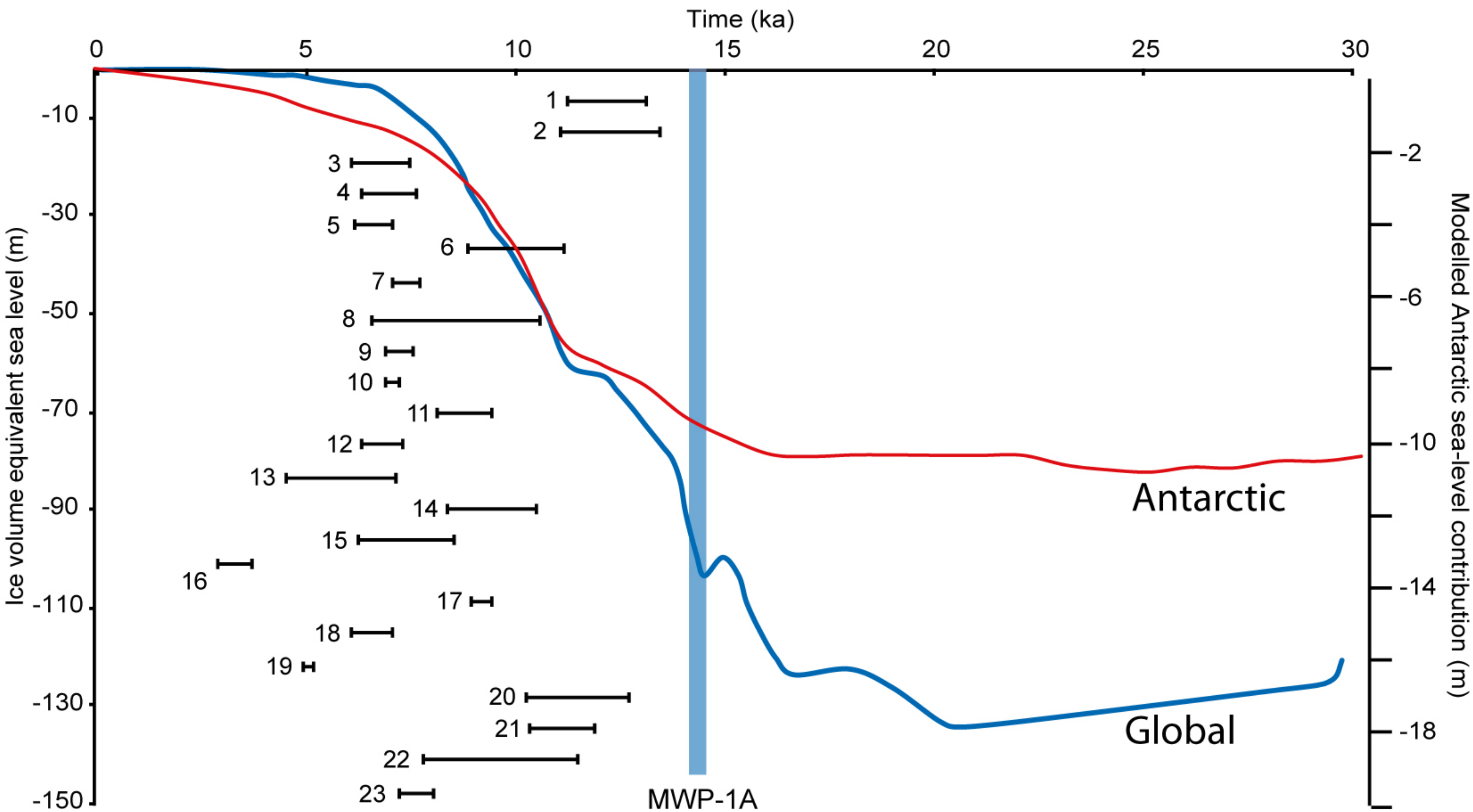

Time (ka)
0
5
10
15
20
25
30
Ice volume equivalent sea level (m)
-10
-30
-50
-70
-90
-110
-130
-150
Modelled Antarctic sea-level contribution (m)
-2
-6
-10
-14
-18
1
2
3
4
5
6
7
8
9
10
11
12
13
14
15
16
17
18
19
20
21
22
23
MWP-1A
Antarctic
Global

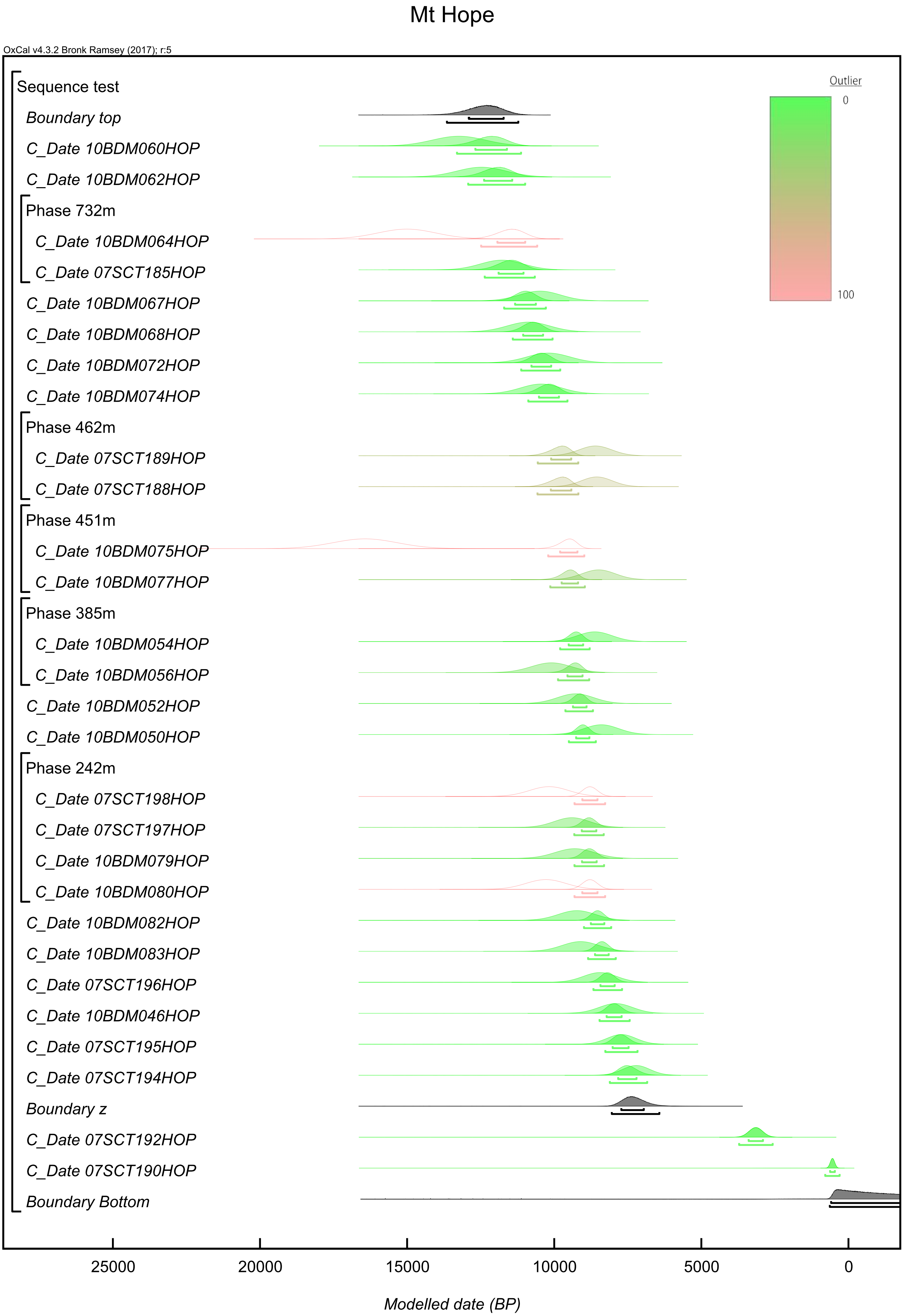
Mt Hope
OxCal v4.3.2 Bronk Ramsey (2017); r:5
Outlier
0
100
Sequence test
Boundary top
C_Date 10BDM060HOP
C_Date 10BDM062HOP
Phase 732m
C_Date 10BDM064HOP
C_Date 07SCT185HOP
C_Date 10BDM067HOP
C_Date 10BDM068HOP
C_Date 10BDM072HOP
C_Date 10BDM074HOP
Phase 462m
C_Date 07SCT189HOP
C_Date 07SCT188HOP
Phase 451m
C_Date 10BDM075HOP
C_Date 10BDM077HOP
Phase 385m
C_Date 10BDM054HOP
C_Date 10BDM056HOP
C_Date 10BDM052HOP
C_Date 10BDM050HOP
Phase 242m
C_Date 07SCT198HOP
C_Date 07SCT197HOP
C_Date 10BDM079HOP
C_Date 10BDM080HOP
C_Date 10BDM082HOP
C_Date 10BDM083HOP
C_Date 07SCT196HOP
C_Date 10BDM046HOP
C_Date 07SCT195HOP
C_Date 07SCT194HOP
Boundary z
C_Date 07SCT192HOP
C_Date 07SCT190HOP
Boundary Bottom
25000
20000
15000
10000
5000
0
Modelled date (BP)

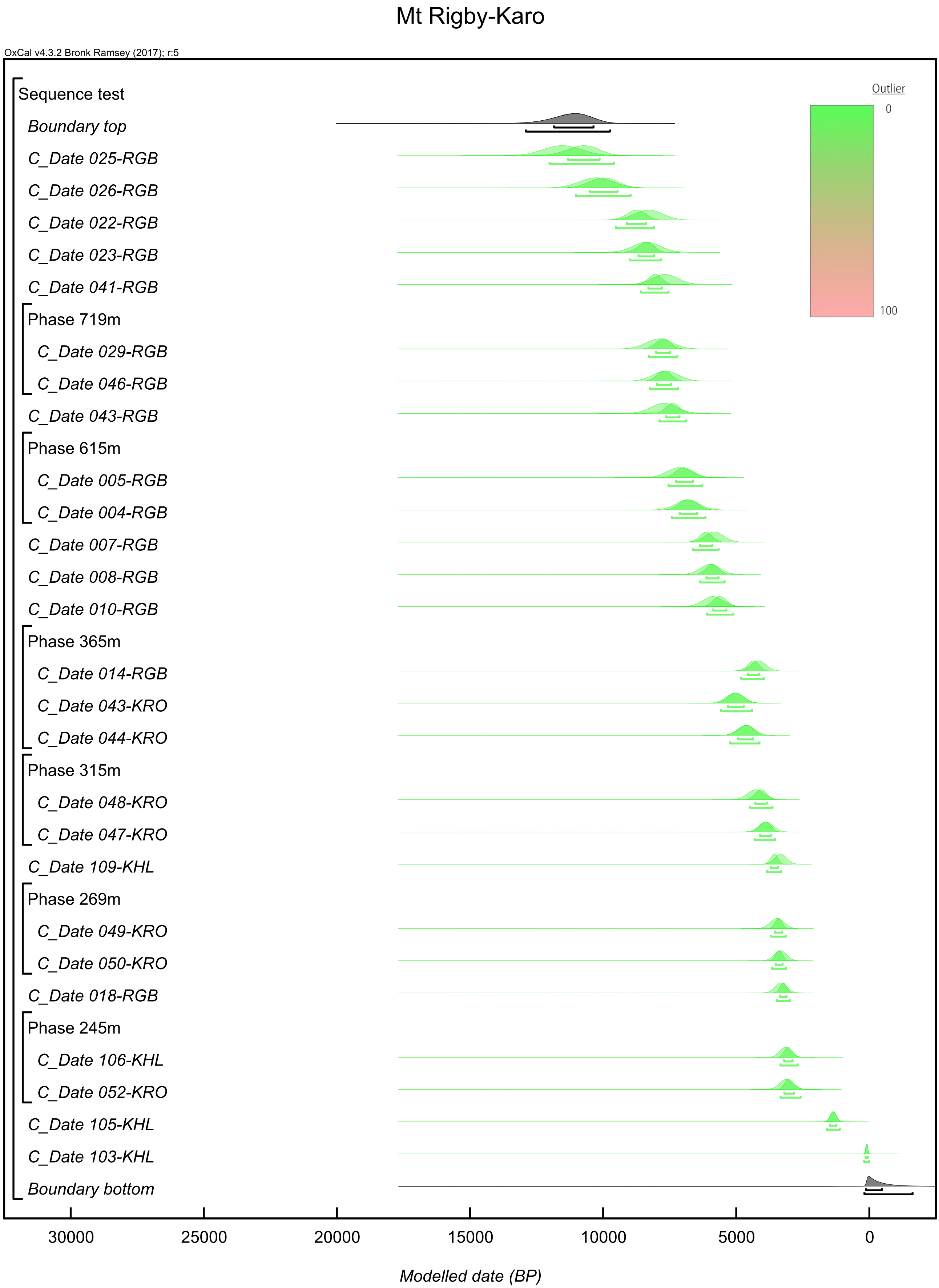

Mt Rigby-Karo
OxCal v4.3.2 Bronk Ramsey (2017); r:5
Sequence test
Boundary top
C_Date 025-RGB
C_Date 026-RGB
C_Date 022-RGB
C_Date 023-RGB
C_Date 041-RGB
Phase 719m
C_Date 029-RGB
C_Date 046-RGB
C_Date 043-RGB
Phase 615m
C_Date 005-RGB
C_Date 004-RGB
C_Date 007-RGB
C_Date 008-RGB
C_Date 010-RGB
Phase 365m
C_Date 014-RGB
C_Date 043-KRO
C_Date 044-KRO
Phase 315m
C_Date 048-KRO
C_Date 047-KRO
C_Date 109-KHL
Phase 269m
C_Date 049-KRO
C_Date 050-KRO
C_Date 018-RGB
Phase 245m
C_Date 106-KHL
C_Date 052-KRO
C_Date 105-KHL
C_Date 103-KHL
Boundary bottom
Outlier
0
100
30000
25000
20000
15000
10000
5000
0
Modelled date (BP)

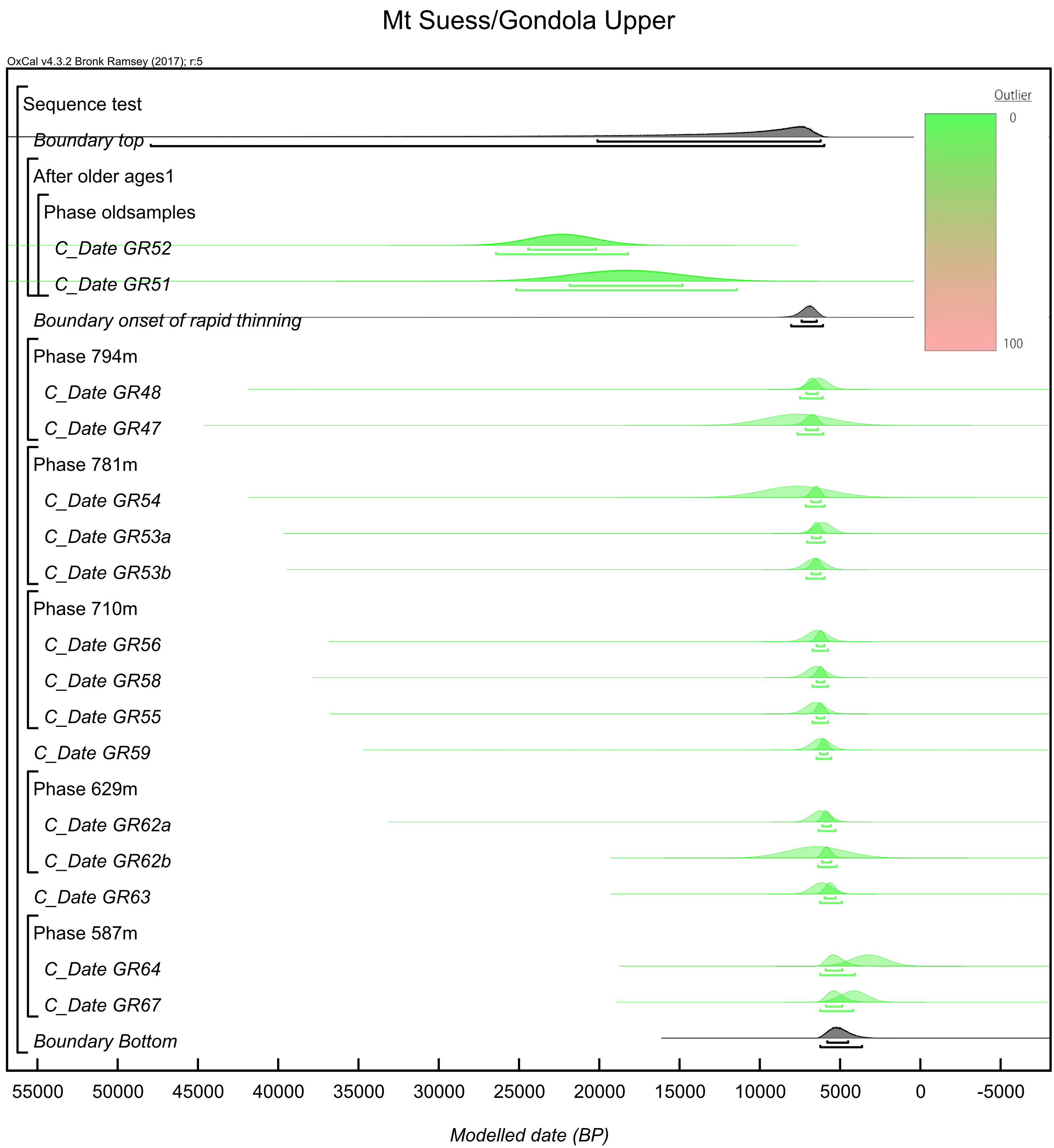

Mt Suess/Gondola Upper
OxCal v4.3.2 Bronk Ramsey (2017); r:5
Outlier
0
100
Sequence test
Boundary top
After older ages1
Phase oldsamples
C_Date GR52
C_Date GR51
Boundary onset of rapid thinning
Phase 794m
C_Date GR48
C_Date GR47
Phase 781m
C_Date GR54
C_Date GR53a
C_Date GR53b
Phase 710m
C_Date GR56
C_Date GR58
C_Date GR55
C_Date GR59
Phase 629m
C_Date GR62a
C_Date GR62b
C_Date GR63
Phase 587m
C_Date GR64
C_Date GR67
Boundary Bottom
55000
50000
45000
40000
35000
30000
25000
20000
15000
10000
5000
0
-5000
Modelled date (BP)

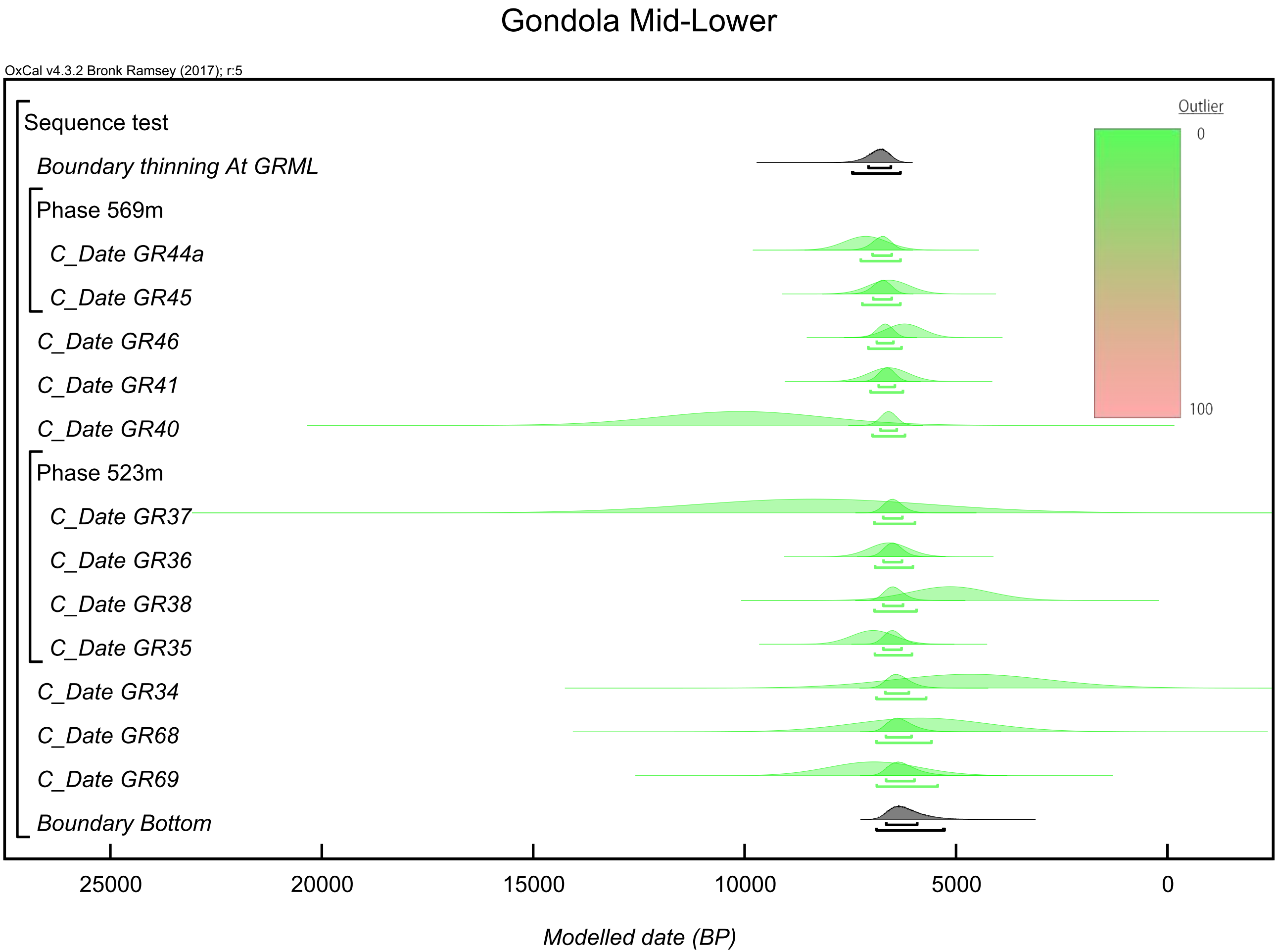

Gondola Mid-Lower
OxCal v4.3.2 Bronk Ramsey (2017); r:5
Sequence test
Boundary thinning At GRML
Phase 569m
C_Date GR44a
C_Date GR45
C_Date GR46
C_Date GR41
C_Date GR40
Phase 523m
C_Date GR37
C_Date GR36
C_Date GR38
C_Date GR35
C_Date GR34
C_Date GR68
C_Date GR69
Boundary Bottom
Outlier
0
100
25000
20000
15000
10000
5000
0
Modelled date (BP)

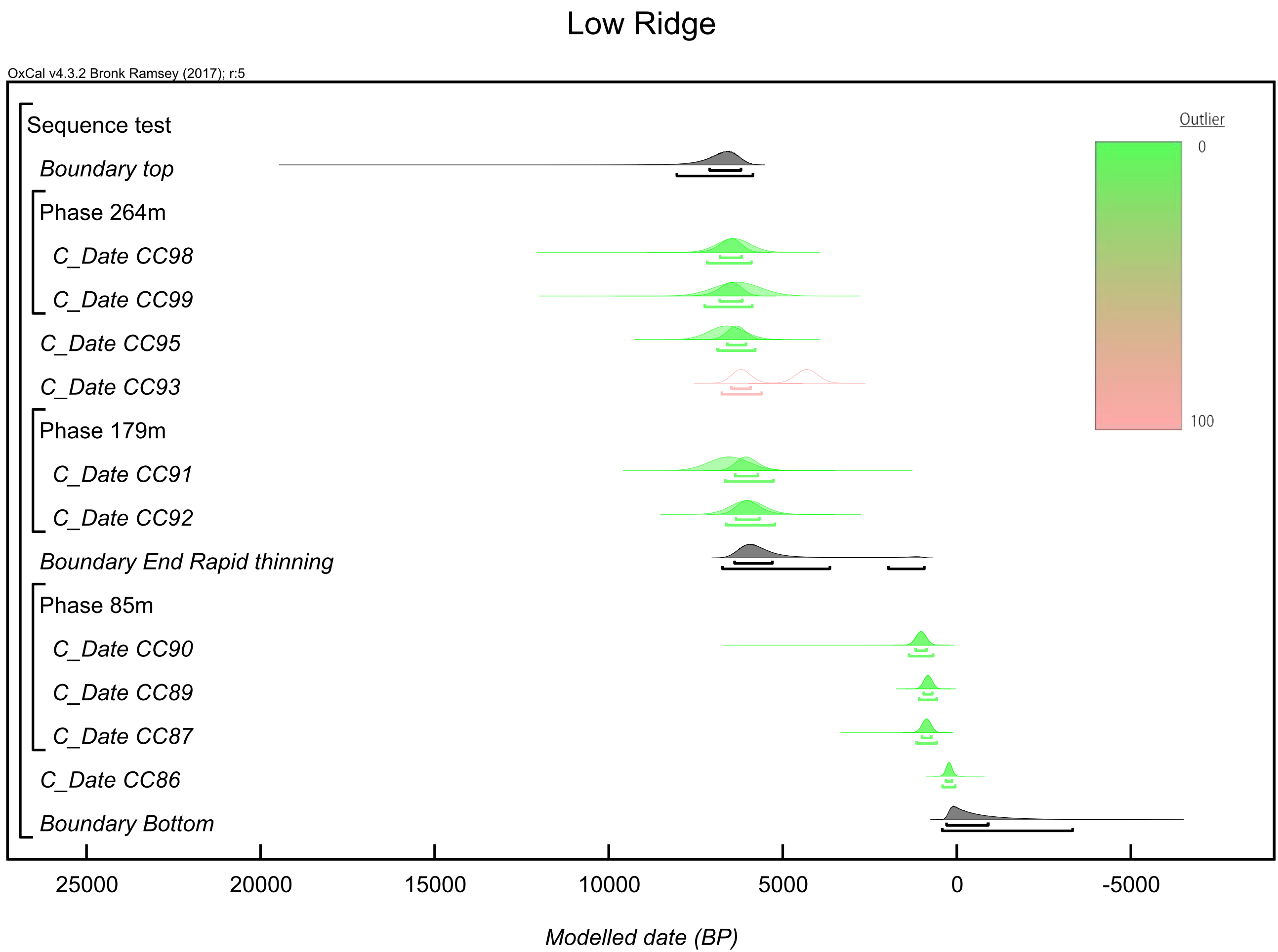

Low Ridge
OxCal v4.3.2 Bronk Ramsey (2017); r:5
Sequence test
Boundary top
Phase 264m
C_Date CC98
C_Date CC99
C_Date CC95
C_Date CC93
Phase 179m
C_Date CC91
C_Date CC92
Boundary End Rapid thinning
Phase 85m
C_Date CC90
C_Date CC89
C_Date CC87
C_Date CC86
Boundary Bottom
Outlier
0
100
25000
20000
15000
10000
5000
0
-5000
Modelled date (BP)

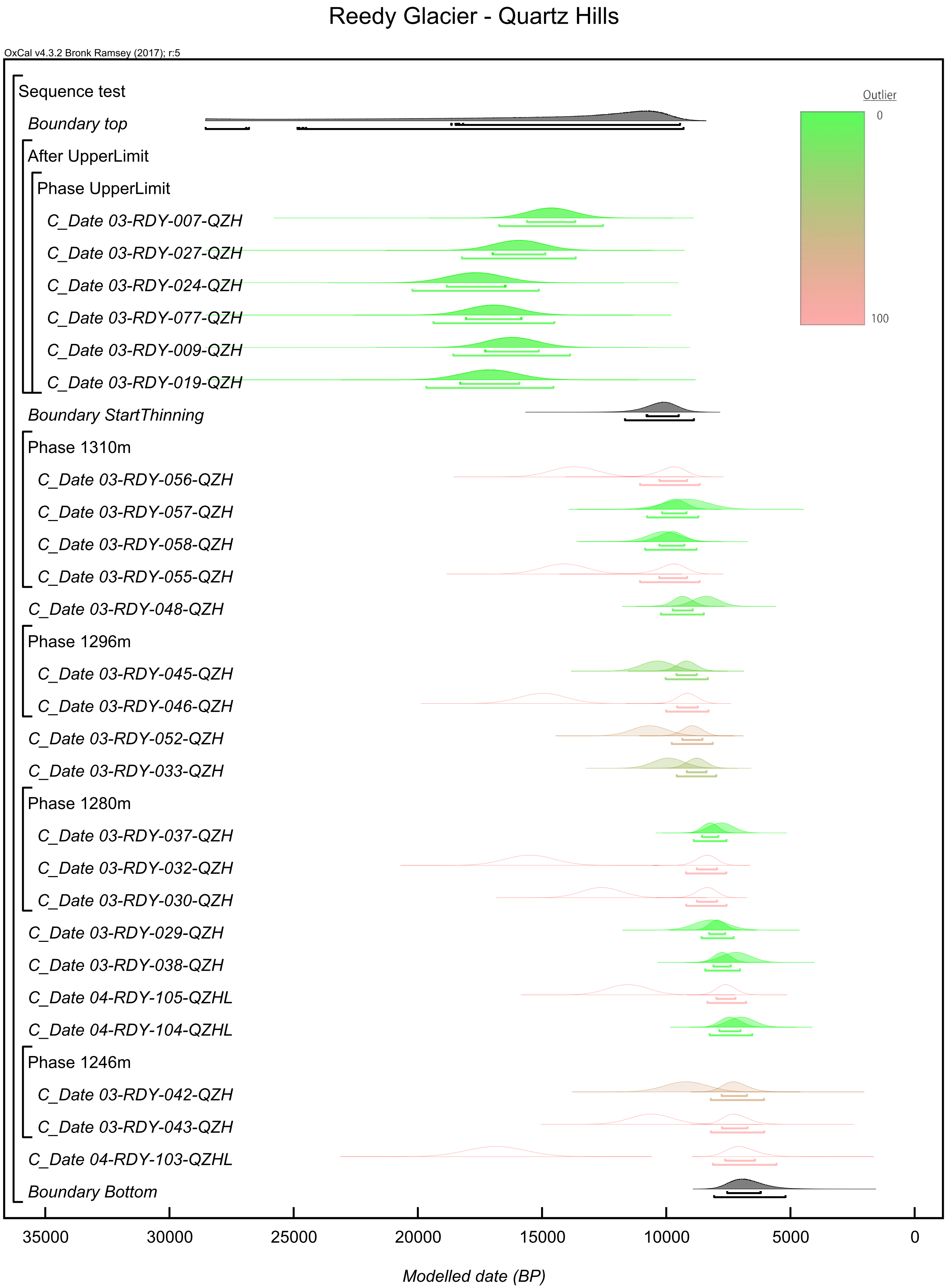
Reedy Glacier - Quartz Hills
OxCal v4.3.2 Bronk Ramsey (2017); r:5
Sequence test
Boundary top
After UpperLimit
Phase UpperLimit
C_Date 03-RDY-007-QZH
C_Date 03-RDY-027-QZH
C_Date 03-RDY-024-QZH
C_Date 03-RDY-077-QZH
C_Date 03-RDY-009-QZH
C_Date 03-RDY-019-QZH
Boundary StartThinning
Phase 1310m
C_Date 03-RDY-056-QZH
C_Date 03-RDY-057-QZH
C_Date 03-RDY-058-QZH
C_Date 03-RDY-055-QZH
C_Date 03-RDY-048-QZH
Phase 1296m
C_Date 03-RDY-045-QZH
C_Date 03-RDY-046-QZH
C_Date 03-RDY-052-QZH
C_Date 03-RDY-033-QZH
Phase 1280m
C_Date 03-RDY-037-QZH
C_Date 03-RDY-032-QZH
C_Date 03-RDY-030-QZH
C_Date 03-RDY-029-QZH
C_Date 03-RDY-038-QZH
C_Date 04-RDY-105-QZHL
C_Date 04-RDY-104-QZHL
Phase 1246m
C_Date 03-RDY-042-QZH
C_Date 03-RDY-043-QZH
C_Date 04-RDY-103-QZHL
Boundary Bottom
Outlier
0
100
35000
30000
25000
20000
15000
10000
5000
0
Modelled date (BP)

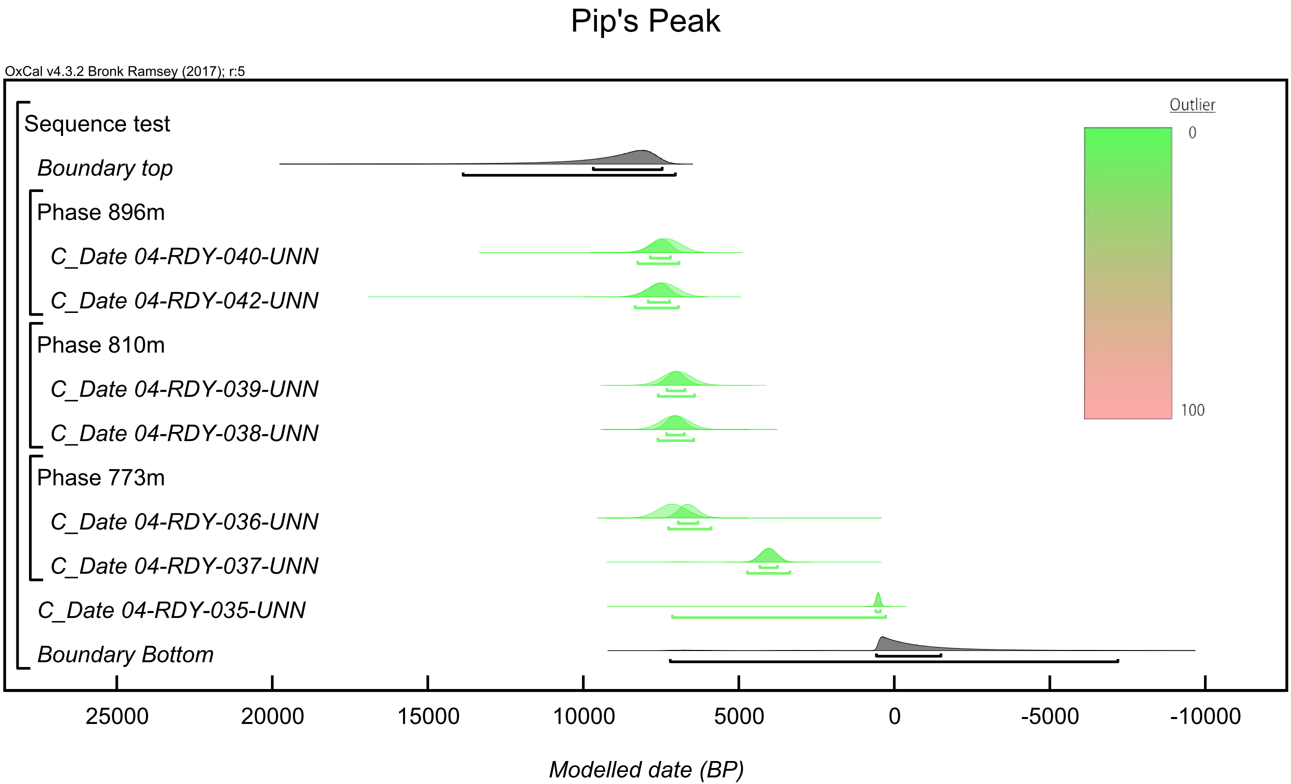

Pip's Peak
OxCal v4.3.2 Bronk Ramsey (2017); r:5
Outlier
0
100
Sequence test
Boundary top
Phase 896m
C_Date 04-RDY-040-UNN
C_Date 04-RDY-042-UNN
Phase 810m
C_Date 04-RDY-039-UNN
C_Date 04-RDY-038-UNN
Phase 773m
C_Date 04-RDY-036-UNN
C_Date 04-RDY-037-UNN
C_Date 04-RDY-035-UNN
Boundary Bottom
25000
20000
15000
10000
5000
0
-5000
-10000
Modelled date (BP)

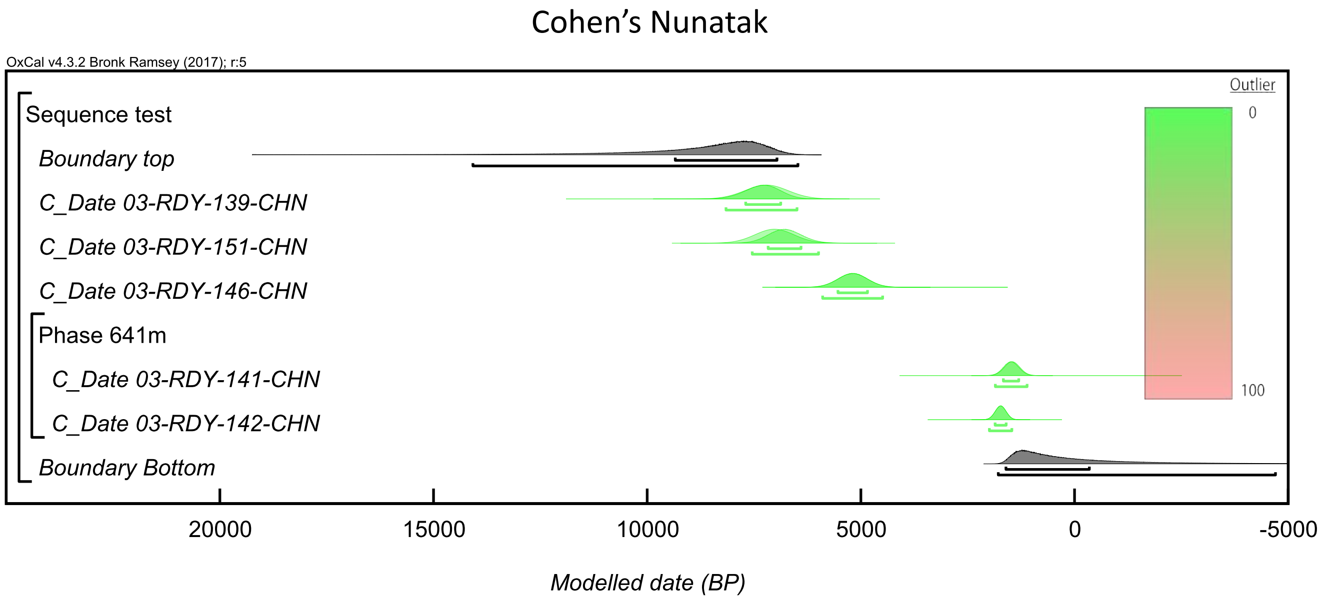

Cohen’s Nunatak
OxCal v4.3.2 Bronk Ramsey (2017); r:5
Outlier
0
100
Sequence test
Boundary top
C_Date 03-RDY-139-CHN
C_Date 03-RDY-151-CHN
C_Date 03-RDY-146-CHN
Phase 641m
C_Date 03-RDY-141-CHN
C_Date 03-RDY-142-CHN
Boundary Bottom
20000
15000
10000
5000
0
-5000
Modelled date (BP)

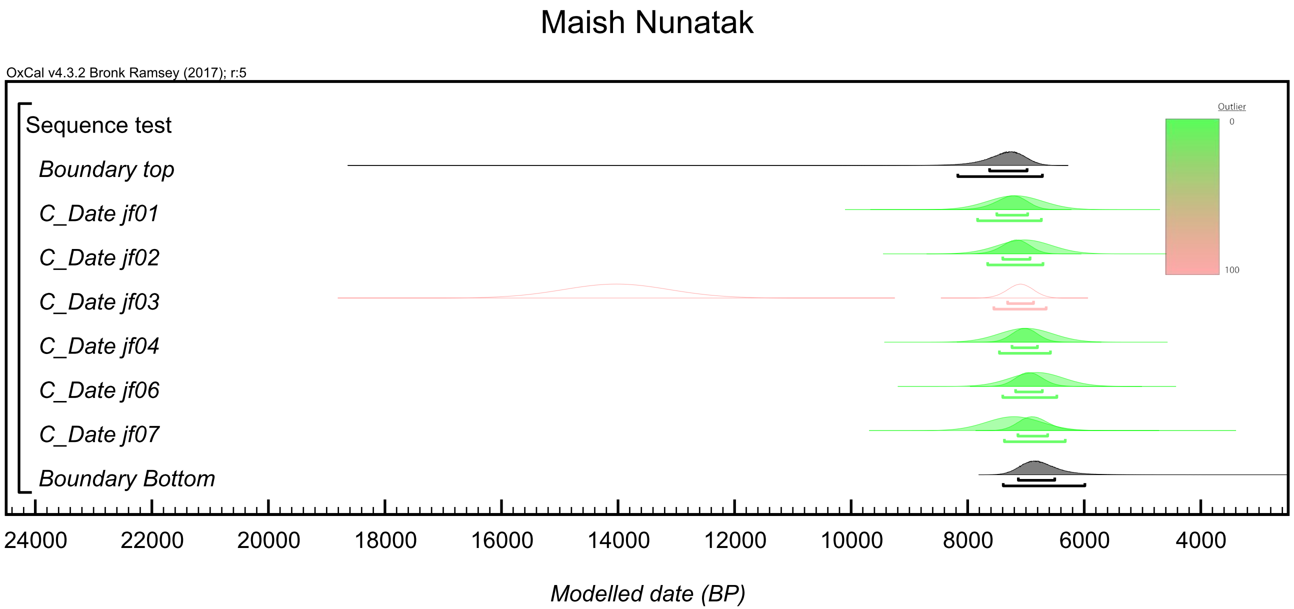
Maish Nunatak
OxCal v4.3.2 Bronk Ramsey (2017); r:5
Sequence test
Boundary top
C_Date jf01
C_Date jf02
C_Date jf03
C_Date jf04
C_Date jf06
C_Date jf07
Boundary Bottom
Outlier
0
100
24000
22000
20000
18000
16000
14000
12000
10000
8000
6000
4000
Modelled date (BP)

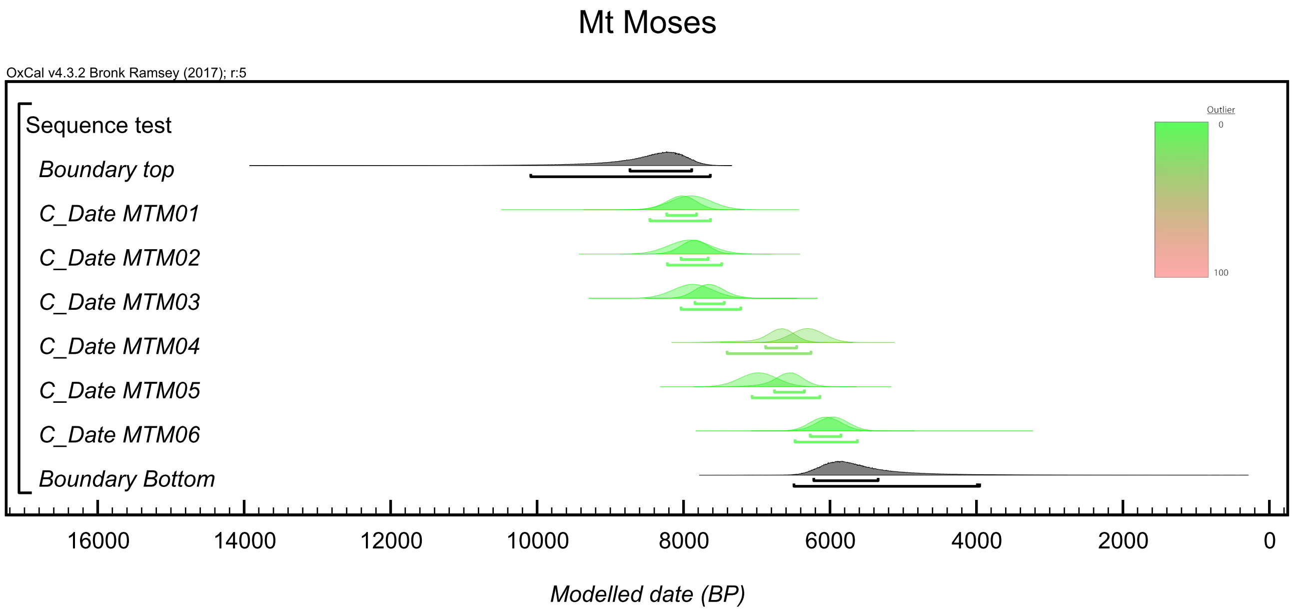
Mt Moses
OxCal v4.3.2 Bronk Ramsey (2017); r:5
Sequence test
Boundary top
C_Date MTM01
C_Date MTM02
C_Date MTM03
C_Date MTM04
C_Date MTM05
C_Date MTM06
Boundary Bottom
Outlier
0
100
16000
14000
12000
10000
8000
6000
4000
2000
0
Modelled date (BP)

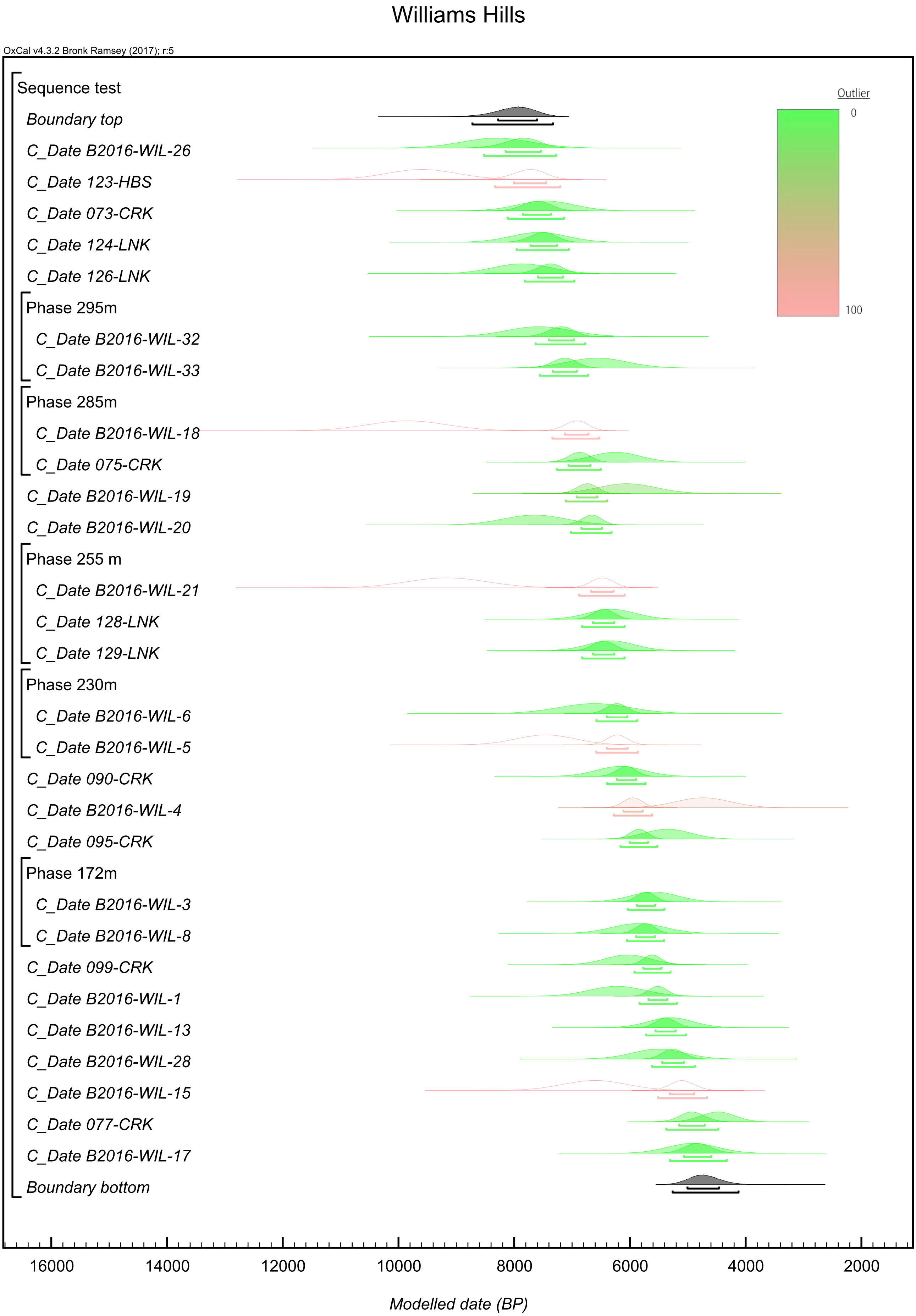

Williams Hills
OxCal v4.3.2 Bronk Ramsey (2017); r:5
Sequence test
Boundary top
C_Date B2016-WIL-26
C_Date 123-HBS
C_Date 073-CRK
C_Date 124-LNK
C_Date 126-LNK
Phase 295m
C_Date B2016-WIL-32
C_Date B2016-WIL-33
Phase 285m
C_Date B2016-WIL-18
C_Date 075-CRK
C_Date B2016-WIL-19
C_Date B2016-WIL-20
Phase 255 m
C_Date B2016-WIL-21
C_Date 128-LNK
C_Date 129-LNK
Phase 230m
C_Date B2016-WIL-6
C_Date B2016-WIL-5
C_Date 090-CRK
C_Date B2016-WIL-4
C_Date 095-CRK
Phase 172m
C_Date B2016-WIL-3
C_Date B2016-WIL-8
C_Date 099-CRK
C_Date B2016-WIL-1
C_Date B2016-WIL-13
C_Date B2016-WIL-28
C_Date B2016-WIL-15
C_Date 077-CRK
C_Date B2016-WIL-17
Boundary bottom
Outlier
0
100
16000
14000
12000
10000
8000
6000
4000
2000
Modelled date (BP)

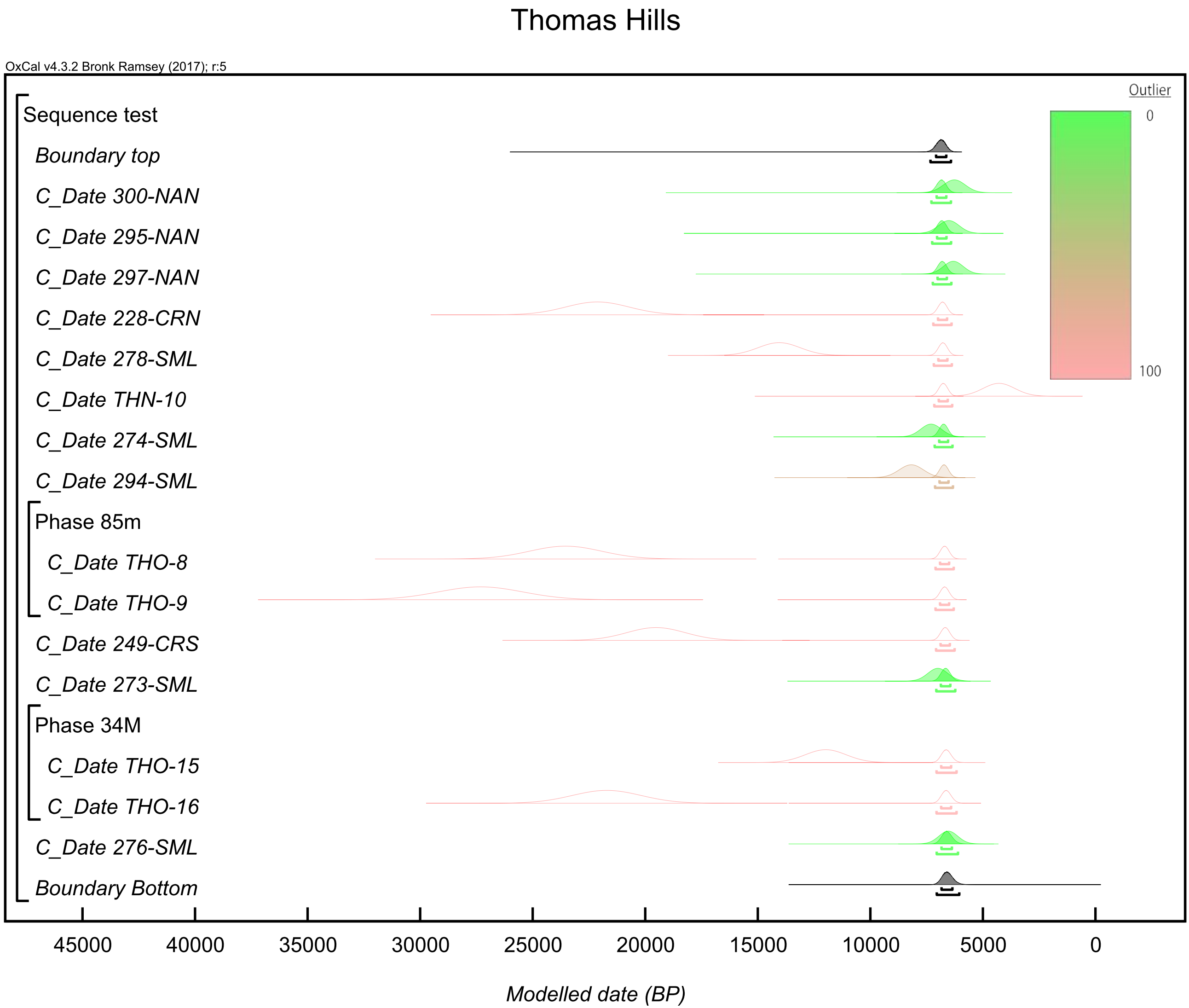

Thomas Hills
OxCal v4.3.2 Bronk Ramsey (2017); r:5
Outlier
0
100
Sequence test
Boundary top
C_Date 300-NAN
C_Date 295-NAN
C_Date 297-NAN
C_Date 228-CRN
C_Date 278-SML
C_Date THN-10
C_Date 274-SML
C_Date 294-SML
Phase 85m
C_Date THO-8
C_Date THO-9
C_Date 249-CRS
C_Date 273-SML
Phase 34M
C_Date THO-15
C_Date THO-16
C_Date 276-SML
Boundary Bottom
45000
40000
35000
30000
25000
20000
15000
10000
5000
0
Modelled date (BP)

Mt Harper-Bragg

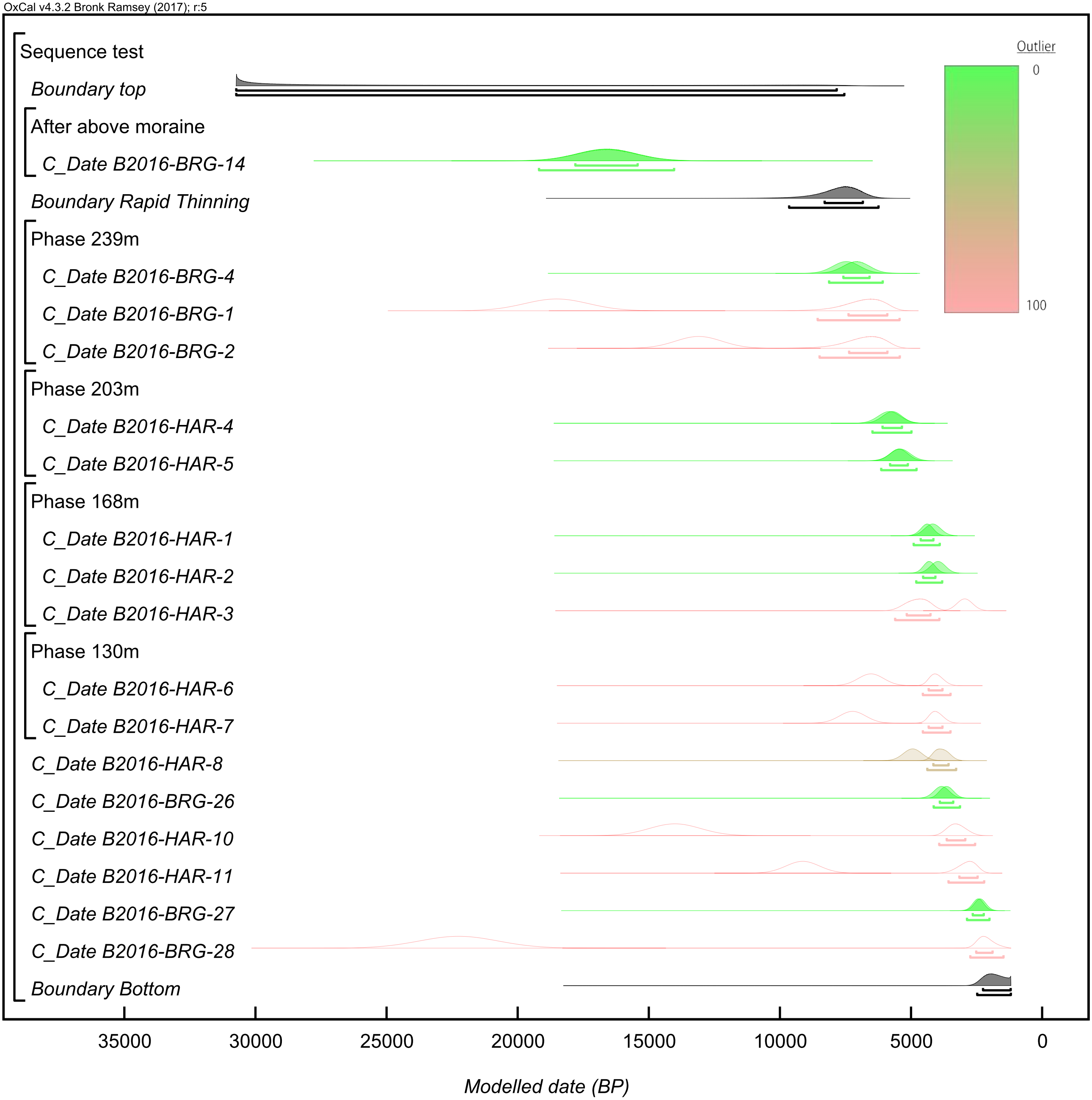

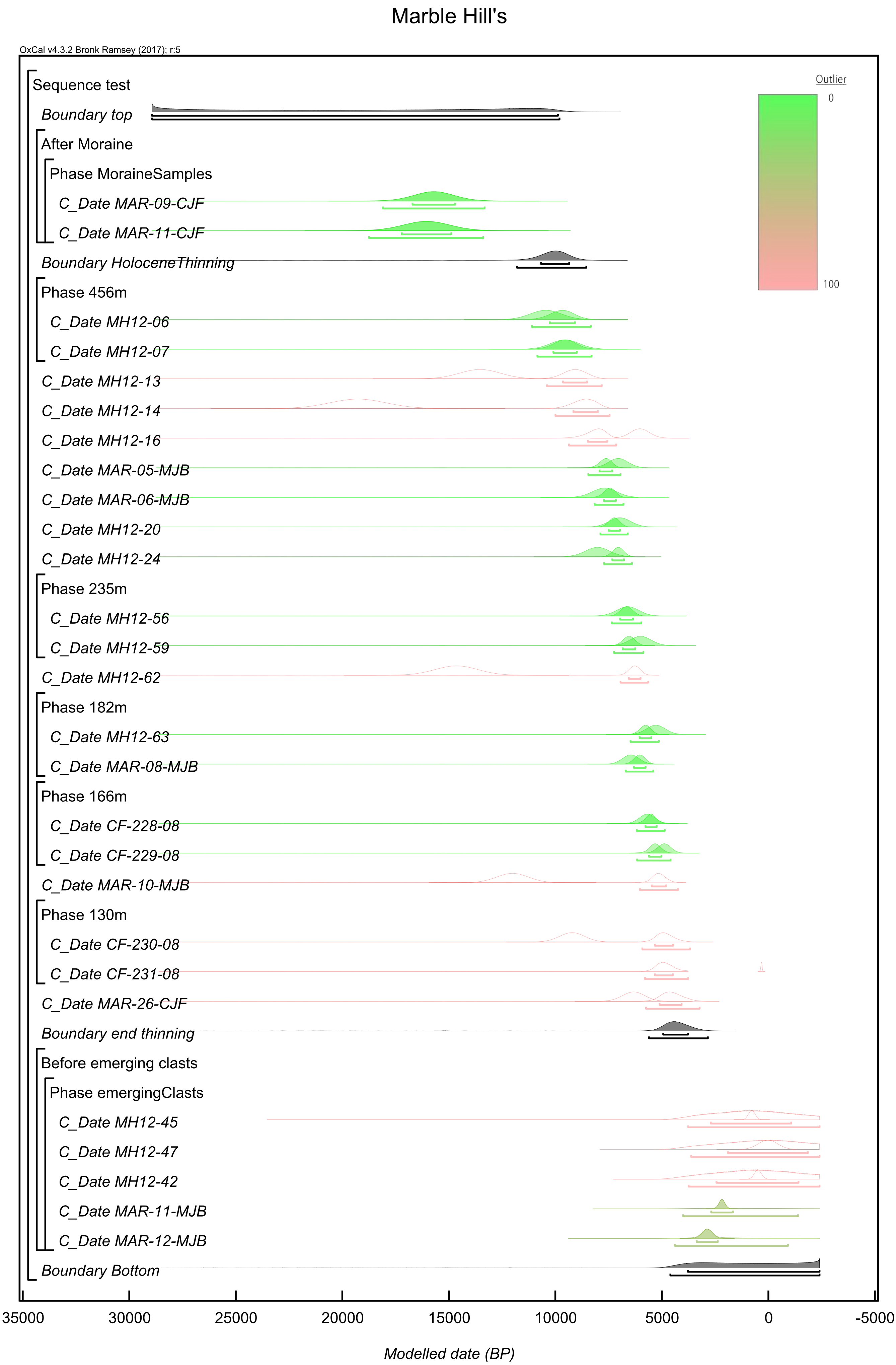
Marble Hill's
OxCal v4.3.2 Bronk Ramsey (2017); r:5
Outlier
0
100
Sequence test
Boundary top
After Moraine
Phase MoraineSamples
C_Date MAR-09-CJF
C_Date MAR-11-CJF
Boundary HoloceneThinning
Phase 456m
C_Date MH12-06
C_Date MH12-07
C_Date MH12-13
C_Date MH12-14
C_Date MH12-16
C_Date MAR-05-MJB
C_Date MAR-06-MJB
C_Date MH12-20
C_Date MH12-24
Phase 235m
C_Date MH12-56
C_Date MH12-59
C_Date MH12-62
Phase 182m
C_Date MH12-63
C_Date MAR-08-MJB
Phase 166m
C_Date CF-228-08
C_Date CF-229-08
C_Date MAR-10-MJB
Phase 130m
C_Date CF-230-08
C_Date CF-231-08
C_Date MAR-26-CJF
Boundary end thinning
Before emerging clasts
Phase emergingClasts
C_Date MH12-45
C_Date MH12-47
C_Date MH12-42
C_Date MAR-11-MJB
C_Date MAR-12-MJB
Boundary Bottom
35000
30000
25000
20000
15000
10000
5000
0
-5000
Modelled date (BP)

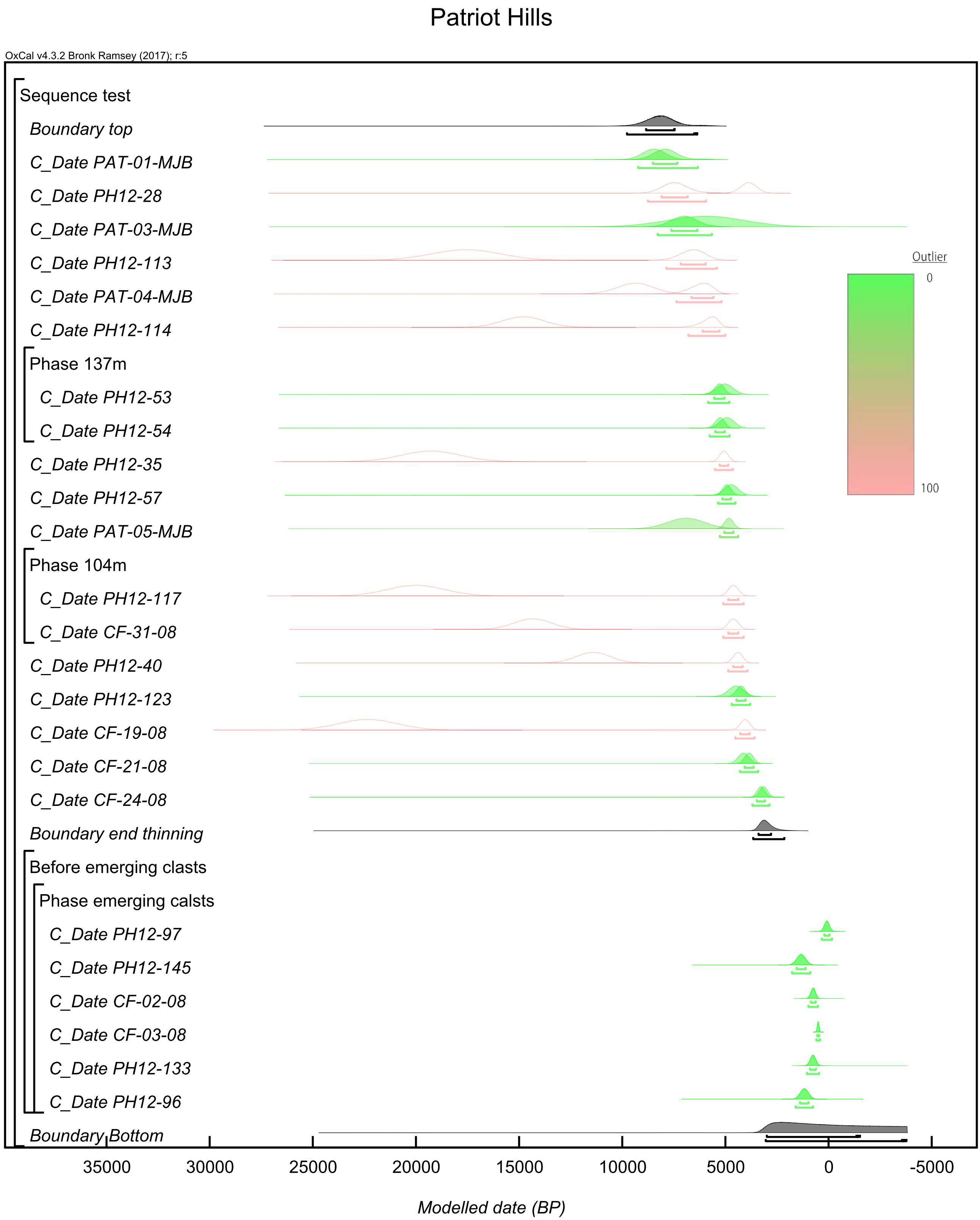

Patriot Hills
OxCal v4.3.2 Bronk Ramsey (2017); r:5
Sequence test
Boundary top
C_Date PAT-01-MJB
C_Date PH12-28
C_Date PAT-03-MJB
C_Date PH12-113
C_Date PAT-04-MJB
C_Date PH12-114
Phase 137m
C_Date PH12-53
C_Date PH12-54
C_Date PH12-35
C_Date PH12-57
C_Date PAT-05-MJB
Phase 104m
C_Date PH12-117
C_Date CF-31-08
C_Date PH12-40
C_Date PH12-123
C_Date CF-19-08
C_Date CF-21-08
C_Date CF-24-08
Boundary end thinning
Before emerging clasts
Phase emerging calsts
C_Date PH12-97
C_Date PH12-145
C_Date CF-02-08
C_Date CF-03-08
C_Date PH12-133
C_Date PH12-96
Boundary Bottom
Outlier
0
100
35000
30000
25000
20000
15000
10000
5000
0
-5000
Modelled date (BP)

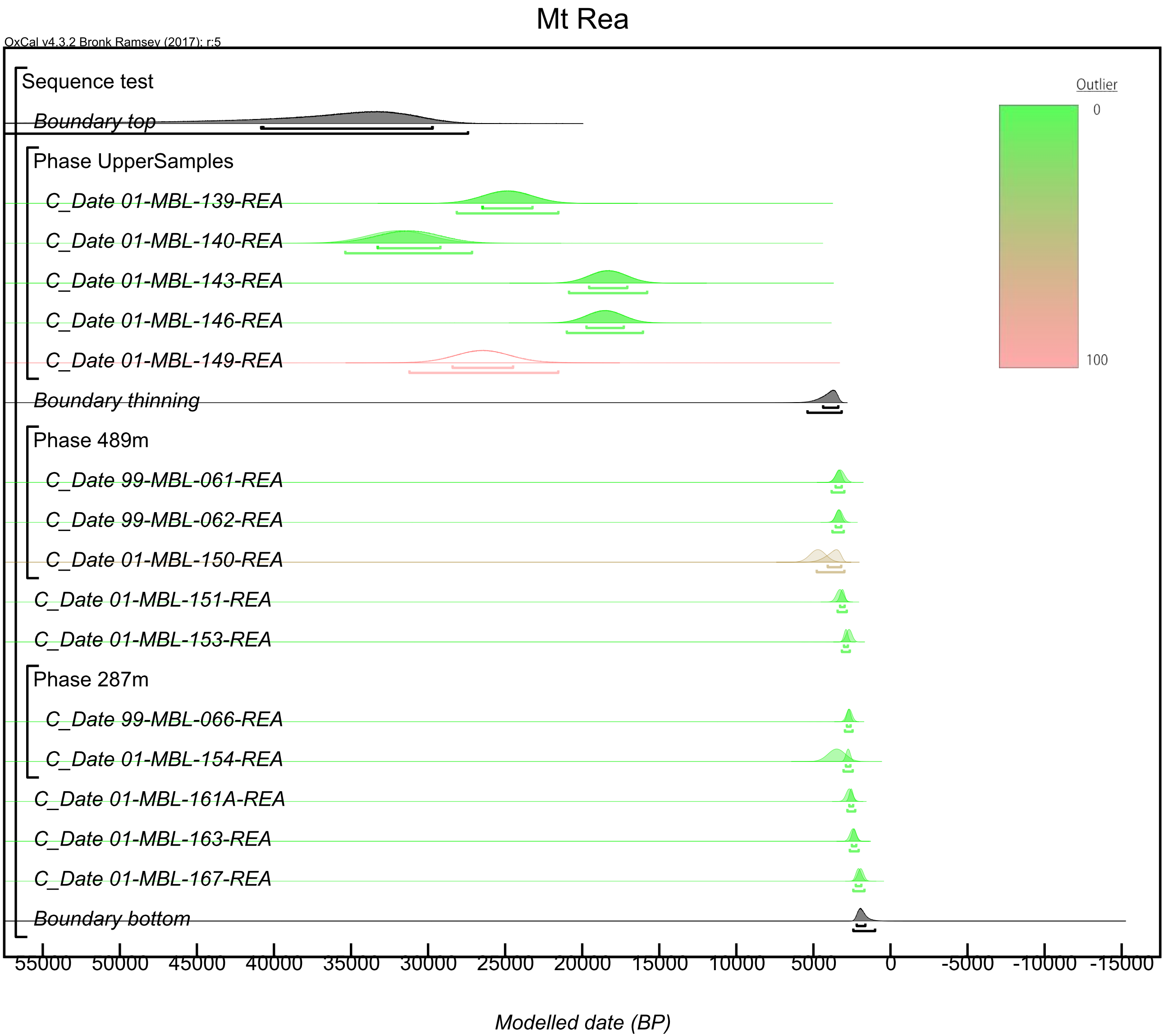

Mt Rea
OxCal v4.3.2 Bronk Ramsey (2017); r:5
Sequence test
Boundary top
Phase UpperSamples
C_Date 01-MBL-139-REA
C_Date 01-MBL-140-REA
C_Date 01-MBL-143-REA
C_Date 01-MBL-146-REA
C_Date 01-MBL-149-REA
Boundary thinning
Phase 489m
C_Date 99-MBL-061-REA
C_Date 99-MBL-062-REA
C_Date 01-MBL-150-REA
C_Date 01-MBL-151-REA
C_Date 01-MBL-153-REA
Phase 287m
C_Date 99-MBL-066-REA
C_Date 01-MBL-154-REA
C_Date 01-MBL-161A-REA
C_Date 01-MBL-163-REA
C_Date 01-MBL-167-REA
Boundary bottom
Outlier
0
100
55000 50000 45000 40000 35000 30000 25000 20000 15000 10000 5000 0 -5000 -10000 -15000
Modelled date (BP)

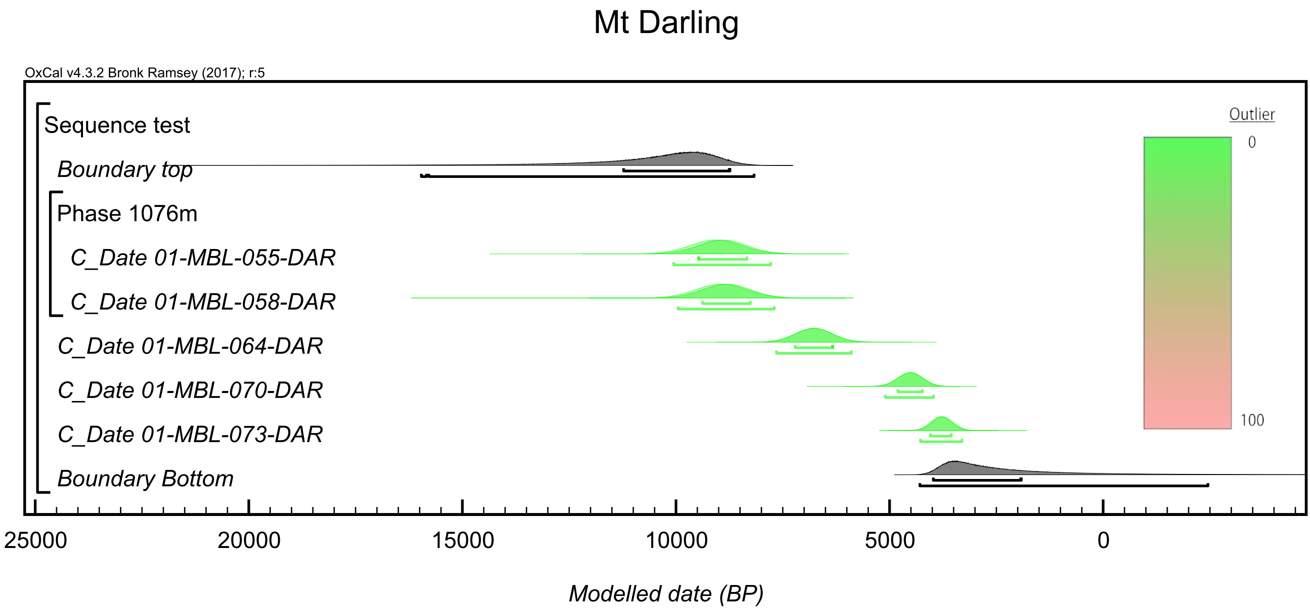
Mt Darling
OxCal v4.3.2 Bronk Ramsey (2017); r:5
Sequence test
Boundary top
Phase 1076m
C_Date 01-MBL-055-DAR
C_Date 01-MBL-058-DAR
C_Date 01-MBL-064-DAR
C_Date 01-MBL-070-DAR
C_Date 01-MBL-073-DAR
Boundary Bottom
Outlier
0
100
25000
20000
15000
10000
5000
0
Modelled date (BP)

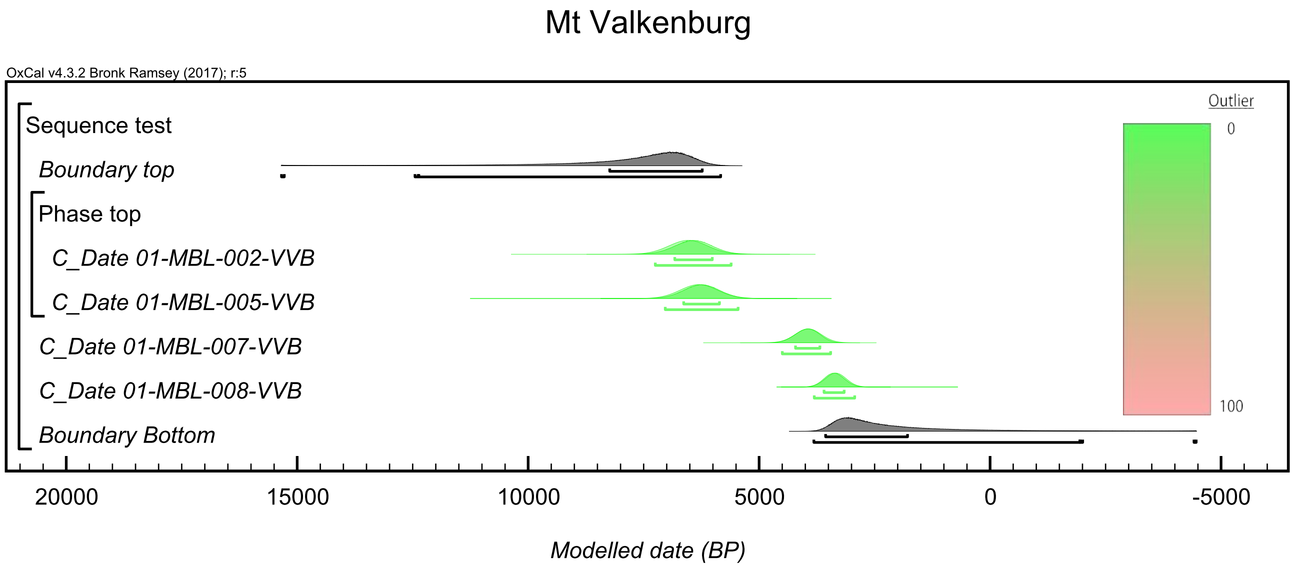

Mt Valkenburg
OxCal v4.3.2 Bronk Ramsey (2017); r:5
Sequence test
Boundary top
Phase top
C_Date 01-MBL-002-VVB
C_Date 01-MBL-005-VVB
C_Date 01-MBL-007-VVB
C_Date 01-MBL-008-VVB
Boundary Bottom
Outlier
0
100
20000
15000
10000
5000
0
-5000
Modelled date (BP)

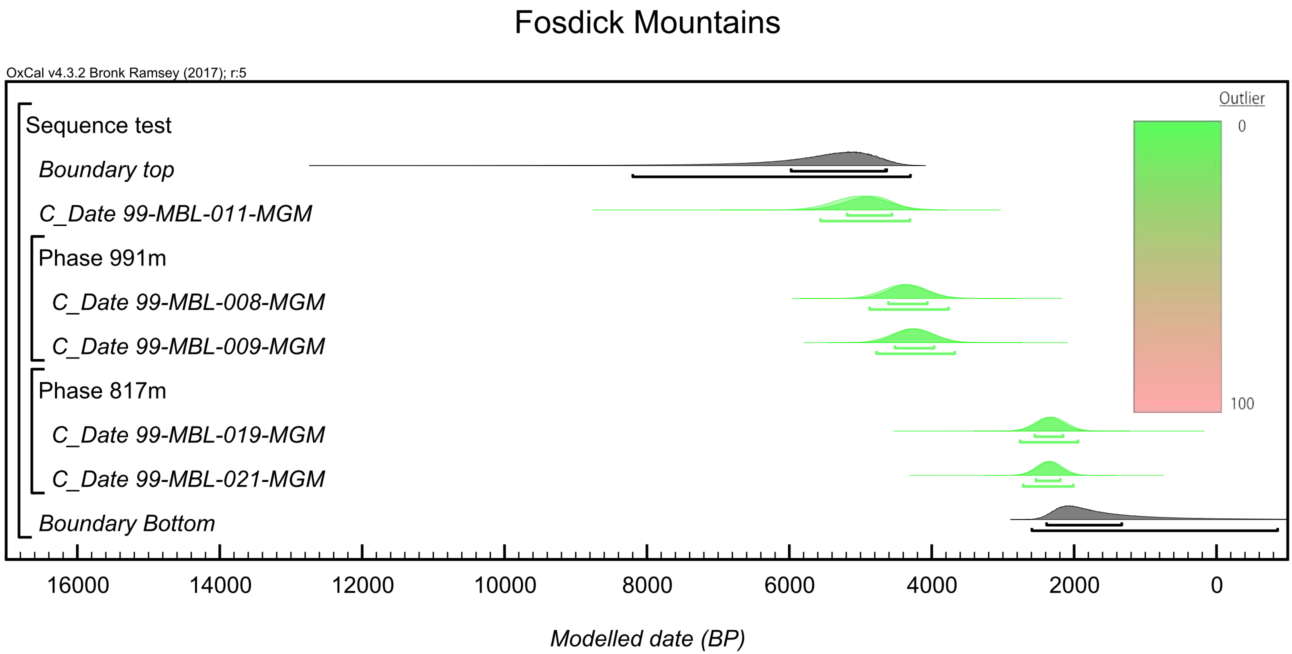

Fosdick Mountains
OxCal v4.3.2 Bronk Ramsey (2017); r:5
Sequence test
Boundary top
C_Date 99-MBL-011-MGM
Phase 991m
C_Date 99-MBL-008-MGM
C_Date 99-MBL-009-MGM
Phase 817m
C_Date 99-MBL-019-MGM
C_Date 99-MBL-021-MGM
Boundary Bottom
Outlier
0
100
16000
14000
12000
10000
8000
6000
4000
2000
0
Modelled date (BP)

Mt Stinear

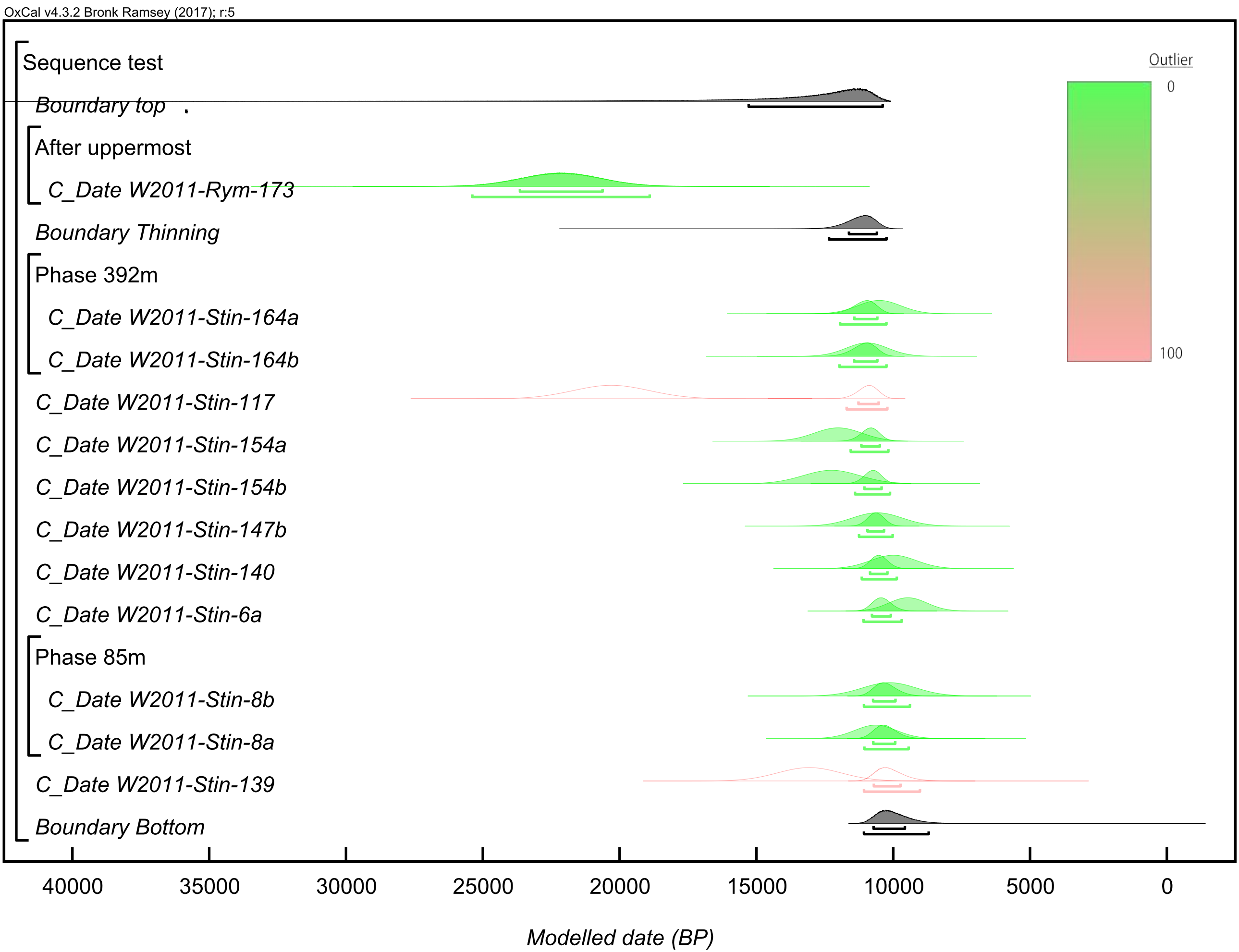
OxCal v4.3.2 Bronk Ramsey (2017); r:5
Sequence test
Boundary top
After uppermost
C_Date W2011-Rym-173
Boundary Thinning
Phase 392m
C_Date W2011-Stin-164a
C_Date W2011-Stin-164b
C_Date W2011-Stin-117
C_Date W2011-Stin-154a
C_Date W2011-Stin-154b
C_Date W2011-Stin-147b
C_Date W2011-Stin-140
C_Date W2011-Stin-6a
Phase 85m
C_Date W2011-Stin-8b
C_Date W2011-Stin-8a
C_Date W2011-Stin-139
Boundary Bottom
Outlier
0
100
40000
35000
30000
25000
20000
15000
10000
5000
0
Modelled date (BP)

Pourquoi-Pas Island

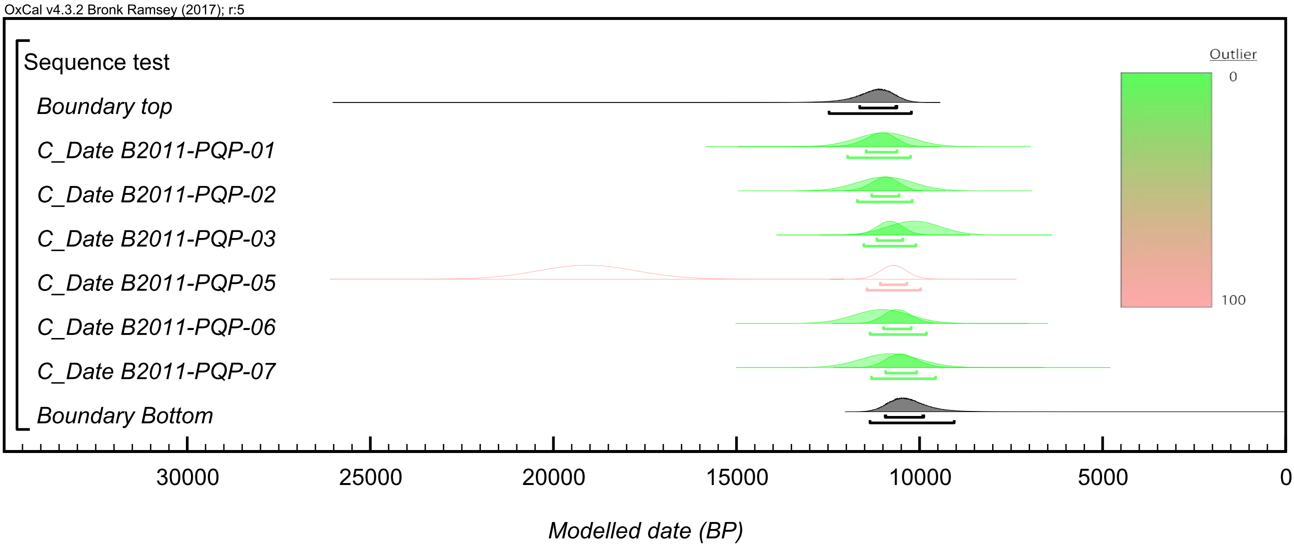

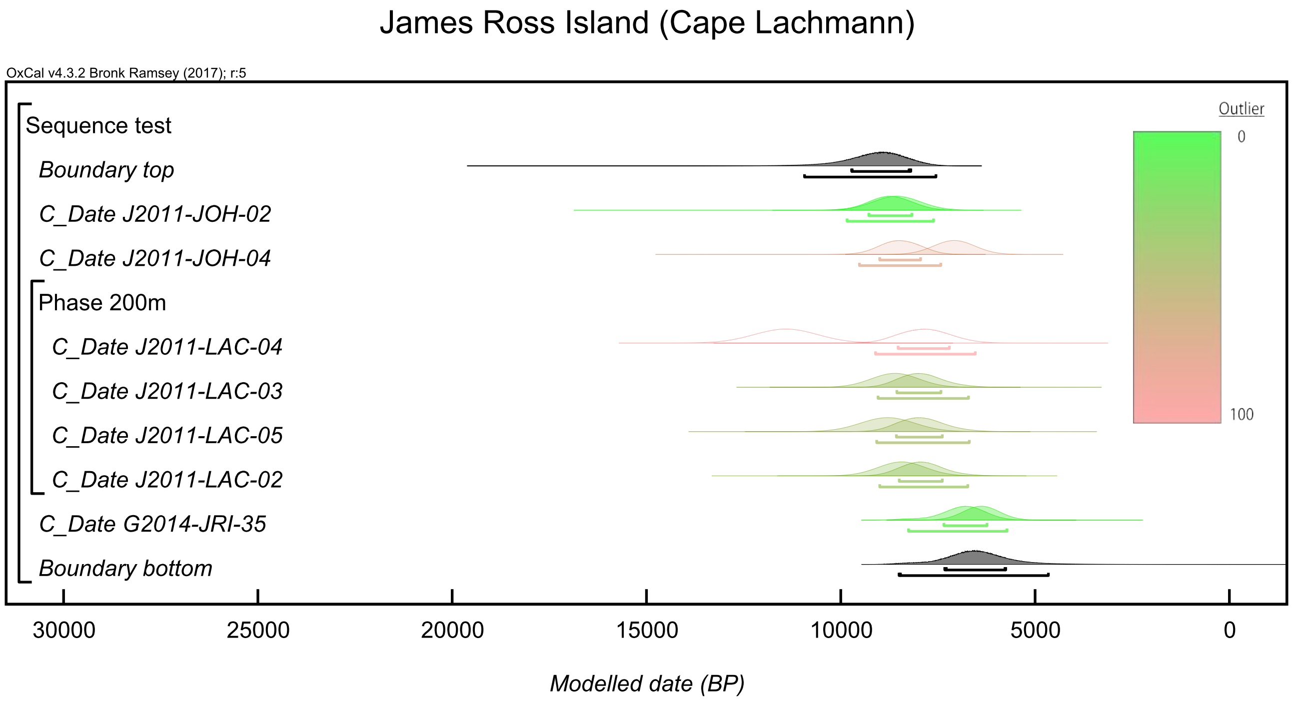
James Ross Island (Cape Lachmann)
OxCal v4.3.2 Bronk Ramsey (2017); r:5
Sequence test
Boundary top
C_Date J2011-JOH-02
C_Date J2011-JOH-04
Phase 200m
C_Date J2011-LAC-04
C_Date J2011-LAC-03
C_Date J2011-LAC-05
C_Date J2011-LAC-02
C_Date G2014-JRI-35
Boundary bottom
Outlier
0
100
30000
25000
20000
15000
10000
5000
0
Modelled date (BP)

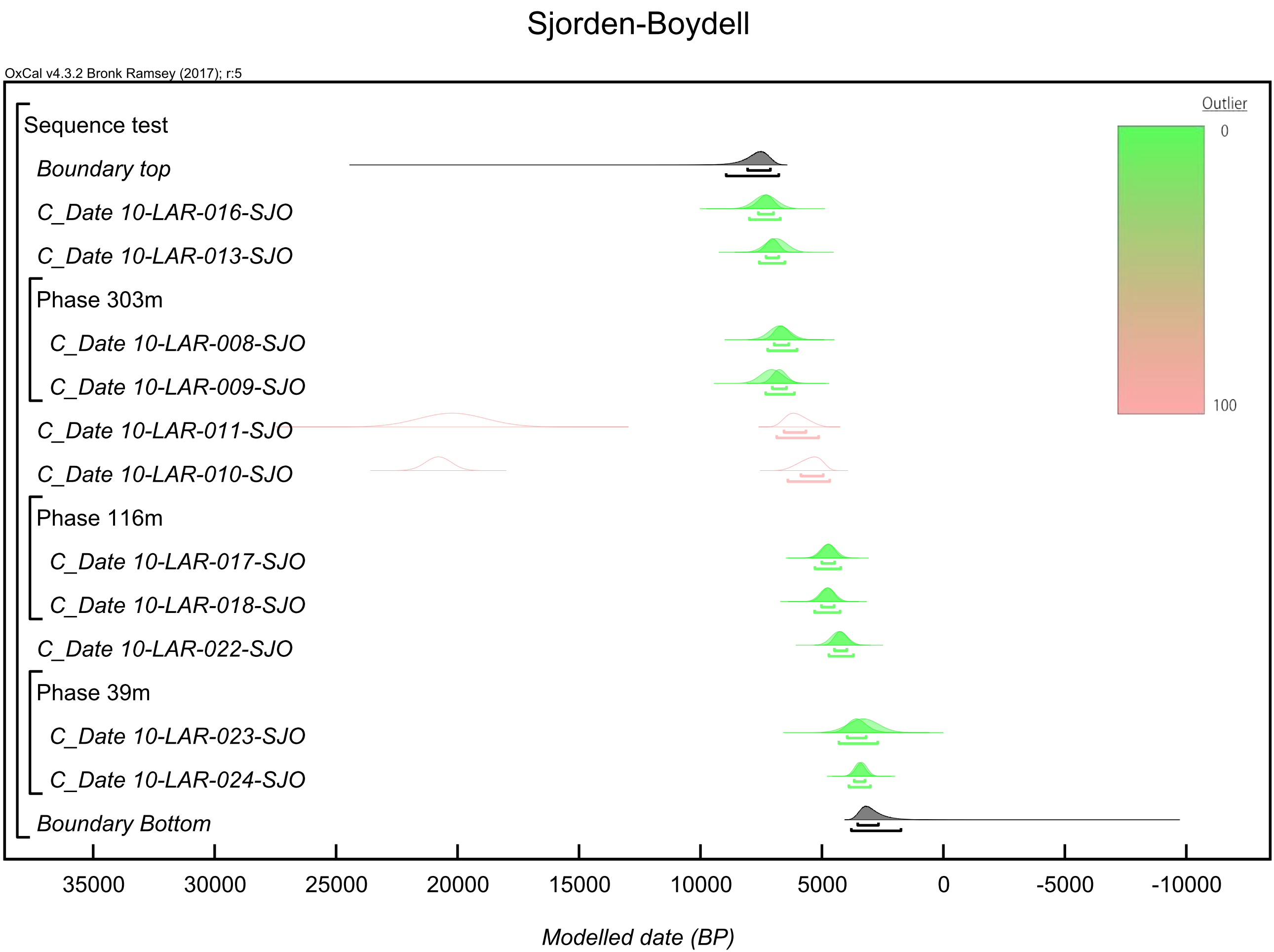
Sjorden-Boydell
OxCal v4.3.2 Bronk Ramsey (2017); r:5
Sequence test
Boundary top
C_Date 10-LAR-016-SJO
C_Date 10-LAR-013-SJO
Phase 303m
C_Date 10-LAR-008-SJO
C_Date 10-LAR-009-SJO
C_Date 10-LAR-011-SJO
C_Date 10-LAR-010-SJO
Phase 116m
C_Date 10-LAR-017-SJO
C_Date 10-LAR-018-SJO
C_Date 10-LAR-022-SJO
Phase 39m
C_Date 10-LAR-023-SJO
C_Date 10-LAR-024-SJO
Boundary Bottom
Outlier
0
100
35000
30000
25000
20000
15000
10000
5000
0
-5000
-10000
Modelled date (BP)

Site 1 – Mount Hope: A) Regressions, B) Histogram.

A)

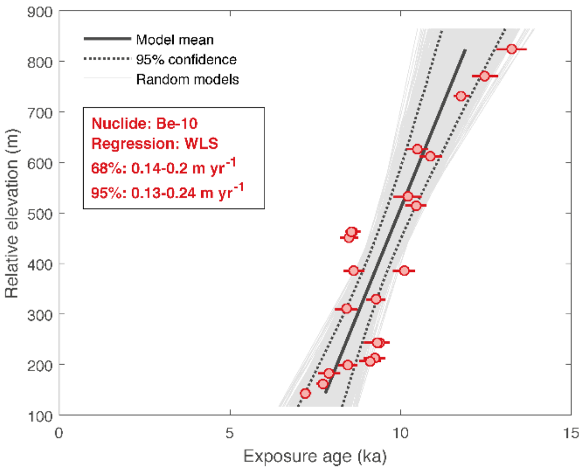

B)

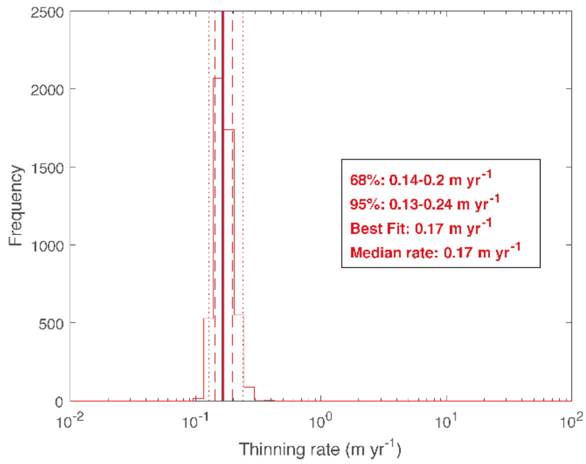

Site 2 – Mount Rigby/Karo

A)

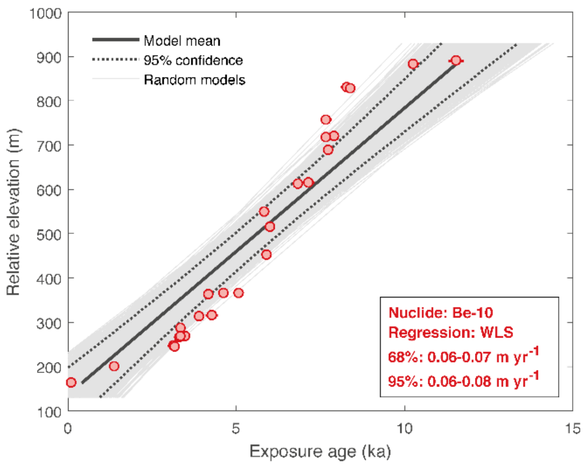

B)

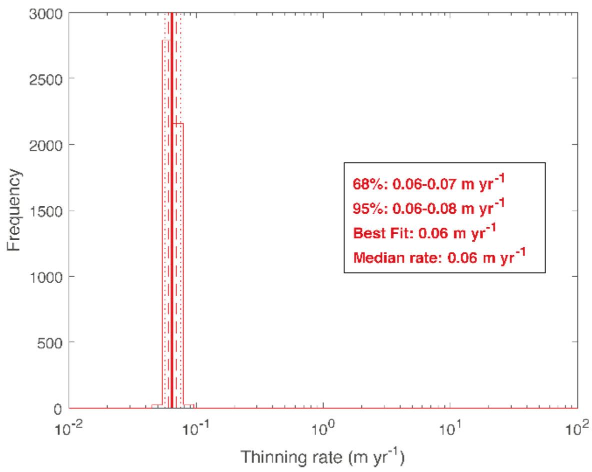

Site 3 – Mount Suess - Gondola Upper

A)

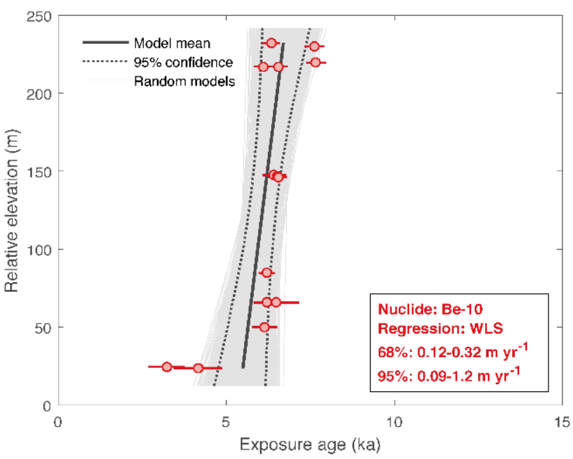

B)

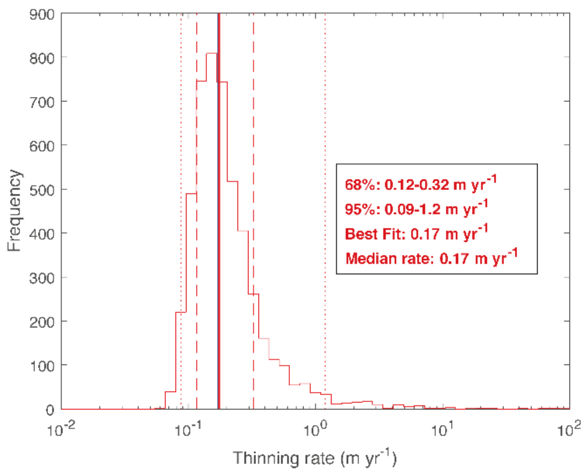

Site 4 – Gondola Mid-Lower

A)

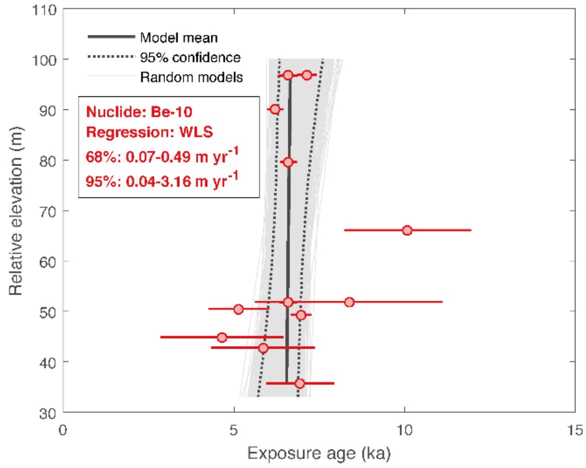

B)

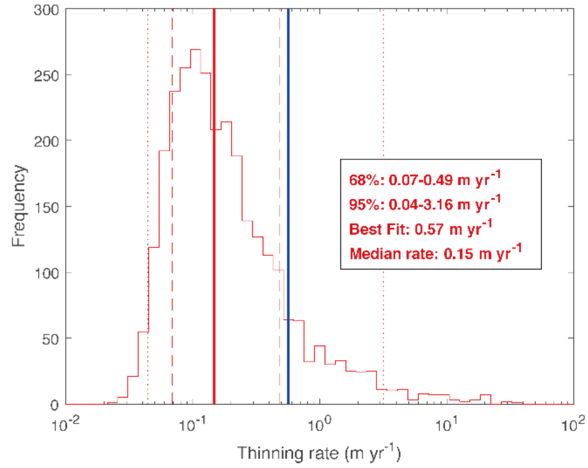

Site 5 – Low Ridge (all samples)

A)

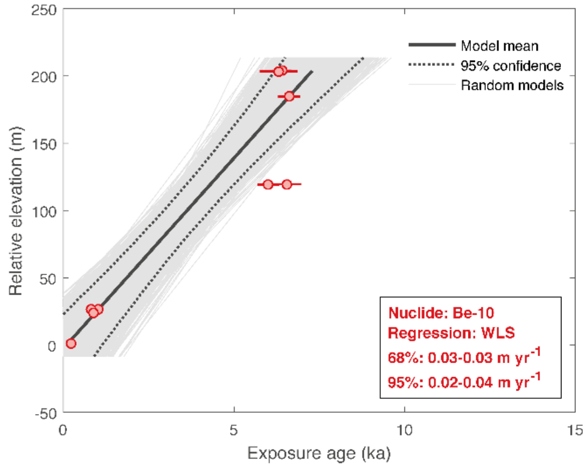

B)

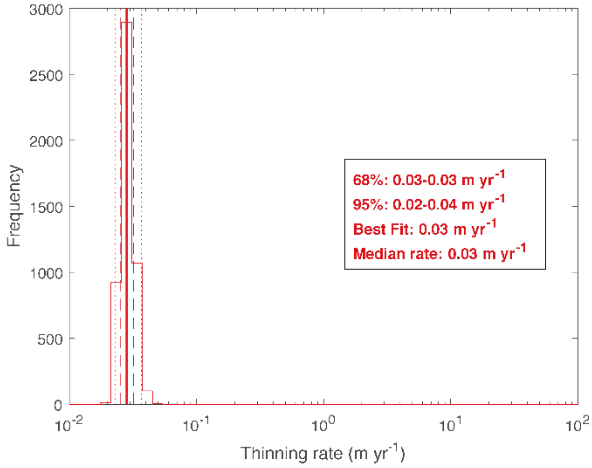

Site 5a – Low Ridge (subset n=5)

A)

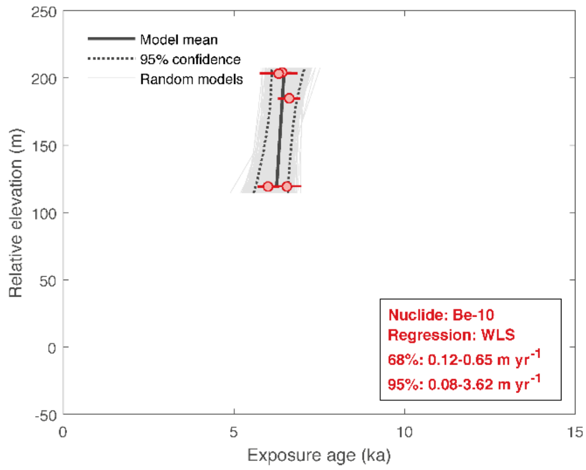

B)

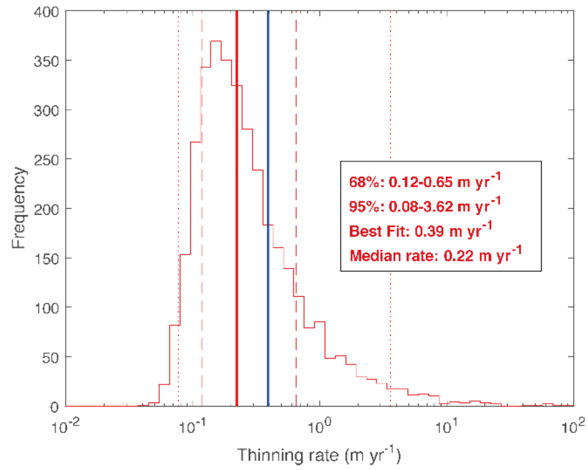

Site 6 – Reedy Glacier (Quartz Hills)

A)

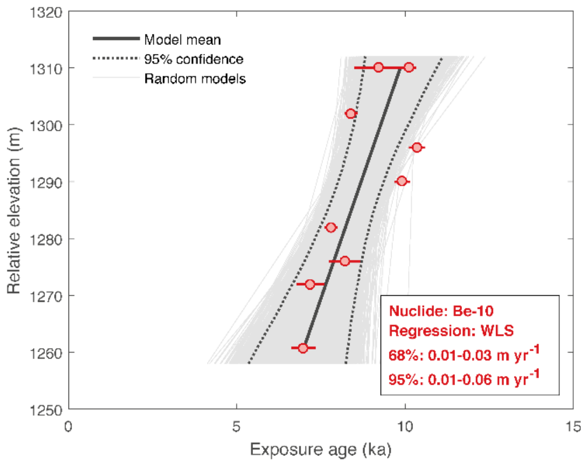

B)

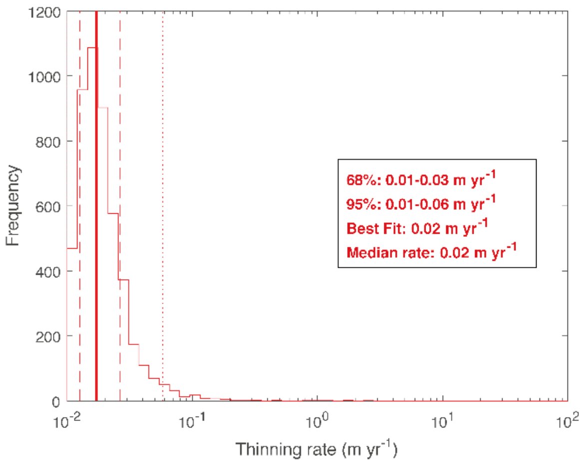

Site 7 – Reedy Glacier (Pip's Peak)

A)

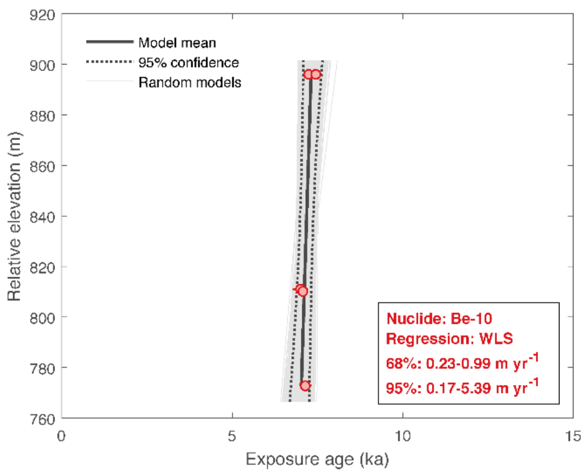

B)

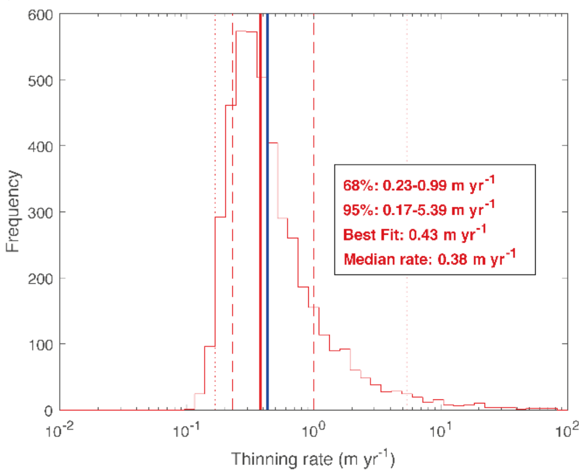

Site 8 – Reedy Glacier (Cohen's Peak)

A)

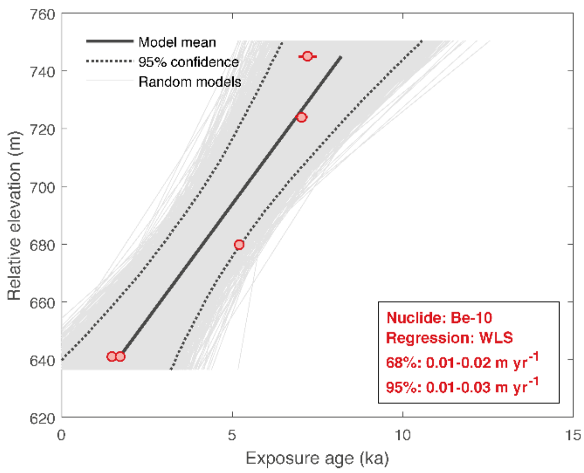

B)

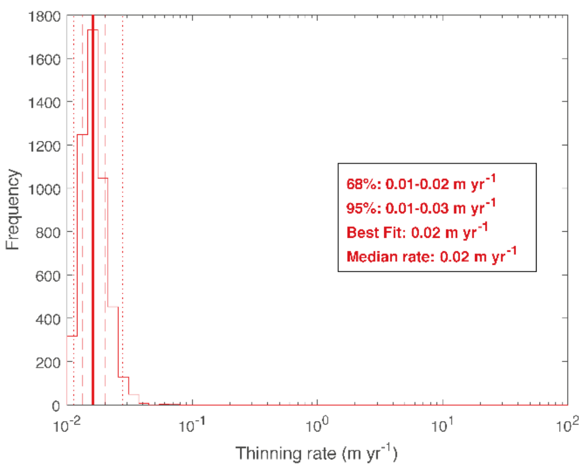

Site 9 – Mount Maish

A)

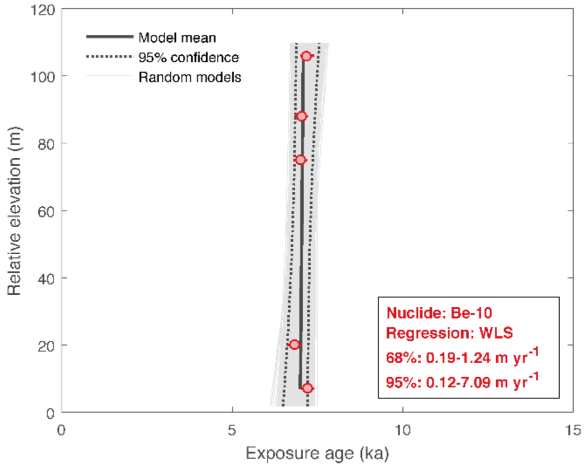

B)

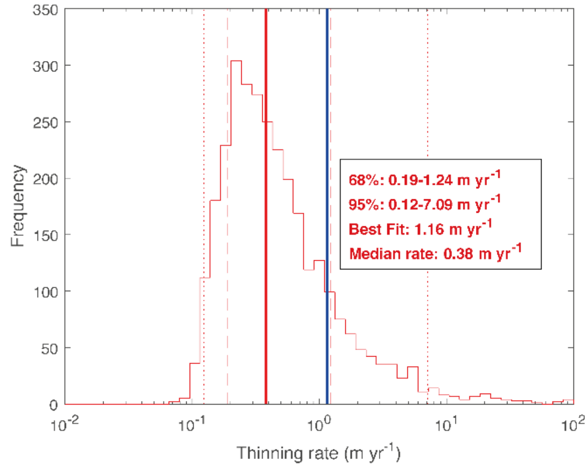

Site 10 – Mount Moses (all samples)

A)

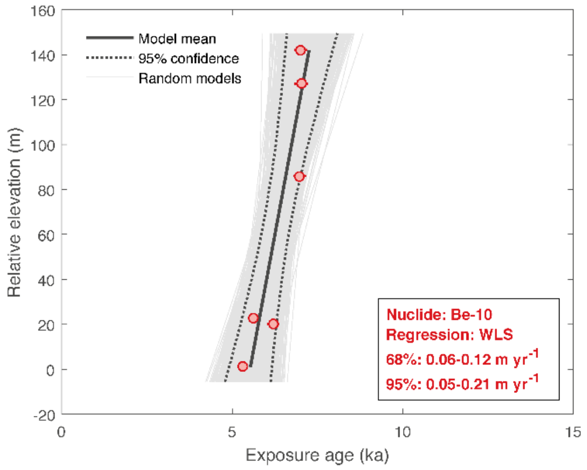

B)

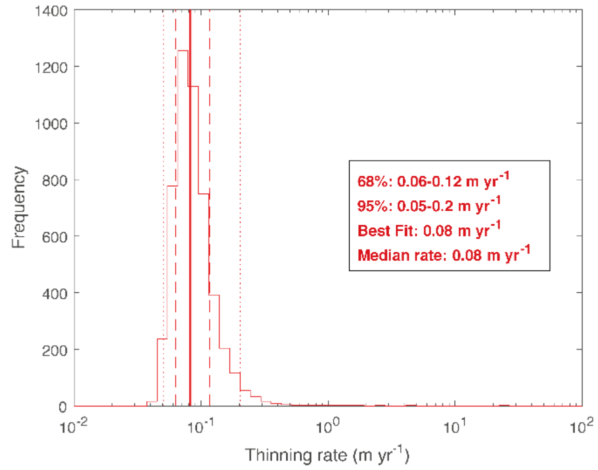

Site 10a – Mount Moses (subset n=3)

A)

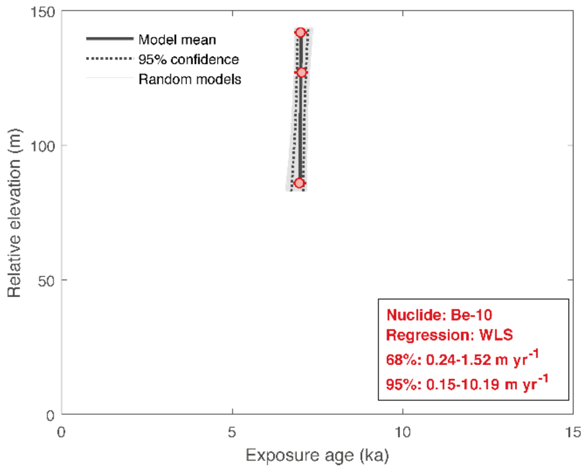

B)

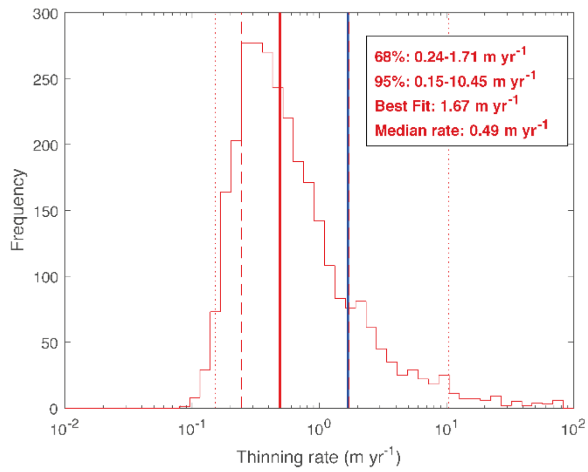

Site 11 – Williams Hills

A)

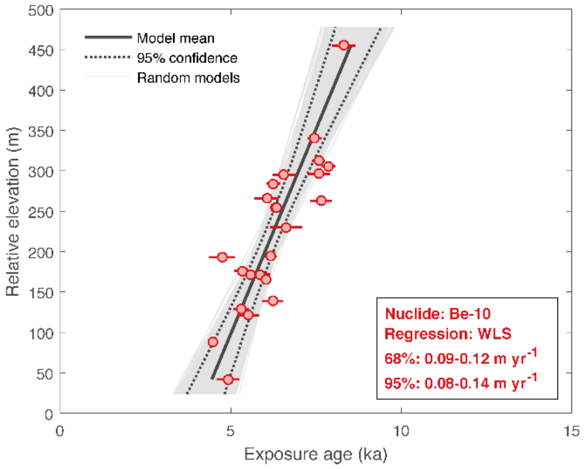

B)

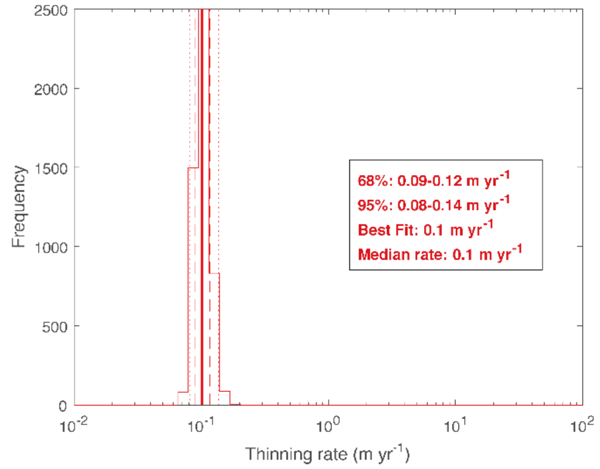

Site 12 – Thomas Hills

A)

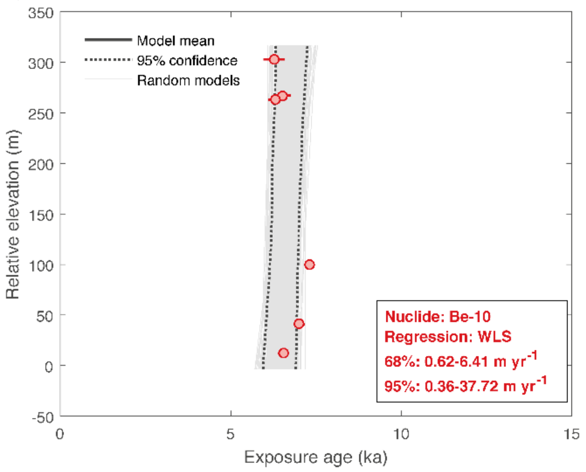

B)

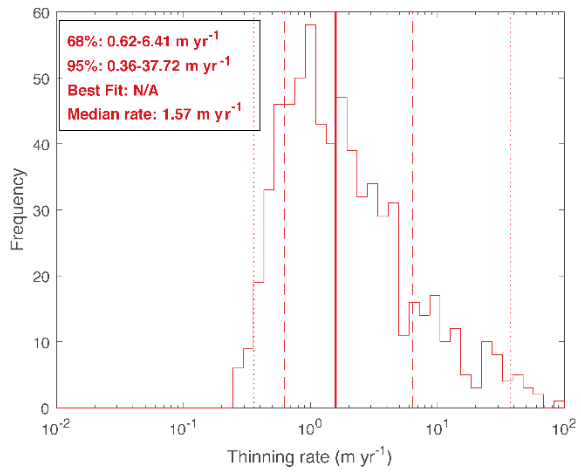

Site 13 – Mount Harper/Bragg

A)

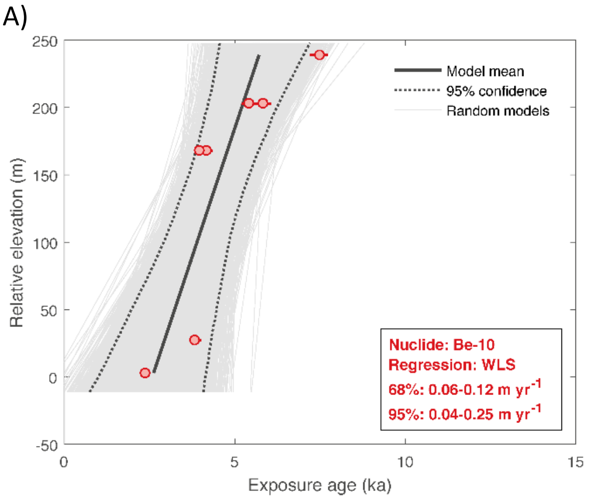

B)

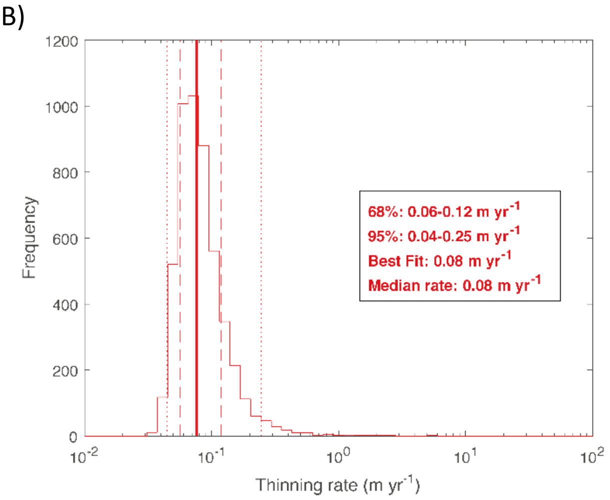

Site 14 – Marble Hills

A)

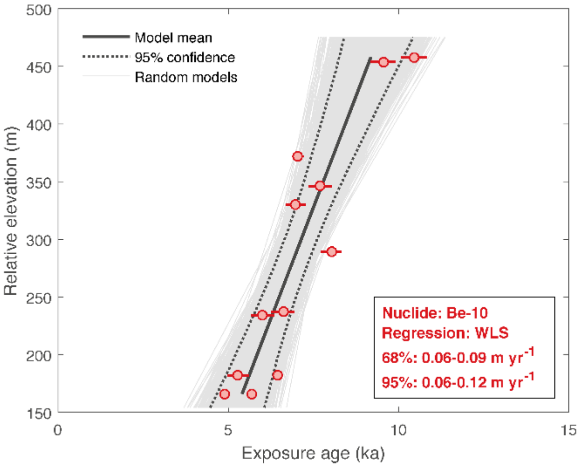

B)

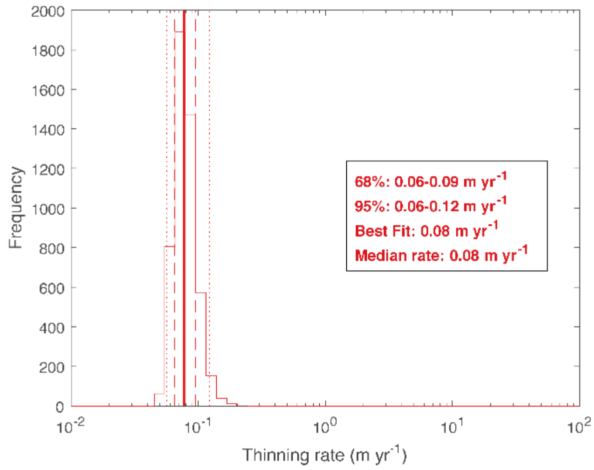

Site 15 – Patriot Hills

A)

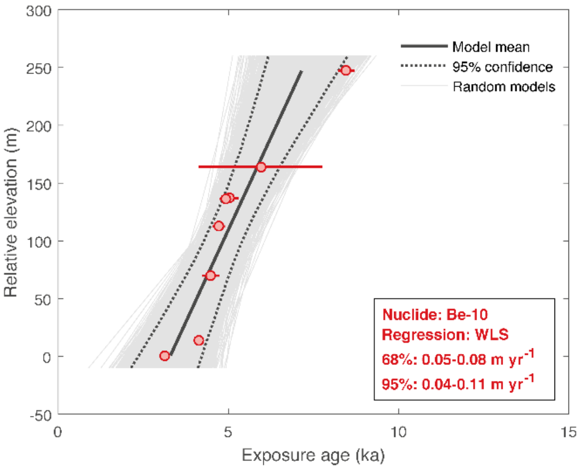

B)

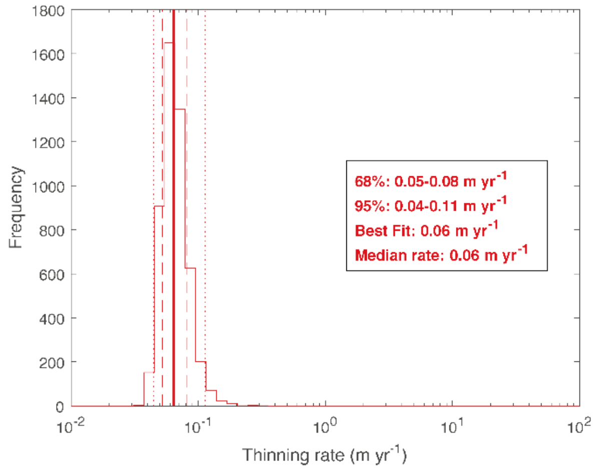

Site 16 – Mount Rea

A)

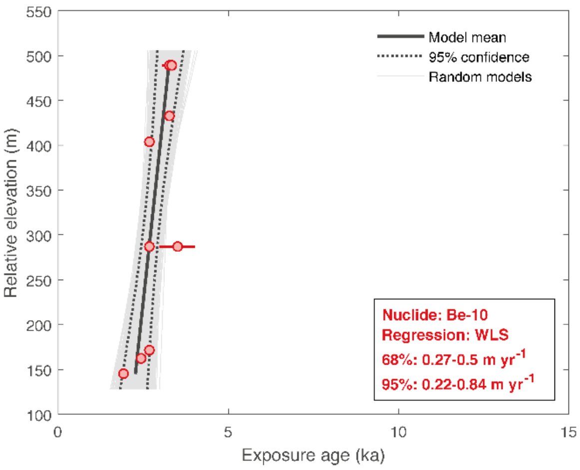

B)

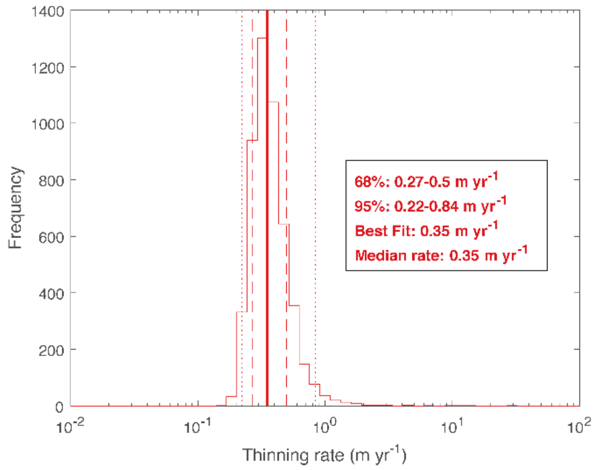

Site 17 – Mount Darling

A)

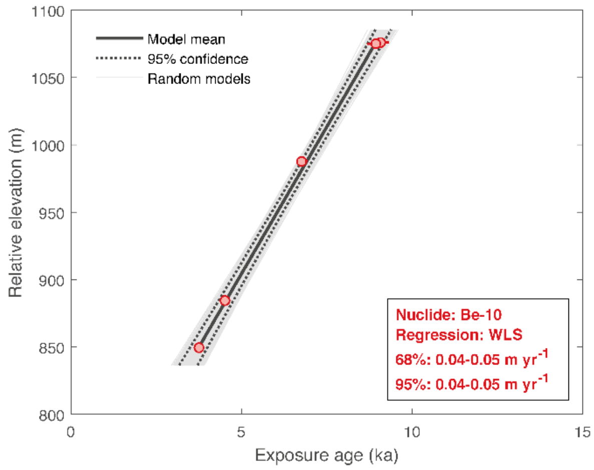

B)

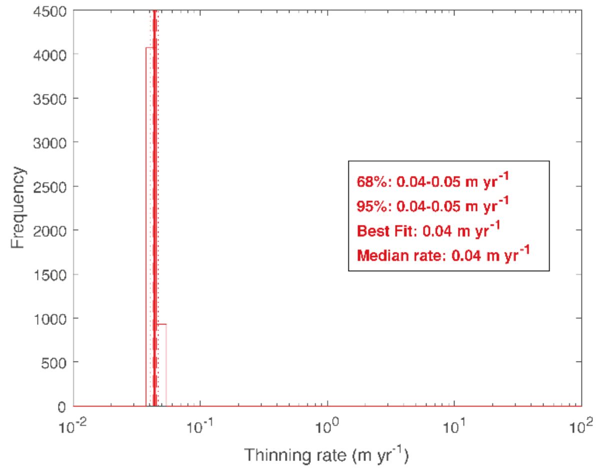

Site 18 – Mount Valkenburg

A)

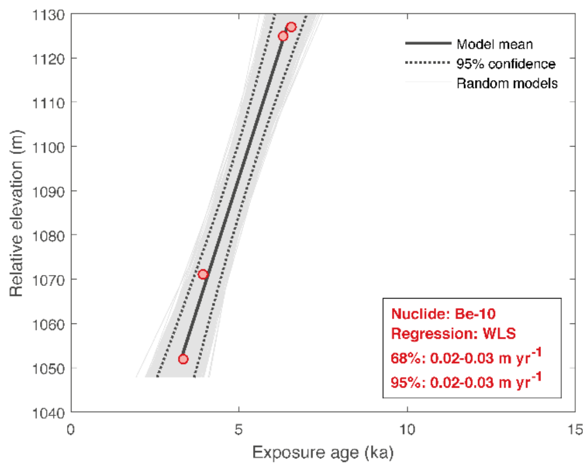

B)

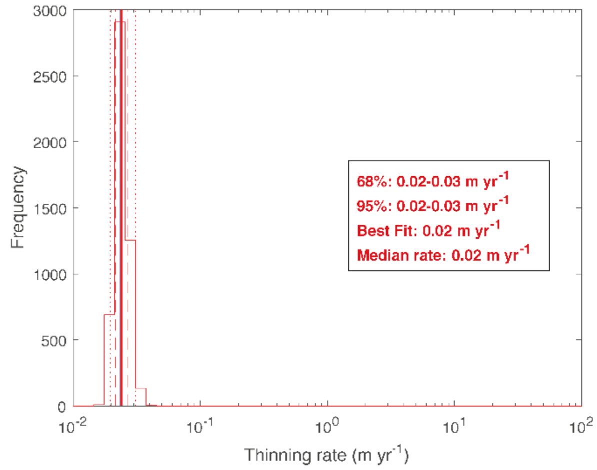

Site 19 – Fosdick Mountains

A)

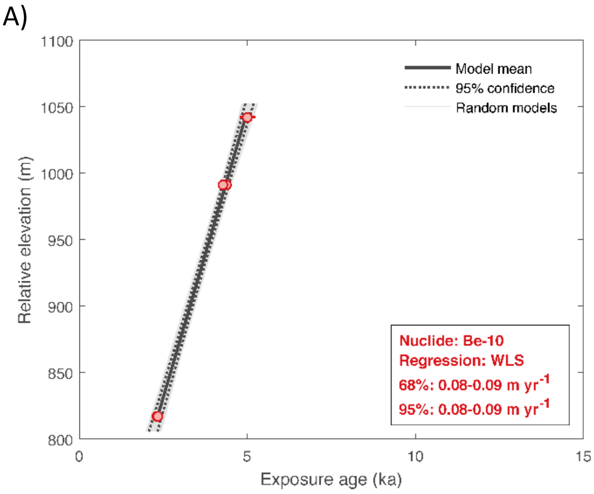

B)

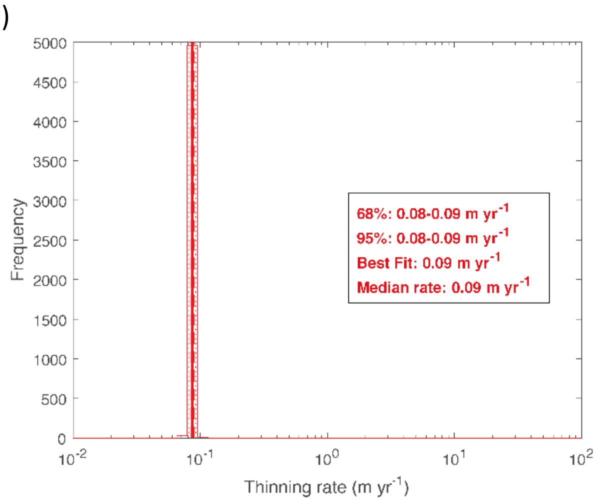

Site 20 – Mount Stinear

A)

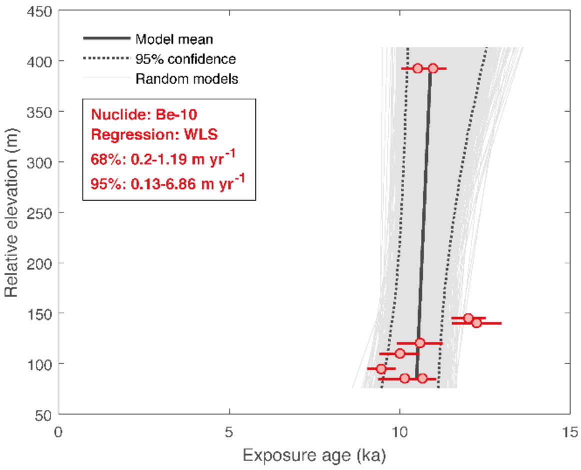

B)

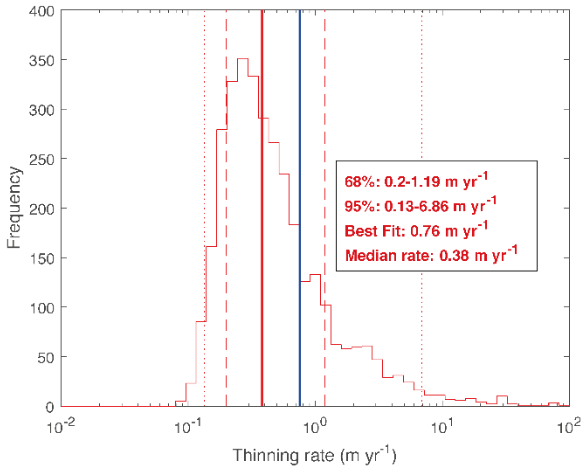

Site 21 – Pourquoi-Pas Island

A)

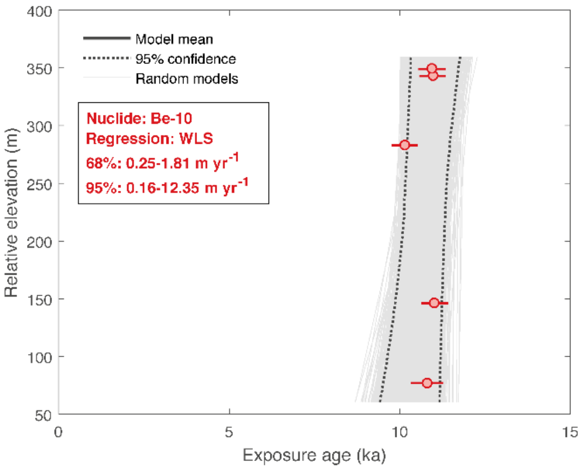

B)

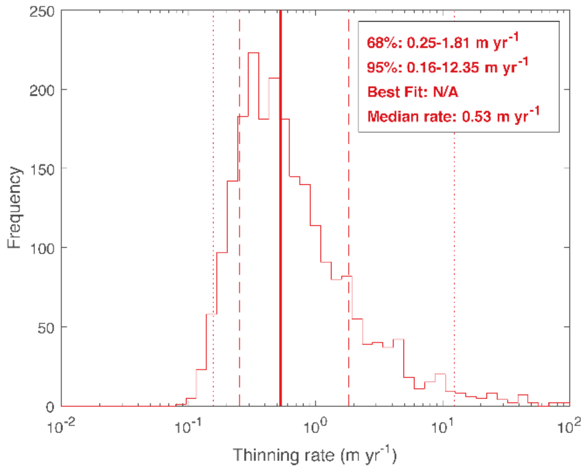

Site 22 – James Ross Island

A)

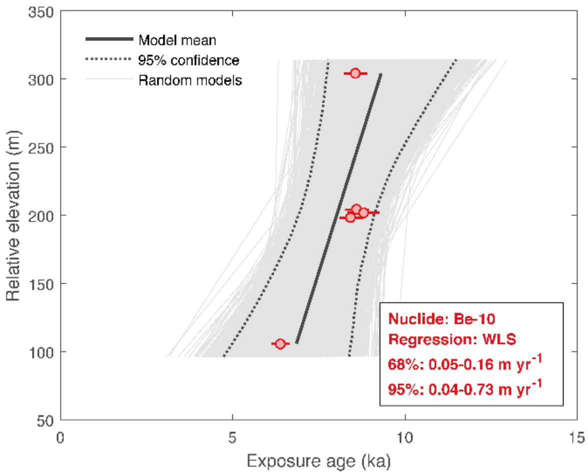

B)

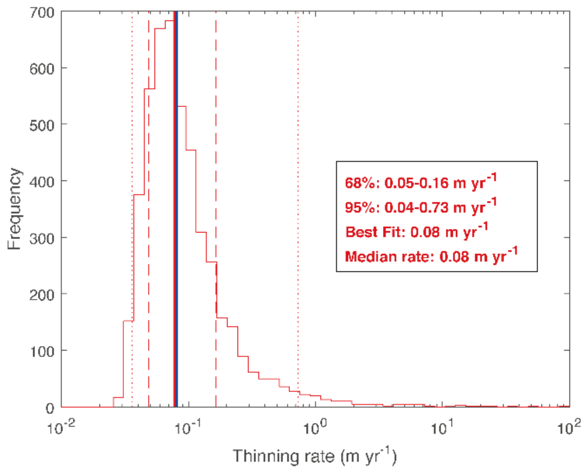

Site 23 – Sjorden-Boydell Fjord

A)

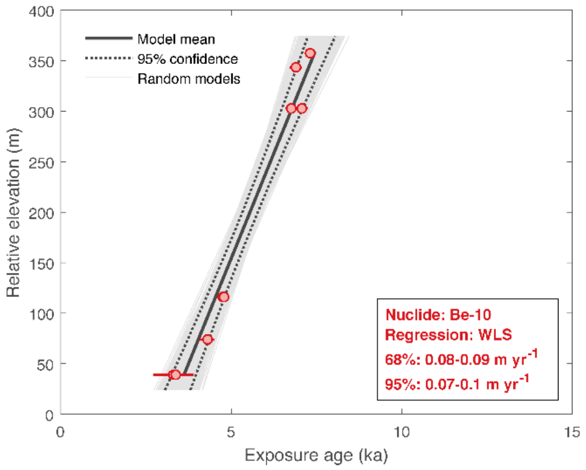

B)